universität wien

DISSERTATION

Titel der Dissertation

„On the effects of finiteness and sampling in simulation of ionic liquids: Implications for molecular dynamics simulations and NMR theory“

Verfasserin

Mag. Sonja Gabl

angestrebter akademischer Grad

Doktorin der Naturwissenschaften (Dr.rer.nat.)

Wien, 2014

Studienkennzahl lt. Studienblatt:	A 791 419
Dissertationsgebiet lt. Studienblatt:	Chemie
Betreuerin / Betreuer:	Univ.-Prof. Dr. Othmar Steinhauser

Danksagung

Ich möchte an dieser Stelle all jenen Menschen danken, die mich beim Erstellen dieser Arbeit und deren zugrundeliegenden Publikationen begleitet und unterstützt haben.

In akademischer Hinsicht gilt mein Dank zunächst allen am INSTITUT FÜR COMPUTERGESTÜTZE BIOLOGISCHE CHEMIE. Ich danke besonders Prof. Dr. Othmar Steinhauser, der mich in allen Belangen unterstützte und mir half durch Erklärung der theoretischen Hintergründe so manches Ergebnis richtig zu interpretieren.

Auch Dr. Christian Schröder war ein sehr wichtiger Ansprechpartner, der mir immer mit gutem Rat zur Seite stand.

Weiters möchte ich der gesamten Arbeitsgruppe danken. Sie hat mich besonders in den letzten Monaten meiner Arbeit moralisch und mit Rechen-Ressourcen unterstützt.

Außerdem möchte ich Prof. Dr. Hermann Weingärtner an der Ruhr-Universität Bochum für den interessanten fachlichen Austausch danken.

An dieser Stelle möchte ich meinen Eltern, meinem Bruder und meinem Mann danken. Ihr habt mir durch eure Unterstützung nicht nur mein Doktorat ermöglicht, sondern auch den entsprechenden sozialen Rahmen geboten. Ihr habt meine Höhen und Tiefen über die Jahre meines Studiums miterlebt und hattet besonders an Donnerstagen ein offenes Ohr für meine Sorgen.

Abstract

In this thesis we take a closer look on the methodical aspects of dealing with ionic liquids in molecular dynamics simulations. Since the simulation of Coulomb forces faces the finiteness of computational resources, one has to apply a method, which minimises this dependence, in our case the Ewald method. Nevertheless, to assess finite size effects simulations of various system sizes as well as extensive length were performed. Structural data, single particle and collective properties were deduced and dielectric spectra were computed from simulation data . This offered valuable clues to the size and time dependence in systems containing ionic liquids. To describe the size dependence of various properties, the values were plotted versus the inverse box length. For sufficiently large systems a linear regime as predicted by hydrodynamic theory could be identified in the plots. We found evidence that the onset of this regime is primarily affected by viscosity. Using these findings of finite size effects, trajectory data of $C_2mim^+BF_4^-$ was generated to calculate the intermolecular ^{1}H-^{19}F nuclear Overhauser effect (NOE) at full distance resolution. Since the zero frequency would require extremely long simulation lengths, which is needed for the homonuclear NOE, we were restricted to the calculation of the heteronuclear NOE at high frequencies due to finite simulation length. Furthermore, existing model theories were extended and new ones developed to reveal a distance dependence of the spectral density function. This range of the NOE on the other hand depends on the frequency. Nevertheless, the frequency dependence decreased with increasing complexity of the model theory and vanished altogether for simulation. Even more sensitive are the cross and longitudinal relaxation rate, which depend on the combination of the viscosity of the sample and the spectrometer frequency. Last, we investigated the importance of phase space sampling by performing non-equilibrium simulations. The solvation response functions of two different ionic liquids and one coumarin C153 were calculated and the results were compared to equilibrium simulation as well as experiment.

Zusammenfassung

In dieser Arbeit werden die methodischen Aspekte von Molekulardynamiksimulationen, welche sich mit ionischen Flüssigkeiten beschäftigen, näher betrachtet. Da die Simulation der Coulomb-Kräfte der Endlichkeit von Computerresourcen gegenübersteht, muss eine Methode gefunden werden, die diese Effekte minimiert, in unserem Fall die Ewald Methode. Um die Endlichkeitseffekte besser beurteilen zu können wurden Simulationen von unterschiedlichen Systemgrößen und langer Dauer gemacht. Davon wurden Strukturdaten, Eigenschaften von Einzelpartikeln als auch kollektive Eigenschaften berechnet und dielektrische Spektren generiert. Von diesen Daten konnte Information über die Größen- und Zeitabhängigkeit von Systemen, die ionische Flüssigkeiten behandeln, gewonnen werden. Um die Größenabhängigkeit von verschiedenen Eigenschaften zu beschreiben wurden diese gegen die inverse Boxlänge geplottet. Ab einer bestimmten Systemgröße konnte ein lineares Regime, vorausgesagt von hydrodynamischer Theorie, in diesen Plots identifiziert werden. Wir fanden Indizien, dass der Beginn dieses Bereichs durch die Viskosität beeinflusst wird. Unter Verwendung der Ergebnisse von Endlichkeitseffekten, wurde eine Trajektorie von $C_2mim^+BF_4^-$ generiert um den intermolekularen ^{1}H-^{19}F nuklear Overhauser Effekt (NOE) in voller Distanzresolution zu berechnen. Da die Null-Frequenz extrem lange Simulationsdauern benötigen würde, die man braucht für den homonuklearen NOE, beschränkten wir uns auf die Berechnung des heteronuklearen NOEs bei hohen Frequenzen aufgrund der endlichen Simulationslänge. Weiters wurden bestehende Modelltheorien erweitert und neue entwickelt um eine Distanzabhängigkeit in der spektralen Dichtefunktion zu zeigen. Diese Reichweite des NOE hängt wiederum von der Frequenz ab. Nichtsdestotrotz nahm die Frequenzabhängigkeit mit zunehmender Komplexität der Modelltheorie ab um im Fall der Simulation ganz zu verschinden. Sogar noch sensitiver sind die Kreuz- und longitudinale Relaxationsrate, welche von der Kombination der Viskostität der Probe als auch der Frequenz des Spektrometers abhängen. Zuletzt untersuchen wir die Bedeutung des Phasenraumsamplings indem Nichtgleichgewichtssimulationen durchgeführt wurden. Von zwei verschiedenen ionischen Flüssigkeiten mit jeweils einem Coumarin C153 wurde die Lösungsmittelantwort berechnet und die Ergebnisse wurden verglichen mit Gleichgewichtssimulationen sowie dem Experiment.

Contents

1 Introduction **1**

1.1 Room temperature ionic liquids 1

1.2 Molecular dynamics simulation of liquids 2

1.3 Outline of the following publications 4

2 Declaration by the author **7**

3 Computational studies of ionic liquids: Size does matter and time too **9**

4 From Short-Range to Long-Range Intermolecular NOEs in Ionic Liquids: Frequency Does Matter **25**

5 Pair dynamics and the intermolecular nuclear Overhauser effect (NOE) in liquids analysed by simulation and model theories: Application to an ionic liquid **33**

6 On the solvation dynamics of coumarin C153 in ionic liquids: Comparison of non-equilibrium simulation to equilibrium simulation and experiment **53**

7 Final discussion **71**

Bibliography 81

Curriculum Vitae 83

1 Introduction

1.1 Room temperature ionic liquids

Since the discovery synthesis of ionic liquids (IL) by Paul Walder (1914) exactly one decade ago, the interest in this topic did not diminish over time. Ionic liquids are salts, which are liquid at room temperature under standard conditions for temperature and pressure without being dissolved in a solvent. They consist of highly anisotropic cations, which are large asymmetric molecules with a charge distribution over all atoms. The anions range from typical inorganic molecules to more elaborate organic molecules. Due to the anisotropy, an allocation of molecules in a crystal lattice is not possible at room temperature and therefore, they are liquid, mostly at the price of high viscosity. Furthermore, the anisotropic charge distribution in the molecule results in a noteworthy dipole moment.

The fact, that in an ionic liquids the dipole moment and net charge reside on the very same molecule, does not facilitate their interpretation as it is possible for other liquids. In case of dielectric relaxation in a molecular liquid, such as acetone or water, which have a dipole moment but no net charge, dynamics is solely described by collective rotation as depicted in Fig.1.1a. Molten salts, such as NaCl, on the other hand are determined by translational dynamics of the net charges on atoms (Fig.1.1b). Although, an ionic solution combines translational and rotational dynamics, the effects can be ascribed to different species (Fig.1.1c). In ionic liquids, however, rotational dynamics is highly coupled due to the dipole moment and translational motions due to the net charge. But in this case dipole moment and net charge reside on the very same molecule as can readily be seen in Fig.1.1d.

Due to the fact that there are innumerable cation-anion combinations, physico-chemical properties can be influenced, which makes them inter-

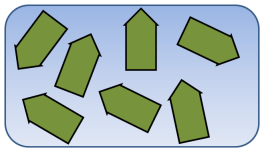

(a) Dynamics in a molecular liquid is solely described by collective rotation.

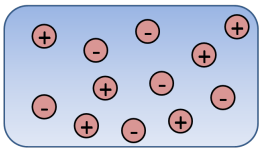

(b) Dynamics in a molten salt is solely described by collective translation.

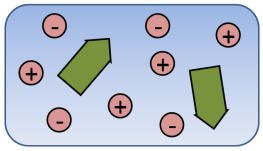

(c) Rotational and translational dynamics can be ascribed to either one of the species included in an ionic solution.

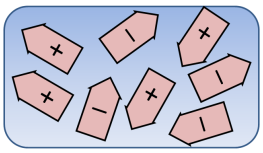

(d) Combined rotational and translational dynamics are needed for an ionic liquid, where net charge and dipole moment reside on the same molecule.

Figure 1.1: Characteristics of various liquids.

esting as solvents for organic and inorganic synthesis [1], energy-related applications [2, 3] and many more [4]. Nevertheless, the question of their harmlessness [4–7] and the fact that ionic liquids are still rather expensive prevents widespread usage.

1.2 Molecular dynamics simulation of liquids

In this thesis I used molecular dynamics (MD) simulation to study ionic liquids and I placed special emphasis on the correct handling of the method with respect to Coulomb systems. This chapter will focus on aspects, which will be needed for the further understanding of my publications, but for a detailed description of the theory behind MD simulation please refer to other, more exhaustive sources [8, 9].

To describe the time evolution of a given set of particles, molecular dynamics simulation numerically solves the classical equations of motion

$$\frac{d^2\vec{x}_i(t)}{dt^2} = \frac{\vec{F}_i(t)}{m_i}, \tag{1.1}$$

where $\vec{F}_i(t)$ is the force acting on atom i with its mass m_i and thus influencing its behaviour. On the other hand, the force $\vec{F}_i(t)$ is determined by an empirical potential V, which is also known as force field,

$$\vec{F}_i(t) = -\nabla V(\vec{x}_i). \tag{1.2}$$

The potential $V(\vec{x}_i)$ consists of five different types of interactions, which for reasons of convenience are written in internal coordinates, r_{ij}, θ_{ijk} and ϕ_{il}:

$$\begin{aligned} V(\vec{x}_i) &= \sum_{bonds} K_{ij}(r_{ij} - r_{ij,0})^2 && (1.3)\\ &+ \sum_{angles} K_{ijk}(\theta_{ijk} - \theta_{ijk,0})^2 && (1.4)\\ &+ \sum_{dihedrals} K_{ijkl}(1 - \cos(n_{ijkl}\phi_{il} - \delta_{ijkl})) && (1.5)\\ &+ \sum_i \sum_{i<j} \epsilon_{ij}\left[\left(\frac{r_{\min,ij}}{r_{ij}}\right)^{12} - 2\left(\frac{r_{\min,ij}}{r_{ij}}\right)^{6}\right] && (1.6)\\ &+ \sum_i \sum_{i<j} \frac{q_i q_j}{4\pi\epsilon_0 r_{ij}} && (1.7) \end{aligned}$$

The first term (Eq.1.3) of the potential $V(\vec{x}_i)$ is needed to describe a covalent bond to an atom j with the force constant K_{ij} and an equilibrium distance $r_{ij,0}$. The second term (Eq.1.4) is needed for the angle between the bonds of atoms i and k to another atom j with the force constant K_{ijk} and the angle in equilibrium $\theta_{ijk,0}$. Eq.1.5 characterises the dihedral angle between a plane, constructed by the atoms i, j and k, and a plane made up by the atoms j, k and l. K_{ijkl} is the force constant, n_{ijkl} specifies the multiplicity of the dihedral angle and δ_{ijkl} is a shift constant of 0° or 180° degrees. The Lennard-Jones potential can be identified in the fourth term (Eq.1.6). It models the Van der Waals interaction of two atoms i and j with the parameters $\epsilon_{ij} = \sqrt{\epsilon_i \epsilon_j}$ and $r_{\min,ij} = (r_{\min,i} + r_{\min,j})/2$. The last term to describe interactions in ionic liquids is the Coulomb potential (Eq.1.7)with the dielectric permittivity of vacuum ϵ_0, partial atomic charges q_i and q_j as well as the interatomic distance r_{ij}.

Due to the fact that in ionic liquids each molecule carries a net charge, an accurate description of electrostatic interactions is extremely important.

Unfortunately, the Coulomb potential has a r^{-1} dependence, i.e. 'infinite range', and is not necessarily compatible with finite computer resources. Therefore, another methodic approach to describe the intermolecular interactions of charge distributions may be necessary.

The description of electrostatic forces by permanent charges, or any other method, misses the ability to adapt the molecular charge distribution to quick changes in the local neighbourhood, since the atomic charges are kept fix. To overcome this drawback, the so-called Drude model, also known as charge-on-a-spring model [10], is used to describe atomic polarizabilities. Thereby, particles of nearly no mass and opposite sign are attached to all non-hydrogen atoms.

Although, the implementation of polarizability can be seen as a means to include electronic degrees of freedom by avoiding quantum-chemical calculations, it is not done without additional computational costs. Nevertheless, the inclusion of induced charges has its merits, since dynamics is accelerated, because the interactions of atomic charges are dampened.

1.3 Outline of the following publications

Based on a good empirical force field, MD simulations can be carried out. The resulting sets of coordinates and velocities are stored in so-called trajectories, which are needed for analysis. To satisfy the ergodic hypothesis, i.e. the time a system requires to sufficiently sample phase space, two different approaches can be pursued. On the one hand, one trajectory of great length, or, on the other hand, a lot of short trajectories, distributed over phase space, can be simulated. The first possibility, i.e. the generation of one long trajectory, normally refers to simulation in equilibrium, although it can be used to study systems in non-equilibrium in combination with linear response theory. Another technique to determine the effects of some kind of applied external field on a system is simulation in non-equilibrium.

To actually determine effects of finiteness and sampling in simulation of ionic liquids, as stated in the title of this thesis, analysis of trajectory data is used as a tool. Thereby, the comparison to experimental results helps to

shed further light on the matter.

In this thesis I want to address effects of finiteness in ionic liquids in a twofold manner. On the one hand, the effects can be part of the simulation method and can be influenced by system size as well as trajectory length. To assess the impact of these effects, analysis of simulation data can be performed on properties like energy, structure, collective and single particle properties as well as dielectric spectra. These issues are investigated in detail in the first publication [11].

On the other hand, effects of finiteness can be found in a quantity, which describes a certain behaviour in a system, e.g. the spatial range of the *intermolecular* nuclear Overhauser effect (NOE). This quantity can either be directly calculated from simulation data or by means of model theories. This is addressed in the second and third publication [12, 13].

Furthermore, in this thesis I focus on phase space sampling. Therefore, two techniques, simulation in equilibrium and non-equilibrium, are compared to each other. To be able to rate the two simulation methods, analysis of the solvation response function can be used. Comparison of the results to experimental data grants certainty of the quality of the methods. In addition, advantages or drawbacks of these methods can be identified. This matter is discussed in the last article [14].

2 Declaration by the author

In this thesis I investigated the effects of finiteness and sampling by means of molecular dynamics simulation of ionic liquids. Thereby, I put a special focus on the methodology of simulation as well as NMR theory. The results have been summarised in four articles of which three have been published (Section 3, Section 4 and Section 5) and one is intended for publication in *The Journal of Chemical Physics* (Section 6).

Section 3

Sonja Gabl, Christian Schröder, and Othmar Steinhauser. Computational studies of ionic liquids: Size does matter and time too. *J. Chem. Phys.* **137**, 094501 (2012); DOI: 10.1063/1.4748352

Section 4

Sonja Gabl, Othmar Steinhauser, and Hermann Weingärtner. From Short-Range to Long-Range Intermolecular NOEs in Ionic Liquids: Frequency Does Matter. *Angew. Chem. Int. Ed.* **52**, 9242 (2013); DOI: 10.1002/anie.201302712

Section 5

Sonja Gabl, Christian Schröder, Daniel Braun, Hermann Weingärtner, and Othmar Steinhauser. Pair dynamics and the intermolecular nuclear Overhauser effect (NOE) in liquids analysed by simulation and model theories: Application to an ionic liquid. *J. Chem. Phys.* **140**, 184503 (2014); DOI: 10.1063/1.4874155

Section 6

Sonja Gabl, Christian Schröder, and Othmar Steinhauser. On the solvation dynamics of coumarin C153 in ionic liquids: Comparison of non-

equilibrium simulation to equilibrium simulation and experiment. *Intended for submission to 'The Journal of Chemical Physics'*

For the listed articles, I did the entire analysis all on my own as well as MD simulations, with the exception of Section 5. O. Steinhauser provided assistance in the design of the studies, in the derivation and development of the underlying theory and interpretation of results. C. Schröder helped with the set up of the MD simulations and the interpretation of results.

Furthermore, my studies profited from the reviews and discussions with the entire team each week: O. Steinhauser, C. Schröder, M. Schmollngruber and D. Braun.

3 Computational studies of ionic liquids: Size does matter and time too

Reprinted with permission from *The Journal of Chemical Physics* **137**, 094501 (2012); DOI: 10.1063/1.4748352. Copyright 2012, AIP Publishing LLC.

Computational studies of ionic liquids: Size does matter and time too

Sonja Gabl, Christian Schröder, and Othmar Steinhauser

Citation: The Journal of Chemical Physics **137**, 094501 (2012); doi: 10.1063/1.4748352
View online: http://dx.doi.org/10.1063/1.4748352
View Table of Contents: http://scitation.aip.org/content/aip/journal/jcp/137/9?ver=pdfcov
Published by the AIP Publishing

Articles you may be interested in

Insights on cholinium- and piperazinium-based ionic liquids under external electric fields: A molecular dynamics study
J. Chem. Phys. **139**, 224502 (2013); 10.1063/1.4839635

Slippage and viscosity predictions in carbon micropores and their influence on CO2 and CH4 transport
J. Chem. Phys. **138**, 064705 (2013); 10.1063/1.4790658

Ab initio molecular dynamics simulation of ionic liquids
J. Chem. Phys. **126**, 154502 (2007); 10.1063/1.2718531

Collective excitations in an ionic liquid
J. Chem. Phys. **124**, 074513 (2006); 10.1063/1.2172602

Diffusion mechanisms in under-cooled binary liquids
AIP Conf. Proc. **469**, 398 (1999); 10.1063/1.58469

This article is copyrighted as indicated in the article. Reuse of AIP content is subject to the terms at: http://scitation.aip.org/termsconditions. Downloaded to IP: 131.130.40.59 On: Tue, 13 May 2014 13:30:09

Computational studies of ionic liquids: Size does matter and time too

Sonja Gabl, Christian Schröder, and Othmar Steinhauser
University of Vienna, Department of Computational Biological Chemistry, Vienna, Austria

(Received 6 July 2012; accepted 14 August 2012; published online 4 September 2012)

Taking the molecular ionic liquid 1-ethyl-3-methylimidazolium triflate as a reference system, the size and time dependence of molecular dynamics simulation studies is analyzed in a systematic way. Based on an all atom force field, trajectories of 70 ns length, covering samples of 8–2000 ion pairs, were generated and analyzed in terms of structure as well as single particle and collective dynamics. Although 50 ion pairs seemed sufficient for structure, at least 500 ion pairs were needed for the correct handling of dynamics. For larger systems a linear regime is found, i.e., the respective dynamical properties are a linear function of the inverse box length. In case of translational diffusion coefficients, this linear relation can be rationalised in hydrodynamic terms. The respective formula is essentially determined by viscosity and the inverse box length. Concerning the time dependence, consistent dynamical properties required a time period of 20–30 ns. Nevertheless, size dependence dominates time dependence and has to be primarily addressed. © *2012 American Institute of Physics*. [http://dx.doi.org/10.1063/1.4748352]

I. INTRODUCTION

Since the constitutive work of Boltzmann[1] published in 1896, we have seen a century of evolution of statistical mechanics based on analytic formulations and derivations. Many authors claim that the Jarzynski equality,[2] derived in 1997, is the last (easy) analytic result of this tradition. With the pioneering work of Alder and Wainwright on hard sphere systems,[3] Rahman[4] and Verlet[5] on Lennard-Jones fluids, Rahman and Stillinger on water,[6] and many others, analytic mean values were replaced by averages over configurations generated by computer simulation of the time evolution of a small ensemble of particles confined to a nanoworld (nanometers and nanoseconds). Thereby, molecular motions were and are studied in full atomistic detail by Newtonian mechanics.

With the green chemistry movement some years later, a fascinating type of condensed matter, molecular ionic liquids (ILs), was placed into the centre of attention. Starting with the pioneering work of Handke and Lynden-Bell,[7] we are now facing a decade of computational studies of ILs. The work of Maginn[8] gives a good summary of what has been going on in molecular dynamics simulation on ILs until then, e.g., force field development, liquid structure and dynamics, solutes in ILs, and ILs in the vapor phase. Molecular dynamics simulation of ILs poses some interesting new challenges, due to the anisotropy of the ions, which keeps them fluid near room temperature. This anisotropy stems from shape forces, modeled by Lennard-Jones potentials, as well as electrostatic forces, describing the interaction between intermolecular charge distributions. It needs sufficiently large samples for the shape anisotropy to die off and switch to the bulk isotropy. Furthermore, long-range electrostatic forces push the system size and in addition, high viscosity expands the simulation period.

These demands on system size and simulation period become even more critical when computing collective properties, which characterise the whole sample by a single number, thus prohibiting averaging over individual particles. This makes it difficult to obtain collective properties with high statistical accuracy. Nevertheless, collective properties are of high interest for the interpretation of experimental data, which normally refer to the whole sample and not to individual particles. Typical examples are conductivity, dielectric spectra, and viscosity.

However, the finiteness of computer resources enforces usage of small, finite samples, whose time evolution can only be studied in a confined time period. Therefore, it is crucial to define a simulation environment, which balances computational costs and accurate simulation results, to minimise finite size effects as well as time effects. The question of finite size effects has been addressed several times, but the findings are often contradictory and incomplete.

Rey-Castro and Vega[9] studied the effect of the system size on transport properties. They state that it is essential to estimate the correct system size to calculate a desired property with enough accuracy at reasonable central processing unit cost. Systems, containing 64, 125, and 216 ion pairs, were simulated and transport properties were calculated. Although statistical uncertainity improved with increasing system size, they could not detect a trend in system size in their results. Pićalek and Kolafa[10] did a similar study using systems with 100, 200, and 400 ion pairs and they could not detect any significant effects as well. The group of Maroncelli[11] did a coarse grained study using a box with 343 ion pairs. To validate the simulation, another one was done with 2744 ion pairs and they could not find differences beyond statistical uncertainities.

Lopes and Pádua[12] reported that the size of the system studied and the duration of the simulation is of particular importance, when it comes to ionic liquids. They simulated different systems, containing 128, 250, and 350 ion pairs. Results were presented only for the largest system, because they appear to have less artificially induced periodic structures. In a second paper,[13] the authors chose again the same amount of ion pairs in a box to calculate equilibrium properties,

 © 2012 American Institute of Physics

This article is copyrighted as indicated in the article. Reuse of AIP content is subject to the terms at: http://scitation.aip.org/termsconditions. Downloaded to IP: 131.130.40.59 On: Tue, 13 May 2014 13:30:09

such as densities, energies, and radial distribution functions (RDFs). Wang and Voth[14,15] investigated ILs using a multiscale coarse-graining method in 2005/2006. They simulated systems with 64, 216, 512, and 1000 ion pairs and computed RDFs. They found out that smaller systems are more ordered, but 64 ion pairs represent a RDF qualitatively well. Further size effects could not be detected. In 2007, Voth and coworkers[16] discussed finite size effects more thoroughly. They simulated 64 and 512 ion pairs and, furthermore, they also varied the alkyl chain length of the cation. They proposed that systems with longer alkyl chain may have more significant finite size effect in a finite simulation box, which may be big enough for systems with shorter chains. This is due to the fact that longer alkyl chains are more flexible and can bend to form many different shapes, so that the distance between the two terminals can range more widely. Therefore, obtaining fully equilibrated IL systems with reasonably large simulation size is not an easy task. Although quantitatively different, the RDFs and the diffusion coefficient for these two sizes give the same qualitative results for local structure and dynamics. In contrast, the finite size effect is so large for the global heterogeneity distributions in ILs that the results from the small-sized systems would give a false impression. Thus, the finite size effect has a large influence on the global heterogeneity of ILs. It also likely suggests that the characteristic correlation length for global heterogeneity is longer than that for local structure and that for diffusion. Bagno and coworkers[17] simulated 25, 27, 61, 64, and 125 ions pairs to calculate diffusion coefficients. They detected a significant effect of the box size on the (MSD). Diffusion coefficients are strongly underestimated with respect to the experimental value. They say, fluctuations in the diffusion coefficient as a function of the box size do not depend on local structure, which is confirmed by radial distribution functions. Hu and Margulis[18,19] calculated viscosities via equilibrium molecular dynamics and nonequilibrium molecular dynamics. They simulated 343, 2744, and 8232 ion pairs and they could not reach the hydrodynamic limit. Nevertheless, they were able to produce viscosities for the larger systems using nonequilibrium molecular dynamics. In the work of Borodin[20] various ILs were simulated. Thereby, the box size ranged from 34 to 44 Å (100–216 ion pairs). Borodin applied a correction[21] for the self-diffusion coefficient, which is typically around 10%–20%. He also states that one has to simulate longer than 200 ps for the self-diffusion coefficient, otherwise it will be calculated from the subdiffusive regime and therefore overestimated by approximately 50%. Applying the correction on the diffusion coefficient, he does not detect any finite size effects for systems up to 216 ion pairs.

The subject of system size dependence was not addressed for the first time with the appearance of ILs. In 2004, Yeh and Hummer[22] did an extensive study on size dependence of diffusion coefficients of TIP3P-water with periodic boundary conditions (PCB). They reported that there is a dependence of the diffusion coefficient and one can apply a correction.[21] Furthermore, they found out that viscosities do not suffer any significant size dependence.

Having already a size dependence in the water model TIP3P, we have evidence that this is valid for molecular ionic liquids too. To get rid of the inconsistencies in the publications mentioned above, we tried to give a more detailed study on finite size and time effects of the unpolarised IL $EMIM^+CF_3SO_3^-$ in Secs. II–VIII. Systems, consisting of 8–2000 ion pairs, were simulated for 70 ns and information on structure and dynamics, single particle as well as collective, was gained. We will show that there is a systematic relation between different system sizes. We applied a correction for the self-diffusion coefficient, which has its seeds in hydrodynamics. An alternative route to viscosity is given in the same context. In Sec. VII, we will discuss the influence of simulation length on results.

II. METHODS

All simulations were performed with the program package Chemistry at Harvard Molecular Mechanics (CHARMM).[23,24] Each trajectory totalled 70 ns and was generated under constant volume and a temperature of 300 K. The timestep was 1 fs. Lennard-Jones energies and forces were smoothly switched off between 9 and 10 Å. For the electrostatic interactions the particle mesh Ewald method[25,26] was used with a cutoff of 10 Å. The real space part was calculated with a κ of 0.41 $Å^{-1}$. For the number of grid points, used for each simulation, please refer to Table I, the charges on the grid were interpolated by sixth-order spline. The nonbonded and image lists used a 14 Å cut-off distance and were heuristically updated. The SHAKE algorithm[27] was used to hold the bond lengths fixed, but not the bond angles or dihedrals. The force field parameters for the cation $EMIM^+$ were taken from Refs. 28 and 29, whereas the parameters for the anion $CF_3SO_3^-$ stem from Refs. 30 and 31 and from the standard CHARMM force field[23,32] as well.

The program PACKMOL[33] was used to pack the various systems of $EMIM^+CF_3SO_3^-$ into cubic boxes according to the experimental density from Ref. 34. The box length of each system used for the packing and the following simulation can be seen in Table I. After the packing process, the resulting pdb files from PACKMOL were converted to crd files (CHARMM standard coordinate files) and minimised by the steepest descent method until reasonably energies were reached. Determining the minimisation, the boxes were ready for simulation.

As a first indication of system size behaviour, we have included the Lennard-Jones and Coulomb energies as well as their sum, the total potential energy, in Table I. All quantities were normalised by the respective volume in order to give intensive quantities. As they represent double averages, both in space and time, they are—in our opinion—too insensitive for discussion of size and time dependence.

III. PACKING AND COLLECTIVE ORIENTATIONAL STRUCTURE

As a starting point of our analysis we would like to give the RDFs

$$g_{\alpha\beta}^{000}(r) = \frac{1}{4\pi\rho r^2 dr} \sum_i \sum_{j\neq i} \langle 1 \cdot \delta(\vec{r} - \vec{r}_{ij}) \rangle, \qquad (1)$$

This article is copyrighted as indicated in the article. Reuse of AIP content is subject to the terms at: http://scitation.aip.org/termsconditions. Downloaded to IP: 131.130.40.59 On: Tue, 13 May 2014 13:30:09

TABLE I. This table gives for each system size the according values of various properties.

No. of ion pairs	8	10	20	30	40	50	100	200	300	500	750	1000	2000
Box length [Å]	13.6	14.6	18.4	21.1	23.2	25.0	31.5	39.7	45.4	53.8	61.6	67.8	85.5
Grid points	12	12	16	20	20	24	24	36	40	48	60	64	80
U_{LJ}/V [10^{-2} kcal]	−6.03	−5.88	−5.74	−5.66	−5.63	−5.67	−5.84	−5.79	−5.82	−5.86	−5.81	−5.85	−5.79
U_{Coul}/V [10^{-2} kcal]	8.89	9.65	8.99	9.68	9.45	9.82	9.46	9.47	9.53	9.54	9.50	9.48	9.46
U_{pot}/V [10^{-2} kcal]	2.86	3.77	3.26	4.02	3.83	4.15	3.62	3.67	3.71	3.69	3.69	3.63	3.67
G_K^{--}	…	…	…	…	…	0.573	0.566	0.543	0.522	0.541	0.537	0.528	0.523
$\langle\tau_{M_D}^{++}\rangle$ [ps]	…	…	…	…	…	1927.8	3544.1	2177.8	2196.7	3582.9	2631.6	2509.4	1821.6
$\langle\tau_{M_D}^{--}\rangle$ [ps]	…	…	…	…	…	536.2	361.5	402.3	345.0	581.5	441.2	344.3	299.6
$\langle\tau_{SP}^{++}\rangle$ [ps]	…	…	…	…	…	3019.3	2526.7	2610.2	2911.4	2928.1	2964.7	2764.4	2526.2
$\langle\tau_{SP}^{--}\rangle$ [ps]	…	…	…	…	…	1727.6	1567.8	1493.3	1569.5	1739.1	1779.7	1599.5	1473.3
D^+ [10^{-8}cm^{2}s^{-1}]	…	…	…	…	…	5.29	8.85	6.48	6.31	5.76	5.91	6.13	6.82
D^- [10^{-8}cm^2 s^{-1}]	…	…	…	…	…	2.22	4.61	2.14	1.93	1.91	1.78	2.03	2.24
$\sigma(0)$ [Sm^{-1}]	…	…	…	…	…	0.146	0.118	0.242	0.179	0.122	0.162	0.173	0.218
η [cP]	…	…	…	…	…	127.8	−192.2	112.7	86.5	61.8	54.4	56.5	62.1

describing the mutual packing of cations and anions ($\alpha\beta$ = (− −), (+ −), (+ +)) in terms of their centre of mass $\vec{r}_{i,cm}$. In Fig. 1, the presentation of these RDFs was splitted into systems with a low number of ion pairs (≤50) and otherwise up to 2000 ion pairs. This distinction was made because 50 ion pairs seemed to be a critical size to avoid artifacts. Smaller systems are plagued by distortions resembling rigidified structures. This circumstance has already been described by Lopes and Pádua[12,13] as well as Voth and co-workers.[14–16]

Due to the fact that structural properties are usually less sensitive to system parameters than dynamical properties discussed below, we therefore restrict our further analysis to systems larger than 50 ion pairs. For the larger systems, the asymptotic behaviour clearly depends on system size: A monotonic decay from half of the boxlength ($r = L/2$) to zero at $r = \sqrt{3}L/2$ is observed and stems from the incomplete spherical shells in the corners of the cube. However, the structure within the inscribed sphere for $r < L/2$ is preserved.

Reducing anisotropic molecules to just a point or a molecular centre is an oversimplification. As the first step to include anisotropy, we generalised the simple RDF g^{000} to the dipolar RDF

$$g_{\alpha\beta}^{110}(r) = \frac{1}{4\pi\rho r^2 dr} \sum_i \sum_{j\neq i} \left\langle \hat{\mu}_i^\alpha \hat{\mu}_j^\beta \cdot \delta(\vec{r} - \vec{r}_{ij}) \right\rangle. \qquad (2)$$

This is achieved replacing unity in the simple RDF by the scalar product $\hat{\mu}_i^\alpha \cdot \hat{\mu}_j^\beta$, representing the cosine between the dipole axes, $\hat{\mu}_i^\alpha$ and $\hat{\mu}_j^\beta$, of two ions. In this way one gets information about the average cosine and thus the mutual orientation of two dipoles. In Fig. 2 to the left, the dipolar RDF of the anion pair $CF_3SO_3^-$-$CF_3SO_3^-$ is shown. The pronounced negative region at short distances is indicative of a strong antiparallel alignment of molecular axes, which coincide with the dipolar axes. The antiparallel alignment is enforced by the shape anisotropy of $CF_3SO_3^-$-ions, thus enabling optimal and dense packing. The first step from a pairwise description to a collective picture can be demonstrated by the so-called

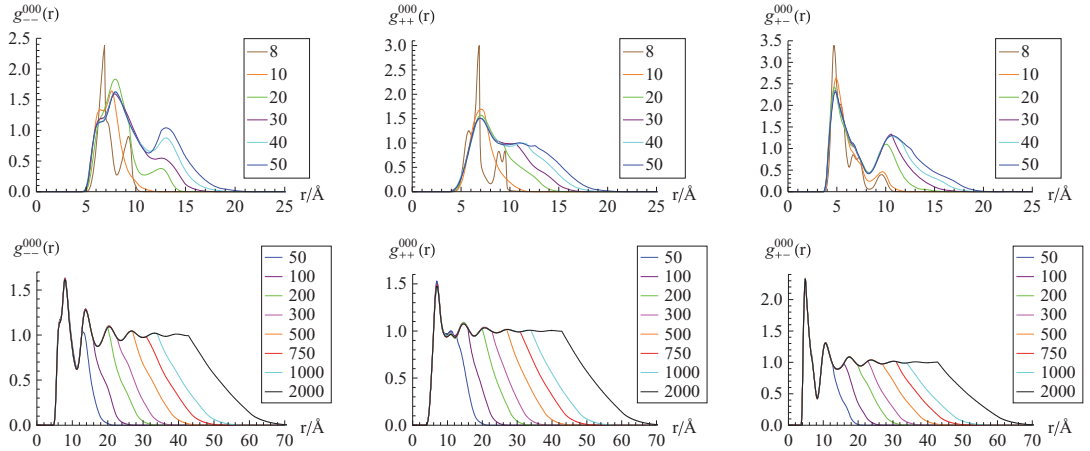

FIG. 1. Centre of mass radial distribution functions of $EMIM^+CF_3SO_3^-$. The first row is dedicated to the small systems, whereas the second row shows systems beyond 50 ion pairs.

This article is copyrighted as indicated in the article. Reuse of AIP content is subject to the terms at: http://scitation.aip.org/termsconditions. Downloaded to IP: 131.130.40.59 On: Tue, 13 May 2014 13:30:09

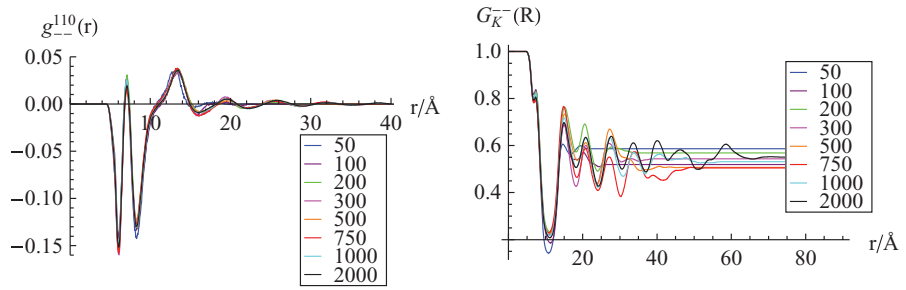

FIG. 2. The anion-anion dipolar RDF is to the left. The respective running integral from Eq. (3) is to the right.

Kirkwood G_K-factor[35]

$$G_K^{\alpha\beta}(R) = 1 + \rho \int_0^R g^{110}(r)\, 4\pi r^2 \mathrm{d}r, \tag{3}$$

which accumulates the average cosine of dipolar orientation from each spherical shell extending from r to $r + dr$. The weighting by the respective shell volume of $4\pi r^2 dr$ amplifies even the modest contribution from distant shells (Fig. 2 to the right).

Such a description in terms of spherical shells finds its limits for distances $R = L/2$ larger than one half of the box length, where these shells become incomplete. This incompleteness may be overcome by an alternative formulation,

$$G_K^{\alpha\beta}(R) = \int_0^R \frac{1}{N} \sum_i \sum_j \langle \hat{\mu}_i^\alpha \hat{\mu}_j^\beta \rangle \delta(r - r_{ij})\, \mathrm{d}r \tag{4}$$

$$= \frac{1}{N} \sum_i \sum_{\substack{j \\ r_{ij} < R}} \langle \hat{\mu}_i^\alpha \hat{\mu}_j^\beta \rangle \tag{5}$$

$$= \frac{1}{N\mu_\alpha \mu_\beta} \sum_{i=1}^{N} \langle \vec{\mu}_i^\alpha \cdot \vec{M}_D^\beta(R) \rangle, \tag{6}$$

where in the last step we have introduced the total rotational dipole moment $\vec{M}_D^\beta$ of the sample of species β, explained in detail at the beginning of Sec. IV. With this reformulation the asymptotic limit

$$\lim_{R \to R_{\max}} G_K^{\alpha\beta}(R) = \frac{\langle \vec{M}_D^\alpha \cdot \vec{M}_D^\beta \rangle}{N\mu_\alpha \mu_\beta} \tag{7}$$

can be directly calculated, where $\langle \vec{M}_D^\alpha \cdot \vec{M}_D^\beta \rangle$ is the starting point of the time correlation function of the rotational dipole moment, explained in detail in Sec. IV. These asymptotic values as a function of the inverse box length is shown in Fig. 3. A more or less monotonic decay is observed, which seems to become linear for the larger systems. This linear behaviour is intrinsically connected to the inverse box length $1/L$. It disappears when using the volume V or the box length L instead. For the larger systems an appropriate linear fit yields both, the slope and the intercept. The latter gives the "apparent" value for the "infinite" system.

IV. COLLECTIVE AND SINGLE PARTICLE ROTATION

From a principal point of view, ionic liquids can be described as an ensemble of atomic charges $\{q_{i,a}\}$ located at the position $\{\vec{r}_{i,a}\}$ of atom a in molecule i with its centre of mass at $\vec{r}_i$. Quite often experimental results are related to global properties, rather than single particle data. A typical global property of such a system is the total dipole moment

$$\vec{M}_{tot} = \sum_i \sum_a q_{i,a} \vec{r}_{i,a}. \tag{8}$$

As the ensemble consists of pairs of cations and anions we have charge neutrality, i.e., the total sum of charges

$$Q = \sum_i q_i = \sum_i \left(\sum_a q_{i,a} \right) = 0, \tag{9}$$

making $\vec{M}_{tot}$ independent of origin.

For detailed interpretation, it is convenient to decompose $\vec{M}_{tot}$ into a translational component

$$\vec{M}_J = \sum_i q_i \vec{r}_i \tag{10}$$

and a rotational part

$$\vec{M}_D = \vec{M}_{tot} - \vec{M}_J = \sum_i \left(\sum_\alpha q_{i,a} (\vec{r}_{i,a} - \vec{r}_i) \right) = \sum_i \vec{\mu}_i, \tag{11}$$

which also includes internal motion. As both, $\vec{M}_{tot}$ and $\vec{M}_J$, refer to neutral charge ensembles and are therefore

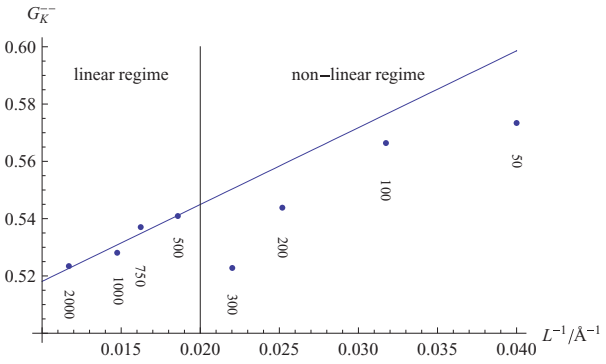

FIG. 3. The asymptotic values from Eq. (7) are plotted versus the inverse box length.

This article is copyrighted as indicated in the article. Reuse of AIP content is subject to the terms at: http://scitation.aip.org/termsconditions. Downloaded to IP: 131.130.40.59 On: Tue, 13 May 2014 13:30:09

independent of origin, the same is true for the rotational part of $\vec{M}_D$. In contrast, molecular dipole moments $\vec{\mu}_i$ depend on the respective reference point $\vec{r}_i$, in our case the centre of mass. Nevertheless, they are used quite often for interpretation.

For a constant charge set $\{q_{i,a}\}$ temporal fluctuations of $\vec{M}_D$ are caused by the atomic motion, i.e., the change of the coordinates $\vec{r}_{i,a}$. Traditionally, fluctuations of a dynamic variable are characterised by the respective time correlation function $\langle \vec{M}_D(0)\vec{M}_D(t)\rangle$. Its initial, static value $\langle \vec{M}_D^2\rangle$ is related to the asymptotic Kirkwood G_K-factor, already introduced in Sec. III (Eq. (7)). For the interpretation of its temporal behaviour various types of fit functions can be used. Looking for a fit function that matches the complex dynamics with a minimum number of parameters, the Kohlrausch-William-Watts (KWW)-function

$$f_{KWW}(t) = Ae^{(-t/\tau)^\beta} \tag{12}$$

with an average relaxation constant of

$$\langle\tau\rangle = \frac{\tau}{\beta}\Gamma\left(\frac{1}{\beta}\right) \tag{13}$$

turned out to be best suited in our case. In order to characterise the correlation function by a single number, we have computed the average relaxation time $\langle\tau_{M_D}\rangle$ defined in Eq. (13). For the complete system, $\langle\tau_{M_D}\rangle$ did not show any systematic behaviour. Therefore, we splitted $\vec{M}_D$ into separate contributions from cations and anions

$$\vec{M}_D(t) = \vec{M}_D^+(t) + \vec{M}_D^-(t), \tag{14}$$

which implies for the correlation function

$$\langle \vec{M}_D(0)\vec{M}_D(t)\rangle = \langle \vec{M}_D^+(0)\vec{M}_D^+(t)\rangle + \langle \vec{M}_D^-(0)\vec{M}_D^-(t)\rangle + 2\langle \vec{M}_D^+(0)\vec{M}_D^-(t)\rangle. \tag{15}$$

Figure 4 shows the average relaxation time, $\langle\tau_{M_D}^{++}\rangle$ (orange) and $\langle\tau_{M_D}^{--}\rangle$ (cyan), as a function of the inverse box length for the two self-terms $(++, --)$. For the smaller systems, the behaviour is again unsystematic, but for the largest systems a linear relation is found as already observed for the static anionic G_K-factor (Fig. 3). At this point we emphasise that we have a linear relation for both, the static anionic collective G_K-factor as well as the average relaxation times, $\langle\tau_{M_D}^{++}\rangle$ and $\langle\tau_{M_D}^{--}\rangle$. The larger the system, the faster is the overall collective rotation. Therefore, we have now two indicators, static and dynamic, for the overstabilisation of small systems.

The splitting of $\langle \vec{M}_D^\alpha(0)\vec{M}_D^\beta(t)\rangle$ into contributions from ionic species may be continued to the molecular level

$$\langle \vec{M}_D^\alpha(0)\vec{M}_D^\beta(t)\rangle = \sum_i \langle \vec{\mu}_i^\alpha(0)\vec{\mu}_i^\beta(t)\rangle + \sum_i \sum_{j\neq i} \langle \vec{\mu}_i^\alpha(0)\vec{\mu}_j^\beta(t)\rangle. \tag{16}$$

The single particle time correlation functions $\langle \vec{\mu}_i(0)\vec{\mu}_i(t)\rangle$ can again be fitted to a KWW-function (Eq. (13)). The respective average relaxation times, $\langle\tau_{SP}^{++}\rangle$ (red) and $\langle\tau_{SP}^{--}\rangle$ (blue), are also plotted as a function of the inverse box length in Fig. 4. In the linear regime, their size dependence is analogous to the collective relaxation times. Indeed, the actual numerical values are comparable for the collective relaxation time,

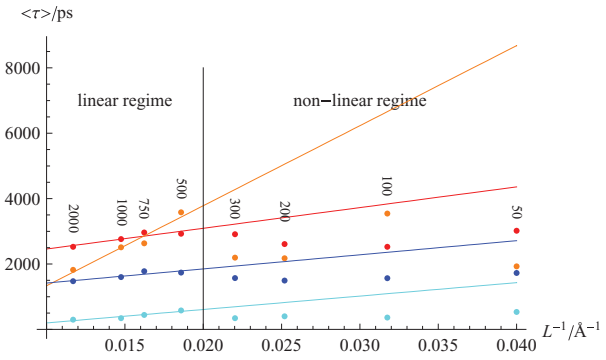

FIG. 4. The average relaxation times for the cation are given in orange (collective) and red (single particle), whereas the times for the anion are displayed in cyan (collective) and blue (single particle).

$\langle\tau_{M_D}^{++}\rangle$, and the single particle relaxation time, $\langle\tau_{SP}^{++}\rangle$, in case of the cations. In contrast, the collective relaxation time $\langle\tau_{M_D}^{--}\rangle$ is four times faster than the single particle relaxation time $\langle\tau_{SP}^{--}\rangle$. This empirical scaling law of single particle and collective rotational dynamics can be rationalised by the generalised Kivelson-Madden relation[36]

$$\langle\tau_{M_D}^{++}\rangle = G_K^{++}\langle\tau_{SP}^{++}\rangle, \tag{17}$$

$$\langle\tau_{M_D}^{--}\rangle = G_K^{--}\langle\tau_{SP}^{--}\rangle. \tag{18}$$

In this context, the term "generalised" means that the original Kivelson-Madden relation[37] was derived for monoexponential correlation functions and homogeneous systems consisting of a single molecular species. We applied it here to the average relaxation time of KWW-functions and to systems consisting of two species. So far, we have not considered the G_K-factor of the cations, because it is close to unity. This comes from the weak coupling of the cationic dipoles, such that their orientational order is almost randomised by thermal motion. In contrast, the dumbbell shape of the anions enforces an antiparallel alignment of neighbouring molecules. An optimal packing of dumbbells is achieved when the head or tail of a neighbouring dumbbell is closest to the centre of the reference dumbbell. In this configuration the interaction energy is optimal for an antiparallel alignment. There, we meet the general principle that spatial arrangements of molecules are dominated by shape forces first and subsequently are fine tuned by electrostatic forces, which finally results in the closest proximity of the head of an anion to the tail of a neighbour. Altogether, this reduces the G_K-factor of the anions to a value substantially below unity. Believing in the generalised Kivelson-Madden relation, one would expect that collective and single particle relaxation times are almost equal in case of cations, while the collective rotational dynamics of anions is accelerated by the amount of the respective G_K-factor. Collective rotational dynamics should be twice as fast as the single particle dynamics. Our Fig. 4 confirms this view at least in a qualitative sense. In other words, the static collective G_K-factor can absorb the dynamic contributions from the cross terms, $\langle \vec{\mu}_i(0)\vec{\mu}_j(t)\rangle$.

This article is copyrighted as indicated in the article. Reuse of AIP content is subject to the terms at: http://scitation.aip.org/termsconditions. Downloaded to IP: 131.130.40.59 On: Tue, 13 May 2014 13:30:09

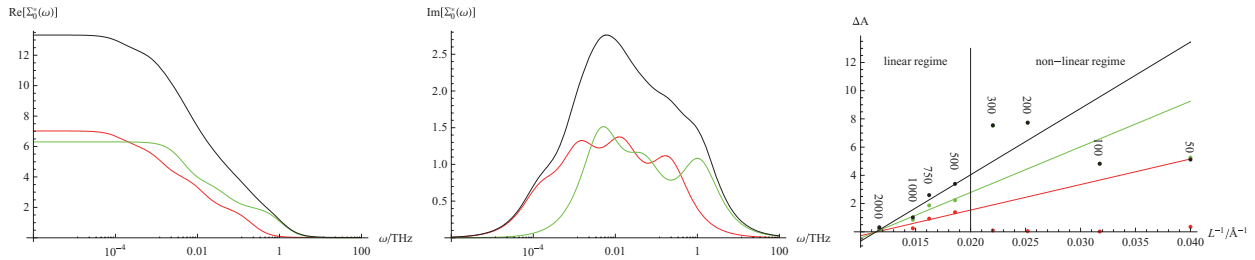

FIG. 5. For the system $N = 2000$ the real part (dielectric dispersion) is given to the left and the imaginary part (dielectric loss) in the middle. The values for the absolute deviation areas can be found to the right, plotted versus the inverse box length. The rotational part is always shown as a red line, whereas the translational part is a green line. The sum is displayed in black.

So far, we have characterised $\langle \vec{M}_D(0)\vec{M}_D(t)\rangle$ on the average. We now analyze its full time dependence, but we transform to Fourier space in order to be closer to the experimental situation. Indeed, the rotational part of the dielectric spectrum is given by the Fourier-Laplace transform

$$\epsilon(\omega) - 1 = \frac{4\pi}{3Vk_BT}\left[\langle \vec{M}_D^2\rangle + i\omega\int_0^\infty dt e^{i\omega t}\langle \vec{M}_D(0)\vec{M}_D(t)\rangle\right]. \tag{19}$$

As there is no analytic Fourier transform of the KWW-function, we used a multiexponential fit $\sum_k A_k \exp(-t/\tau_k)$ instead

$$\epsilon(\omega) - 1 = \sum_k \frac{A_k}{1 - i\omega\tau_k}. \tag{20}$$

For the largest system ($N = 2000$), Fig. 5 presents in red the real part (dielectric dispersion) to the left and the imaginary part (dielectric loss) in the middle. In order to find a simple measure for comparison of a set of dielectric functions referring to systems of different size, we introduce the absolute deviation area

$$\Delta A = \int |A(\omega) - A_{2000}(\omega)| d\omega. \tag{21}$$

Here, $A_{2000}(\omega)$ is the rotational dielectric function $\epsilon(\omega) - 1$ of the reference system, which contains 2000 ion pairs simulated for 70 ns. Because of its maximum extension in size and time, we have compared every other system $A(\omega)$ to this reference. The resulting deviation areas are depicted in Fig. 5 (right) as a function of the inverse box length. For the largest systems, a linear regime was found again.

V. TRANSLATION AND SINGLE PARTICLE DIFFUSION

The collective dipole moment $\vec{M}_J$ (Eq. (10)) is the translational analog of $\vec{M}_D$. Both together constitute the total collective dipole moment $\vec{M}_{tot}$ (Eq. (11)). Consequently, the Fourier-Laplace transform $\vartheta(\omega)$ of the time correlation function $\langle \vec{M}_J(0)\vec{M}_J(t)\rangle$ complements the rotational part $\epsilon(\omega) - 1$, already discussed above, to the full generalised dielectric constant $\Sigma(\omega)$,

$$\Sigma(\omega) = \epsilon(\omega) - 1 + \vartheta(\omega). \tag{22}$$

In principle, we have this formal analogy of rotational and translational spectra. In practice, however, a static ($\omega = 0$) electric field induces an electric current

$$\vec{J}(t) = \frac{d}{dt}\vec{M}_J(t) = \sum_i q_i \vec{v}_i(t) \tag{23}$$

in systems with charge carriers. This current is experimentally accessible via the dielectric conductivity

$$\sigma(\omega) = \frac{1}{3Vk_BT}\int_0^\infty dt e^{i\omega t}\langle \vec{J}(0)\vec{J}(t)\rangle. \tag{24}$$

Its static value $\sigma(0)$ leads to a parabola $4\pi i\sigma(0)/\omega$ in the imaginary part of the $\vartheta(\omega)$. In experimental spectra as well as in our simulated spectra this parabola is subtracted

$$\vartheta_0(\omega) = \vartheta(\omega) - \frac{4\pi i\sigma(0)}{\omega} = 4\pi i\frac{\sigma(\omega) - \sigma(0)}{\omega}. \tag{25}$$

As the current $\vec{J}(t)$ is the time derivative of the collective translational dipole moment $\vec{M}_J(t)$, the respective correlation functions are related by

$$\langle \vec{J}(0)\vec{J}(t)\rangle = -\frac{d^2}{dt^2}\langle \vec{M}_J(0)\vec{M}_J(t)\rangle = \frac{1}{2}\frac{d^2}{dt^2}\left\langle \Delta\vec{M}_J^2(t)\right\rangle. \tag{26}$$

In the last step, we also introduced the dipolar displacement

$$\left\langle \Delta\vec{M}_J^2(t)\right\rangle = \langle[\vec{M}_J(t) - \vec{M}_J(0)]^2\rangle. \tag{27}$$

Combining all these relations in an appropriate manner, the translational part of the dielectric spectrum, the so-called dielectric conductivity, is given by

$$\vartheta_0(\omega) = \frac{4\pi}{3Vk_BT}\frac{i}{\omega}\int_0^\infty dt(e^{i\omega t} - 1)\frac{1}{2}\frac{d^2}{dt^2}\left\langle \Delta\vec{M}_J^2(t)\right\rangle. \tag{28}$$

In order to compute the actual spectrum, we used again a fit function

$$\left\langle \Delta\vec{M}_J^2(t)\right\rangle = \sum_l (B_l(1 - e^{-t/\tau_l})) + 6Vk_BT\sigma(0)t. \tag{29}$$

While the short time behaviour of the dipolar displacement is described by the amplitudes B_l and the relaxation times τ_l, the conductivity $\sigma(0)$ describes the long time regime. As it is the second time derivative of the dipolar displacement that enters the dielectric conductivity (Eq. (28)), the asymptotic linear part of the dipolar displacement is automatically annihilated and we get

$$\vartheta_0(0) = \frac{1}{2}\sum_l \frac{B_l}{1 - i\omega\tau_l}. \tag{30}$$

This article is copyrighted as indicated in the article. Reuse of AIP content is subject to the terms at: http://scitation.aip.org/termsconditions. Downloaded to IP: 131.130.40.59 On: Tue, 13 May 2014 13:30:09

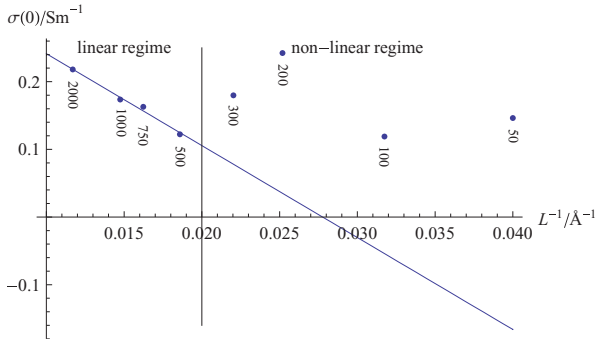

FIG. 6. The static conductivity $\sigma(0)$ plotted versus the inverse box length.

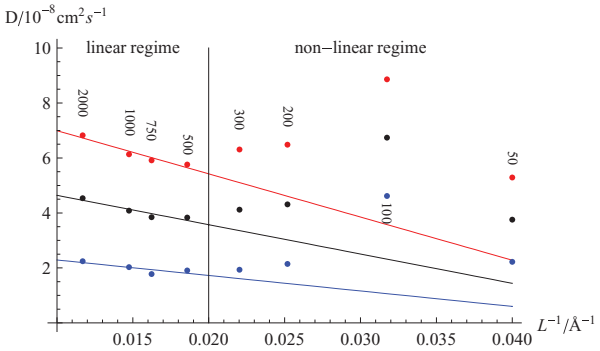

FIG. 8. The diffusion coefficient for the cation is shown in red, for the anion it is in blue, and the averaged diffusion coefficient is shown in black.

The numerical result for the largest system ($N = 2000$) for 70 ns is shown in Fig. 5 (left and middle part). The sum $\Sigma(\omega)$ of dielectric permittivity $\epsilon(\omega) - 1$ and the dielectric conductivity $\vartheta_0(\omega)$ is also given. The respective deviation areas, defined in Eq. (21), are displayed in Fig. 5 to the right. While being unsystematic for the smaller systems, a linear regime finally evolves. This asymptotic linear regime becomes more evident in Fig. 6, when plotting the values for the static conductivity $\sigma(0)$ versus the inverse box length.

Combining relations Eqs. (10) and (27), the collective dipolar displacement $\langle \Delta \vec{M}_J^2(t) \rangle$ may be expressed as a double sum over the net charge q_i and the centre of mass $\vec{r}_i$ of all molecular ions. This double sum can be separated into self- (S) and cross terms (C).

$$\langle \Delta \vec{M}_J^2(t) \rangle = \left[\langle \Delta \vec{M}_J^2(t) \rangle \right]_S + \left[\langle \Delta \vec{M}_J^2(t) \rangle \right]_C, \tag{31}$$

$$\left[\langle \Delta \vec{M}_J^2(t) \rangle \right]_S = \sum_i q_i^2 \langle [\vec{r}_i(t) - \vec{r}_i(0)]^2 \rangle, \tag{32}$$

$$\left[\langle \Delta \vec{M}_J^2(t) \rangle \right]_C = \sum_i \sum_{j \neq i} q_i q_j \langle [\vec{r}_i(t) - \vec{r}_i(0)][\vec{r}_j(t) - \vec{r}_j(0)] \rangle. \tag{33}$$

The self-term $[\langle \Delta \vec{M}_J^2(t) \rangle]_S$ retains diagonal terms $i = j$ only, thus neglecting correlations between particles. For equally charged cations and anions $q_i^2 = q^2$ the self-term is the sum of the average of all individual MSDs $\langle [\vec{r}_i(t) - \vec{r}_i(0)]^2 \rangle$, irrespective of the ionic type. In other words, one would approximate $\langle \Delta \vec{M}_J^2(t) \rangle$ by the average MSD multiplied by q^2. In Fig. 7 this approximation is compared to the full dipolar displacement. Depending on the time period considered, the performance of the self-term is quite different. Surveying a period of 20 ns (cf. middle part of Fig. 7), it seems to perform reasonably. Zooming to the initial period (cf. left part of Fig. 7), however, deficiencies become clearly visible. The discrepancy between $\langle \Delta \vec{M}_J^2(t) \rangle$ and average MSD $\cdot\ q^2$ can be accredited to the neglect of the cross-terms. It is evident, that the cross-terms have a great influence on $\langle \Delta \vec{M}_J^2(t) \rangle$. This rules out any possibilities to compute the translational part of the dielectric spectrum, the so-called dielectric conductivity, from single particle contributions alone. The importance of statistical accuracy of collective properties is displayed in the right part of Fig. 7. In addition, one can see the necessity of extremely long simulation periods, which are required to produce reliable results.

Having discussed the transition from collective translational motion to the single particle mean squared displacement, we now consider the diffusion coefficients, which can be calculated from the linear regime of the MSD

$$\langle [\vec{r}_i(t) - \vec{r}_i(0)]^2 \rangle \to 6Dt. \tag{34}$$

The size dependence of the cationic and anionic diffusion coefficient D^+ and D^- can be found in Fig. 8 in red and blue, the averaged diffusion coefficient $D = 1/2(D^+ + D^-)$ is displayed in black. In any case, the largest systems exhibit a linear behaviour.

The size dependence reported by Bagno and coworkers,[17] 25–125 ion pairs, is therefore due to mere statistical uncertainities. The same can be said for Borodin,[20] who simulated up to 216 ion pairs. In both publications the authors were not able to reach the linear regime.

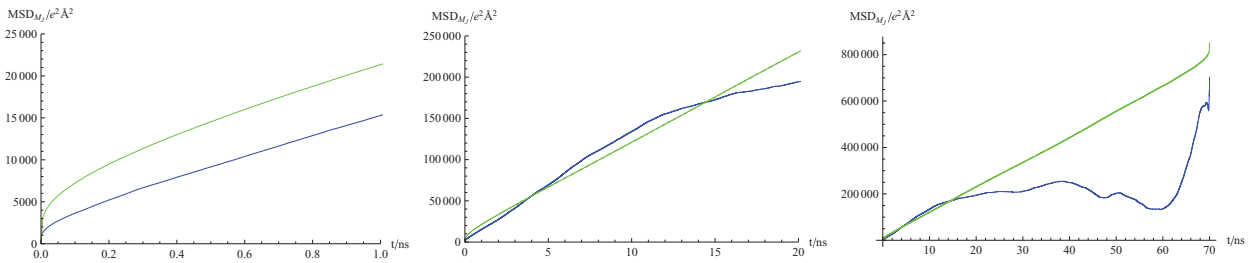

FIG. 7. The collective dipolar displacement $\langle \Delta \vec{M}_J^2(t) \rangle$ is shown in blue, whereas the average MSD multiplied by q^2 is shown in green for $N = 2000$. The initial period is to the left, the whole trajectory length to the right, and a 20 ns slice can be found in the middle.

This article is copyrighted as indicated in the article. Reuse of AIP content is subject to the terms at: http://scitation.aip.org/termsconditions. Downloaded to IP: 131.130.40.59 On: Tue, 13 May 2014 13:30:09

To conclude this chapter, we shift the asymptotic linearity of the diffusion coefficient to the mean single particle reorientation time $\langle\tau\rangle$ by the observation that the product

$$D * \langle\tau\rangle = const. \tag{35}$$

is fairly constant in the linear regime, but varies for systems smaller than 500 ion pairs (data not shown).

VI. HYDRODYNAMIC EXPLANATION AND THE ROLE OF VISCOSITY

So far we have found that a variety of properties shows a linear dependence on the inverse box length $x = 1/L$, provided the system is sufficiently large. Since every property has to be a function $f(x)$ of the inverse box length, the linear regime may be realised by a truncated Taylor series

$$f(x) = f(0) + f'(0)x + O(x^2). \tag{36}$$

Of course, one can use this linear relation for the extrapolation to the infinite system value $f(0)$, but we have no criteria, which system size is large enough to fall in the linear regime. Though we think that the beginning of the linear regime is influenced by viscosity. The more viscous the system, the more molecules have to be included in the simulation box to be able to enter the linear regime. Indications in that direction can be found in the work of Yeh and Hummer[22] on water. They simulated 128 water molecules, which sufficed to enter the linear regime. In our case, we simulated systems of $EMIM^+CF_3SO_3^-$, which are characterised by higher viscosity. Consequently, we needed approximately 500 ion pairs to enter the linear regime.

To understand the linear behaviour in physical terms, the concept of hydrodynamics[38] is consulted, which has often been used for the explanation of principal phenomena in molecular systems. In our case the transition from the molecular world to hydrodynamics is mediated by the interparticle diffusion tensor

$$D_{ij}^{\gamma\delta} = \int_0^\infty \left\langle v_i^\gamma(0) v_j^\delta(t)\right\rangle dt = D^{\gamma\delta}(\vec{r}_i - \vec{r}_j). \tag{37}$$

Here the subscripts i, j refer to pairs of molecular centres $\vec{r}_i, \vec{r}_j$, while the superscripts γ, δ denote the Cartesian tensor components. The special case of the self-diffusion tensor is obtained by taking the zero distance limit

$$D_{ii}^{\gamma\delta} = \lim_{\vec{r}\to 0} D^{\gamma\delta}(\vec{r}). \tag{38}$$

In hydrodynamics the velocity flow field $\vec{u}(r,t)$ replaces the molecular velocities $\vec{v}_i = \vec{p}_i/m_i$. The link between both worlds is given by

$$u^\gamma(\vec{r},t) = \frac{V}{N}\sum_i \frac{p_i^\gamma}{m_i}\delta(\vec{r} - \vec{r}_i). \tag{39}$$

The diffusion tensor in hydrodynamic terms can now be written as

$$D^{\gamma\delta}(\vec{r}) = \int_0^\infty d\vec{r}\langle u^\gamma(0,0) u^\delta(\vec{r},t)\rangle. \tag{40}$$

For a periodic system, one can express the velocity flow field by a Fourier series

$$u^\gamma(\vec{r},t) = \sum_{\vec{k}} u_k^\gamma(t) e^{i\vec{k}\vec{r}}, \tag{41}$$

$$u_k^\gamma(t) = \frac{1}{N}\sum_i \frac{p_i^\gamma}{m_i} e^{-i\vec{k}\vec{r}_i}. \tag{42}$$

Under the plausible assumption that different Fourier components $u_k^\gamma(t)$ are uncorrelated, the diffusion tensor reads

$$\overleftrightarrow{D}(\vec{r}) = \sum_{\vec{k}} (1 - \hat{k}\hat{k}) e^{i\vec{k}\vec{r}} \int_0^\infty dt \left\langle u_k^{\gamma *}(0) u_k^\gamma(t)\right\rangle. \tag{43}$$

For the general case of a combined Hamiltonian and Brownian system Dünweg (cf. Eq. (22) of Ref. 39) has given a relation between the time integral of the correlation function of a property $\langle A(0)A(t)\rangle$ and its time derivative $\langle \dot{A}(0)\dot{A}(t)\rangle$. For a pure Hamiltonian system, one gets the simpler relation

$$\int_0^\infty dt \left\langle u_k^{\gamma *}(0) u_k^\gamma(t)\right\rangle = -\frac{\left\langle u_k^{\gamma *}(0) u_k^\gamma(0)\right\rangle^2}{\int_0^\infty dt \left\langle \dot{u}_k^{\gamma *}(0)\dot{u}_k^\gamma(t)\right\rangle}. \tag{44}$$

Thus, we are left with the computation of the time derivative of the velocity flow field

$$\dot{u}_k^\gamma = \frac{du_k^\gamma(t)}{dt} = \sum_i \left[\frac{\partial u_k^\gamma}{\partial \vec{r}_i}\cdot\frac{d\vec{r}_i}{dt} + \frac{\partial u_k^\gamma}{\partial \vec{p}_i}\cdot\frac{d\vec{p}_i}{dt}\right] \tag{45}$$

$$= \frac{1}{N}\sum_i \left[\left(-i\vec{k}\cdot\frac{\vec{p}_i}{m_i}\right)\frac{p_i^\gamma}{m_i} e^{-i\vec{k}\vec{r}_i} + \frac{F_i^\gamma}{m_i} e^{-i\vec{k}\vec{r}_i}\right], \tag{46}$$

where in the last step, we have used the expression Eq. (42) for the Fourier components of the velocity flow field and the projections $\vec{k}\cdot\vec{p}_i = k\cdot p_i^\delta$ and $\vec{k}\cdot\vec{r}_i = k\cdot r_i^\delta$. Retaining only terms linear in $\vec{k}$,

$$e^{-i\vec{k}\vec{r}_i} = 1 - i\vec{k}\vec{r}_i + \ldots, \tag{47}$$

$$-i\vec{k}e^{-i\vec{k}\vec{r}_i} = -i\vec{k} + \ldots, \tag{48}$$

and applying Newton's third law $\sum_i F_i = 0$, we finally get

$$\int_0^\infty dt \left\langle u_k^\gamma(0) u_k^\gamma(t)\right\rangle = \frac{k_B T}{V^2 \int_0^\infty dt \langle P_{\gamma\delta}(0)\cdot P_{\gamma\delta}(t)\rangle} \tag{49}$$

with the pressure tensor

$$P_{\gamma\delta} = \frac{1}{V}\sum_i \frac{1}{m_i} p_i^\gamma p_i^\delta + F_i^\gamma r_i^\delta. \tag{50}$$

At this point we come across the molecular Virial forming the basis for the calculation of the viscosity

$$\eta = \frac{V}{k_B T}\int_0^\infty dt \langle P_{\gamma\delta}(0)\cdot P_{\gamma\delta}(t)\rangle. \tag{51}$$

Assembling previous relations, the diffusion tensor turns out to be

$$\overleftrightarrow{D}(\vec{r}) = \frac{k_B T}{V\eta}\sum_{\vec{k}} \frac{1 - \hat{k}\hat{k}}{k^2} e^{i\vec{k}\vec{r}}, \tag{52}$$

This article is copyrighted as indicated in the article. Reuse of AIP content is subject to the terms at: http://scitation.aip.org/termsconditions. Downloaded to IP: 131.130.40.59 On: Tue, 13 May 2014 13:30:09

which is the correct form for a periodic system. Its real space analog, appearing as a multiple of the Oseen tensor,

$$\overleftrightarrow{D}(\vec{r}) = \frac{k_B T}{8\pi\eta r}(1 + \hat{r}\hat{r}) \tag{53}$$

refers to a truly infinite system. Besides this important difference, we want to emphasise that the merit of the derivation above is the formulation of the viscosity in molecular terms, i.e., via the time correlation function of the Virial, thus preserving the link to the molecular world.

Our primary goal, the self-diffusion coefficient, can be easily obtained from the diffusion tensor by taking the trace

$$D(r) = \frac{1}{3}\mathrm{tr}\overleftrightarrow{D} \tag{54}$$

$$= \frac{k_B T}{6\pi\eta}\frac{1}{V}\sum_{\vec{k}}\frac{4\pi}{k^2}e^{i\vec{k}\vec{r}}. \tag{55}$$

In the second relation, we recognise the Ewald potential

$$\phi_{EW}(\vec{r}) = \frac{1}{V}\sum_{\vec{k}}\frac{4\pi}{k^2}e^{i\vec{k}\vec{r}}, \tag{56}$$

describing Coulomb interactions in periodic systems, instead of the bare Coulomb potential $1/r$ acting in an infinite system

$$D(r) = \frac{k_B T}{6\pi\eta r}. \tag{57}$$

Since summation in k-space is ill-defined, one usually introduces the convergence factor $e^{-k^2/4\alpha^2}$,

$$\phi^k_{EW}(\vec{r}) = \frac{1}{V}\sum_{\vec{k}}\frac{4\pi}{k^2}e^{-k^2/4\alpha^2}e^{i\vec{k}\vec{r}}. \tag{58}$$

As a consequence, one needs a complementary sum in real space

$$\phi^r_{EW}(\vec{r}) = \sum_{\vec{n}}\frac{\mathrm{erfc}(\alpha|\vec{r}+\vec{n}L|)}{|\vec{r}+\vec{n}L|} \tag{59}$$

in order to make total Ewald potential independent of the parameter α. In simulation studies the principal finiteness of a computational device prohibits the application of the Coulomb potential $\frac{1}{r}$ and one has to use alternative methods. Among the diversity of all methods to mimic Coulomb interactions in a finite system, the Ewald method has been shown to have minimum size dependence. Nevertheless, there is a size dependence. In other words, the diffusion coefficient D_{PBC} simulated for a system with PBC differs from that of the infinite system D_0,

$$D_{\mathrm{PBC}} = D_0 + (D_{\mathrm{PBC}} - D_0). \tag{60}$$

In order to assess the amount of deviation to the infinite system, i.e., the term in brackets, we replace it by the respective hydrodynamic expressions derived above (Eq. (55)), thereby including the Ewald potential as a representative of the actual simulation

$$D_{ii} = \lim_{\vec{r}\to 0} D(r) = D_0 + \frac{k_B T}{6\pi\eta}\lim_{\vec{r}\to 0}\left[\phi_{EW}(\vec{r}) - \frac{1}{r}\right] = \frac{k_B T}{6\pi\eta}\frac{1}{L}\xi. \tag{61}$$

The term in brackets is the so-called Wigner potential. For a cubic lattice its limit is given by ξ/L with $\xi = 2.8372\ldots$.[21]

At this point, we were able to concretise the Taylor series of the self-diffusion coefficient by the use of hydrodynamics. We showed that one can correct size dependence caused by the Ewald summation, as long as the box size suffices to reach the linear regime. For smaller systems the correction cannot be rightfully applied. Borodin[20] was the first one to apply a correction for self-diffusion coefficients of ionic liquids, but he simulated only systems up to 216 ion pairs, which is not enough to reach the linear regime. Therefore, there is some uncertainty of the extent of his correction. He reported a finite size correction in the order of 10%–20% for ionic liquids and simulated electrolytes in general. However, the correction we could extract from the linear regime of our data amounts to about 15% as well.

Viscosity is a big issue when it comes to ionic liquids. They can be fluid as oil as well as sticky, as needed for lubricants. Therefore, it is of great interest to be able to determine viscosities out of simulation data. In general there are two different simulation methods to calculate viscosities, simulation in equilibrium and simulations following the linear response theory (nonequilibrium). The Green-Kubo approach, defined in Eq. (51), and the Einstein-Helfand method represent calculation methods via equilibrium dynamics. But these methods have their drawbacks. Due to the high viscosity of ILs, it is often cumbersome to determine accurate viscosities. In the publications of Hu and Margulis,[18,19] they dealt with the problem of calculating viscosities and proposed the periodic perturbation method (nonequilibrium) as their method of choice. Müller-Plathe and co-workers[40] calculated the viscosity of $\mathrm{BMIM^+PF_6^-}$ by means of the Einstein-Helfand method and reverse nonequilibrium molecular dynamics. The results were in good agreement. Anyway, the size dependence offers an alternative route to viscosity, by reforming Eq. (61) to

$$\eta = \frac{k_B T\xi}{6\pi}\frac{1}{(D_0 - D_{PBC})L}. \tag{62}$$

Using the slope and the intercept of the linear regime, we derived the according values for each system size, which can be seen in Table I. It is apparent that the viscosities for the four largest systems are in good agreement. The smaller systems deviate from this values, even producing negative viscosities. It is of uttermost importance to ascertain correct self-diffusion coefficients in the linear regime, because even the smallest deviation results in different viscosities. We want to emphasise that the diffusion coefficient suffers from size dependence and not the viscosity. The fact that a linear regime evolves over a major interval implies that η cannot be size dependent. This was already shown by Yeh and Hummer[22] for a low-viscous water system.

VII. TIME DEPENDENCE

The totally elapsed time for a 100 ps run of a system consisting of 500 ion pairs adds up to 1 hour with the chosen setup. In order to get an impression of the computational effort for all the other systems (N = 8–2000), please refer to Fig. 9. The most surprising feature is the observation of a

This article is copyrighted as indicated in the article. Reuse of AIP content is subject to the terms at: http://scitation.aip.org/termsconditions. Downloaded to IP: 131.130.40.59 On: Tue, 13 May 2014 13:30:09

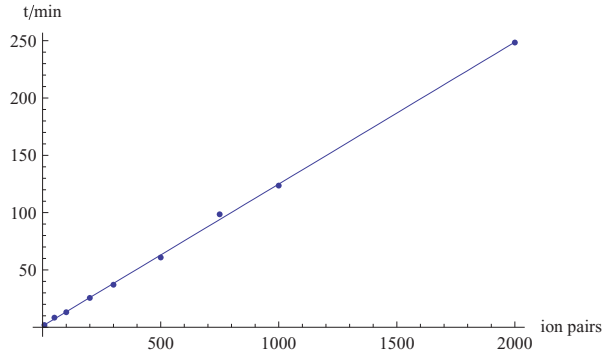

FIG. 9. The required computation time for a 100 ps run is given for each system.

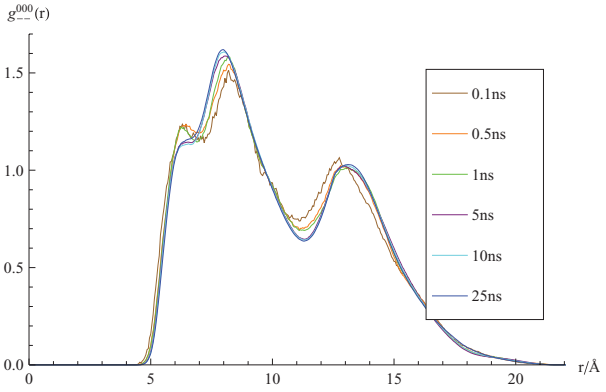

FIG. 10. Time evolution of the anion-anion RDF of 50 ion pairs. The initial first peak degenerates to a shoulder after 5 ns of simulation length.

fairly linear scaling, since one would expect a behaviour according to the "$N \log N$"-rule, following from the application of the particle-mesh-Ewald method.

Before starting a simulation, an appropriate start configuration, which represents a proper sample from phase space, is required. Therefore, several strategies are pursued. It is very common to place molecules at lattice points with the result that a crystal is formed. This crystal structure has to be melted mostly by the use of simulated annealing. This is a cumbersome and time consuming process. In our case we followed a different approach, as already mentioned in Sec. II. We used the program PACKMOL[33] to pack molecules into boxes of defined size. Thereby, molecules are packed according to their geometric properties, which results in a homogeneous distribution of the given species in the box, but at the same time with extremely high energies. These energies do not pose a permanent problem, since they can be minimised by the use of any minimisation method such as steepest descent. Afterwards the start configuration is ready for simulation.

Having obtained an initial configuration by one way or another, one can go for the actual simulation. It is of utmost importance that the simulated system is in equilibrium. Therefore, one usually discards some initial part of the trajectory as the so-called equilibration period. Since its length is more or less an educated guess, we have followed an alternative route: We analyzed the complete trajectory and compared the results to an analogous analysis, where 1–3 ns of data were discarded from the beginning of the same trajectory. We could not detect any significant differences in the results, hence we did not discard any data for the sake of equilibration. Furthermore, one could argue that 1–3 ns are not enough to disconnect the trajectories from each other. In case of obvious pecularities or artefacts, our experience was that 5–10 ns of the trajectory have to be discarded to get rid of it.

A. The influence of finite time

This section is dedicated to the influence of finite time on various system sizes. We will start once again with the description of structure and then we will move on to dynamical properties.

Figure 10 shows the evolution of the anion-anion pair correlation function of 50 ion pairs with increasing trajectory length. One clearly sees that for such small systems it takes up to 5 ns until the first peak degenerates to a shoulder. For larger systems the situation is less critical as the higher number of ion pairs considerably improves statistics.

In order to gain an insight into statistical deviations of dynamics resulting from different simulation lengths, we have selected the cationic diffusion coefficient D^+, the averaged relaxation time $\langle\tau^+_{SP}\rangle$ derived from the KWW-fit of the single particle dipolar correlation function $\langle\mu^+(0)\mu^+(t)\rangle$, the static conductivity $\sigma(0)$, and the collective analog $\langle\tau^+_{M_D}\rangle$ to $\langle\tau^+_{SP}\rangle$. For varying simulation length, we have computed the respective values. In Fig. 11 we plotted the absolute values as a function of the simulation length t. For the sake of simplicity in the figure we selected three systems $N = 50$, $N = 500$, and $N = 2000$ for the following reasons: $N = 50$ is the smallest system, which gets the structure right. $N = 500$ marks the onset of the linear regime. $N = 2000$ is the largest system studied. The position of the lines can be assigned to size dependence and the shape to finite time. In the upper half and to the right of Fig. 11 the diffusion coefficient of the cations is displayed. A striking feature is that 30 ns are needed to get a fairly constant value for $N = 500$ (orange) and $N = 2000$ (black). For 50 ion pairs (blue) the diffusion coefficient does not reach a limiting value. For average single particle rotation $\langle\tau^+_{SP}\rangle$, in the upper half to the left, we have a similar behaviour, except for the fact that 20 ns suffice. The lower half of Fig. 11 is dedicated to collective properties. Due to statistics of collective properties the values vary more than those of single particle properties. To the left, the static conductivity $\sigma(0)$ is shown and once again the line, which belongs to $N = 50$, has a wider spread than those of the larger systems. The same can be said of $\langle\tau^+_{M_D}\rangle$, which can be seen to the right. Altogether, the mobility of ions is enhanced in larger systems.

Although Fig. 11 shows the convergence of various properties as a function of simulation time, it also tells us that the effects of finite time are subordinated to that of finite size. This hierarchy of size and time dependence has practical consequences. Computational resources should be invested into

This article is copyrighted as indicated in the article. Reuse of AIP content is subject to the terms at: http://scitation.aip.org/termsconditions. Downloaded to IP: 131.130.40.59 On: Tue, 13 May 2014 13:30:09

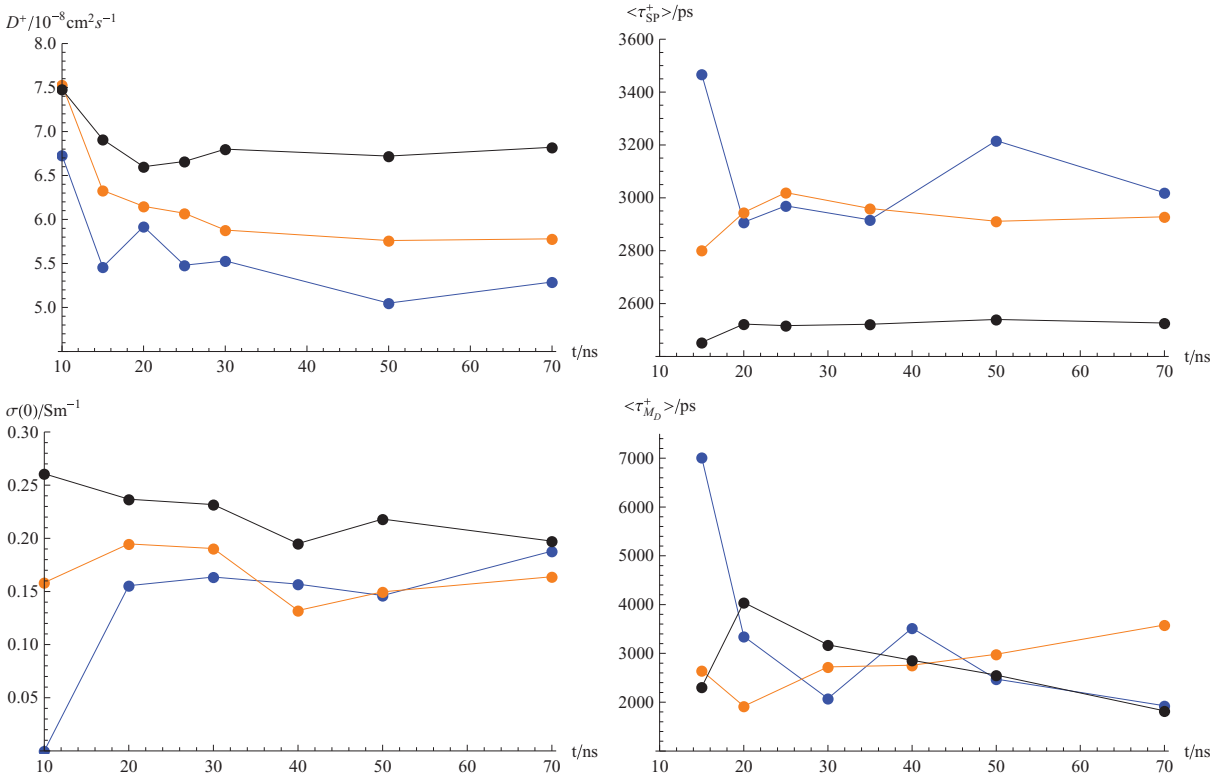

FIG. 11. The influence of finite time on the diffusion coefficient of the cations is shown in the upper part to the left. The average single particle relaxation time can be found to the left. The lower part is dedicated to collective properties, the static conductivity $\sigma(0)$ to the left, and the average relaxation time to the right. Systems with 50, 500, and 2000 ion pairs are depicted in blue, orange, and black, respectively.

larger systems rather than into longer simulations. The respective guideline is the achievement of the linear regime.

VIII. CONCLUSION

Simulation of Coulomb forces always faces the finiteness of computational resources. Therefore, they have a principal size dependence and one has to apply methods which minimise this dependence. In molecular ionic liquids, where each molecule carries a net charge, N-dependence is a central issue, even when using the method with minimum size dependence, the Ewald method.

Preliminary but incomplete studies of finite size effects in molecular ionic liquids can be found throughout literature.[12–20] Our work, based on the concrete system $\mathrm{EMIM}^+\mathrm{CF_3SO_3^-}$, tries to perform a systematic study of the influence of finite size on the structure, single particle, and collective dynamics.

Structure, investigated on the basis of RDFs and their generalisation to include molecular orientation, needs a minimum number of 50 ion pairs in order to free the initial region from artifacts. Collective structural properties, such as the Kirkwood G-factor, demand even larger systems. The emerging linear dependence of systems with 500 ion pairs and more could be seen while plotting against the inverse box length L.

As a next step, we investigated single particle and collective rotation by means of the average relaxation time, derived from KWW-fits. Again linear relationships appeared for systems with $N \geq 500$. In order to characterise translational motion, we computed the diffusion coefficient D from the linear slope of the MSD. The diffusion coefficients showed again a linear dependence. The collective analog to the MSD the dipolar displacement $\langle \Delta \vec{M}_j^2(t) \rangle$ gives the static conductivity $\sigma(0)$ following again a linear relationship. As the slopes of MSD and $\langle \Delta \vec{M}_j^2(t) \rangle$ differ considerably it is not possible to compute $\sigma(0)$ out of single particle data.

In describing the size dependence of various properties, the inverse box length $x = 1/L$ turned out to be the central variable. For a diversity of structural and dynamical properties a linear dependence on x was found for systems with at least 500 ion pairs. Formally, this may be considered as a truncated Taylor series. Therefore, the infinite system value can be derived from an appropriate linear fit.

In case of translational diffusion coefficients hydrodynamics yields an explicit expression for the linear factor involving the temperature, the viscosity, and ξ/L. This decisive, last term is a compact measure of the difference between the Ewald potential acting in a finite, computational sample and the bare Coulomb potential of a truly infinite system. As this result is of hydrodynamic origin, it can only be used in a correct manner for sufficiently large systems. For the non-polarisable system $\mathrm{EMIM}^+\mathrm{CF_3SO_3^-}$ we have found that 500 ion pairs are at least necessary to enter this linear regime. However, we found evidence that the onset of the linear regime is essentially affected by viscosity. This view is supported by the comparison of our results to that of Yeh and

This article is copyrighted as indicated in the article. Reuse of AIP content is subject to the terms at: http://scitation.aip.org/termsconditions. Downloaded to IP: 131.130.40.59 On: Tue, 13 May 2014 13:30:09

Hummer[22] on water. The difference of viscosity of both systems goes along with a different onset of the linear regime.

Furthermore, the concept of the linear hydrodynamic regime of the diffusion coefficient can be used as an alternative route to viscosity. However, this technique requires extremely accurate diffusion coefficients, which raises the question of time dependence too. Nevertheless, there is a clear hierarchy of size and time dependence: If a system is too small and not part of the linear regime, its size dependence cannot be compensated by a longer simulation. Once in the linear regime, it is better to simulate a larger system for a shorter time than vice versa. Since we have found that execution time scales linearly with system size, the effort to simulate a system of double size is equivalent to a simulation of half length.

ACKNOWLEDGMENTS

The computational work was performed on the Vienna Scientific Cluster [http://www.zid.tuwien.ac.at/vsc] of the University of Vienna, the Vienna University of Technology, and the University of Natural Resources and Applied Life Science Vienna. We would also like to thank them for the generous allocation of computer time. This work was supported by Project No. P19807 of the FWF Austrian Science Fund.

[1]L. Boltzmann, *Vorlesung Über Gastheorie* (J. A. Barth, Leipzig, 1896/1898).
[2]C. Jarzynski, Phys. Rev. Lett. **78**, 2690 (1997).
[3]B. J. Alder and T. W. Wainwright, J. Chem. Phys. **27**, 1208 (1957).
[4]A. Rahman, Phys. Rev. **136**, A405 (1964).
[5]L. Verlet, Phys. Rev. **159**, 98 (1967).
[6]A. Rahman and F. H. Stillinger, J. Chem. Phys. **55**, 3336 (1971).
[7]C. G. Hanke, S. L. Price, and R. M. Lynden-Bell, Mol. Phys. **99**, 801 (2001).
[8]E. J. Maginn, J. Phys.: Condens. Matter **21**, 373101 (2009).
[9]C. Rey-Castro and L. F. Vega, J. Phys. Chem. B **110**, 14426 (2006).
[10]J. Pićalek and J. Kolafa, J. Mol. Liq. **134**, 29 (2007).
[11]D. Roy, N. Patel, S. Conte, and M. Maroncelli, J. Phys. Chem. B **114**, 8410 (2010).
[12]J. N. A. C. Lopes and A. A. H. Pádua, J. Phys. Chem. B **110**, 3330 (2006).
[13]J. N. A. C. Lopes and A. A. H. Pádua, J. Phys. Chem. B **110**, 7485 (2006).
[14]Y. Wang and G. A. Voth, J. Am. Chem. Soc. **127**, 12192 (2005).
[15]Y. Wang and G. A. Voth, J. Phys. Chem. B **110**, 18601 (2006).
[16]Y. Wang, W. Jiang, and G. A. Voth, *Ionic Liquids IV*, ACS Symposium Series Vol. 975 (American Chemical Society Publishers, Washington, D.C., 2007), pp. 272.
[17]A. Bagno, F. D'Amico, and G. Saielli, J. Mol. Liq. **131–132**, 17 (2007).
[18]Z. Hu and C. J. Margulis, J. Phys. Chem. B **111**, 4705 (2007).
[19]Z. Hu and C. J. Margulis, Acc. Chem. Res. **47**, 1097 (2007).
[20]O. Borodin, J. Phys. Chem. B **113**, 11463 (2009).
[21]B. Dünweg and K. Kremer, J. Chem. Phys. **99**, 6983 (1993).
[22]I.-C. Yeh and G. Hummer, J. Phys. Chem. B **108**, 15873 (2004).
[23]A. D. MacKerell, Jr., B. Brooks, C. L. Brooks, L. Nilson, B. Roux, Y. Won, and M. Karplus, *The Encyclopedia of Computational Chemistry*, edited by P. V. R. Schleyer (Wiley, New York, 1998), Vol. 1, p. 271.
[24]B. R. Brooks, R. E. Bruccoleri, B. D. Olafson, D. J. States, and S. Swaminathan, J. Comput. Chem. **4**, 187 (1983).
[25]T. Darden, D. York, and L. Pedersen, J. Chem. Phys. **98**, 10089 (1993).
[26]U. Essmann, L. Perera, M. L. Berkowitz, T. Darden, H. Lee, and L. G. Pedersen, J. Chem. Phys. **103**, 8577 (1995).
[27]J.-P. Ryckaert, G. Ciccotti, and H. J. C. Berendsen, J. Comput. Phys. **23**, 327 (1977).
[28]M. G. Del Pópolo and G. A. Voth, J. Phys. Chem. B **108**, 1744 (2004).
[29]J. N. Canongia Lopes, J. Deschamps, and A. A. H. Pádua, J. Phys. Chem. B **108**, 2038 (2004).
[30]J. N. Canongia Lopes and A. A. H. Pádua, J. Phys. Chem. B **108**, 16893 (2004).
[31]I. J. Chen, D. Yin, and A. D. MacKerell, J. Comput. Chem. **23**, 199 (2002).
[32]A. D. MacKerell, Jr., D. Bashford, M. Bellott, R. L. Dunbrack, J. D. Evanseck, M. J. Field, S. Fischer, J. Gao, H. Guo, S. Ha, D. Joseph-McCarthy, L. Kuchnir, K. Kuczera, F. T. K. Lau, C. Mattos, S. Michnick, T. Ngo, D. T. Nguyen, B. Prodhom, W. E. Reiher, B. Roux, M. Schlenkrich, J. C. Smith, R. Stote, J. Straub, M. Watanabe, J. Wiorkiewicz-Kuczera, D. Yin, and M. Karplus, J. Phys. Chem. B **102**, 3586 (1998).
[33]L. Martínez, R. Andrade, G. Birgin, and J. M. Martínez, J. Comput. Chem. **30**, 2157 (2009).
[34]Y.-F. Hu and C.-M. Xu, "Effect of the structures of ionic liquids on their physical-chemical properties and the phase behaviour of mixtures involving ionic liquids," Chem. Rev. (unpublished).
[35]J. G. Kirkwood, J. Chem. Phys. **7**, 911 (1939).
[36]T. Keyes and D. Kivelson, J. Chem. Phys. **56**, 1057 (1972).
[37]D. Kivelson and P. Madden, Mol. Phys. **30**, 1749 (1975).
[38]B. J. Alder and W. E. Alley, Phys. Today **37**, 56 (1984).
[39]B. Dünweg, J. Chem. Phys. **99**, 6977 (1993).
[40]W. Zhao, F. Leroy, S. Balasubramanian, and F. Müller-Plathe, J. Phys. Chem. B **112**, 8129 (2008).

This article is copyrighted as indicated in the article. Reuse of AIP content is subject to the terms at: http://scitation.aip.org/termsconditions. Downloaded to IP: 131.130.40.59 On: Tue, 13 May 2014 13:30:09

4 From Short-Range to Long-Range Intermolecular NOEs in Ionic Liquids: Frequency Does Matter

Angewandte Chemie International Edition **52**, 9242 (2013); DOI: 10.1002/anie.201302712.
Copyright 2013, Wiley-VCH Verlag GmbH & Co.

Ionic Liquids

DOI: 10.1002/anie.201302712

From Short-Range to Long-Range Intermolecular NOEs in Ionic Liquids: Frequency Does Matter**

*Sonja Gabl, Othmar Steinhauser, and Hermann Weingärtner**

The nuclear Overhauser effect (NOE) is widely used for studying local structures in liquids and solutions.[1] The NOE reflects cross-relaxation between two nuclear spins, I and S, because of magnetization transfer through coupling of their magnetic dipole moments. With increasing internuclear distance r the cross-relaxation rate σ_{IS} decays as $1/r^6$. Thus, a NOE is only achieved, if r is less than 4–5 Å.[2]

While derived for spins in the same molecule, a rule like this is also applied to intermolecular cross-relaxation, implying that the NOE essentially captures molecules in the innermost coordination sphere of the relaxing particle. To generate a notable probability for magnetization transfer the life time of these configurations has to be at least of the order of the inverse Larmor frequency $1/\omega_I$ of the relaxing spin I.[2] In ^{1}H NMR spectroscopy this time is typically of the order of 0.5 ns. The specificity of NOE spectroscopy to local interactions prospects intriguing applications. In the present work we focus on NOE studies of local ion configurations in ionic liquids (ILs),[3] but our results are prototypical for many other classes of liquids as well.

As a representative example, we consider results on the ^{1}H-^{19}F NOE in 1-butyl-3-methylimidazolium tetrafluoroborate (**1**) by Giernoth's research group,[3a] which appear to indicate the existence of cation–anion pairs with life times on the nanosecond time scale. After a long-standing debate about the definition, existence (or not), and life time of ion pairs in neat ILs,[4] there is now consensus that in **1** (see Scheme 1) and similar ILs long-lived pairs do not exist. Otherwise, ILs would, for example, reveal a distinct ion pair mode in the dielectric relaxation spectrum, which for **1**[5] and similar ILs has never been observed in experiments and simulations.[6]

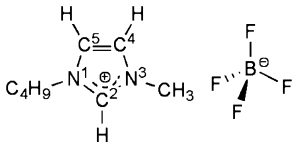

Scheme 1. 1-Butyl-3-methylimidazolium tetrafluoroborate (**1**).

[*] Prof. Dr. H. Weingärtner
Department of Physical Chemistry II
Ruhr-University of Bochum, 44780 Bochum (Germany)
E-mail: hermann.weingaertner@rub.de
Mag. S. Gabl, Prof. Dr. O. Steinhauser
Department of Computational Biological Chemistry
University of Vienna, 1090 Vienna (Austria)

[**] This work is supported by the Cluster of Excellence RESOLV (EXC 1069) funded by the Deutsche Forschungsgemeinschaft. NOE = nuclear Overhauser effect.

The situation closely resembles that encountered in studies of protein hydration, where protein–water NOEs mimic a strongly retarded dynamics of hydration water relative to the bulk liquid. As shown by Halle's research group this strongly bound water does not withstand the test of other experiments.[7] A properly formulated theory of the intermolecular NOE in protein–water solutions by Halle[8] predicts a protein–water NOE dominated by long-range dipolar couplings to bulk water rather hydration water.

Taken together, these observations give rise to fundamental questions about the mechanisms governing the intermolecular NOE.

The present paper addresses these issues by exploring the consequences of a new theory of the intermolecular NOE[9] for the interpretation of NOE data in liquids in general and ILs in particular. The results for **1**[3a] are particularly suited for such an analysis because the literature offers auxiliary data for modeling the NOE.

The information provided by the cross-relaxation rate σ_{IS} concerns the spectral density function $J(\omega)$, which describes the modulation of the magnetic dipole–dipole interaction between the spins I and S by molecular motions. For ^{1}H-^{19}F heteronuclear NOE spectroscopy in the laboratory (Zeeman) frame σ_{IS} is given by Equation (1),[2]

$$\sigma_{IS} = 0.6J(\omega_I + \omega_S) - 0.1J(\omega_I - \omega_S) \quad (1)$$

where ω_I and ω_S are the Larmor frequencies of the spins I and S. σ_{IS} involves the response at two frequencies, namely the sum frequency $(\omega_I + \omega_S)$ and the difference frequency $(\omega_I - \omega_S)$. The understanding of the NOE is founded in a different behavior of these two terms.

While the frequency dependence of $J(\omega)$ prospects detailed information on the intermolecular structure and dynamics,[10] NOE data are usually acquired at a single frequency. This loss of information makes their interpretation highly model-dependent. Most NOE studies resort to a short-range spectral density function of the form given in Equation (2),[2]

$$J(\omega) = K_{IS}\frac{1}{r^6}\frac{\tau_c}{1+(\omega\tau_c)^2} \quad (2)$$

which can be theoretically derived under the assumption that during magnetization transfer the internuclear vector $\mathbf{r}$ connecting I and S has a fixed length r (bold quantities denote vectors), as is the case for an intramolecular NOE.[2] τ_c is the tumbling time of the vector $\mathbf{r}$, $K_{IS} = [(\mu_0/4\pi)\hbar\gamma_I\gamma_S]^2$ is the dipolar coupling constant, where γ_I and γ_S are the magnetogyric ratios of the spins, and μ_0 is the permeability of the vacuum. For ^{1}H-^{19}F spin pairs K_{IS} is 5.04×10^{11} Å^{6}s^{-2}.

© 2013 Wiley-VCH Verlag GmbH & Co. KGaA, Weinheim

For the intermolecular cross-relaxation NOE this approach neglects the modulation of the vector **r** by translational diffusion of the particles. It is known for a long time from theories of intermolecular spin–lattice relaxation that translational dynamics renders $J(\omega)$ long-range.[11] Here, we reconsider these issues for a spin I in a cation, interacting with N_S spins S in anions. The complete theory and its relation to earlier approaches will be given elsewhere.[9]

Figure 1 illustrates our model for the intermolecular dynamics. The cation–anion distribution is described by the radial pair distribution function $g(R)$, where the vector **R** connects the centers of mass of the ions. The two spins are

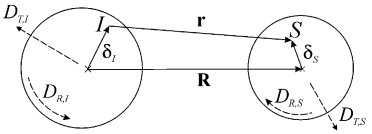

Figure 1. Model for the dynamics governing intermolecular cross-relaxation between the spins *I* and *S*.

located at distances δ_I and δ_S from the centers of mass of the ions. The magnetic dipole–dipole interaction between I and S is modulated by translational and rotational motions of the ions. Translational motions modulate the vector **R**, while rotational motions modulate the orientations of the off-center vectors $\boldsymbol{\delta}_I$ and $\boldsymbol{\delta}_S$. Translational diffusion of the ions is described by the relative diffusion coefficient D_T, which is approximated by the sum of the self-diffusion coefficients of the ions, $D_T \cong D_{T,I} + D_{T,S}$. Rotational motions are characterized by the rotational diffusion coefficients $D_{R,I}$ and $D_{R,S}$ of the ions, which are related to the measurable orientational correlation times τ_c by the relation $D_R = (6\tau_c)^{-1}$. The translational and rotational diffusion coefficients are assumed to be spatially uniform.

The time evolution of the magnetic dipole–dipole interaction is obtained by solving the differential equations for rotational and translational diffusion under the boundary conditions given by our model, which leads to a representation of $J(\omega)$ in the reciprocal space with the wave vector **k** instead of **R** as a variable. When approximating $g(R)$ by a uniform distribution of the ions, modeled by a step function ranging from a lower cut-off distance d to infinity, our theory provides an analytical expression for $J(\omega)$. The latter approximation, known as "force-free model",[11c] underlies all theories of intermolecular spin relaxation of interest here. The resulting expression for the spectral density function $J(\omega)$ reads [Eq. (3)],

$$J(\omega) = \rho_S K_{IS} \sum_{l=0}^{\infty} \int_0^{\infty} Q_l(k,\omega) \frac{j_{l+1}(kb)}{b^{l+1}} \left[\frac{j_{l+1}(kb)}{d^{l+1}} - \frac{j_{l+1}(kR)}{R^{l+1}} \right] dk \qquad (3)$$

where ρ_S is the spin density of S. The functions $j_l(x)$ are the spherical Bessel functions of rank l. b is the closest distance of approach between the ions. A molecular dynamics (MD) simulation of $g(R)$[12] yields $b = 3.05$ Å. The distance d defines the onset of the step function. In a self-consistent treatment the choice of $d = 5.28$ Å has to reproduce the spin density of $\rho_S = 1.24 \times 10^4$ Å^{-3} of ^{19}F. The dynamical behavior is captured by the rotational–translational coupling function $Q_l(k,\omega)$ given in Equation (4):

$$Q_l(k,\omega) = C_l \sum_{\lambda=0}^{l} \frac{\delta_I^{2\lambda}}{(2\lambda+1)!} \frac{\delta_S^{2\nu}}{(2\nu+1)!} f_l(k,\omega) \qquad (4)$$

with the abbreviations $C_l = (l+1)\ (l+2)\ (2l+3)\ (2l+1)!/6$ and $\nu = 1-\lambda$. The function [Eq. (5)]

$$f_l(k,\omega) = \frac{k^2 D_T + \lambda(\lambda-1) D_{R,I} + \nu(\nu+1) D_{R,S}}{\left[k^2 D_T + \lambda(\lambda-1) D_{R,I} + \nu(\nu+1) D_{R,S}\right]^2 + \omega^2} \qquad (5)$$

represents a combination of the measurable translational and rotational diffusion coefficients. We note that the translational diffusion coefficient is weighted by the square of the wave vector, while the rotational diffusion coefficients are not. For purely translational dynamics only terms with $l = 0$ survive. This limit is achieved, if the spins I and S coincide with the centers of mass of the ions ($\delta_I = \delta_S = 0$). In our calculations convergence was achieved by summing terms up to $l = 6$ to 10.

Based on these equations we have analyzed the ^{1}H-^{19}F heteronuclear NOE of **1** based on three models:

- Model A corresponds to the intermolecular NOE between the proton at carbon C^2 of the imidazolium cation ($\delta_I =$ 1.8 Å) and ^{19}F of the $[BF_4]^-$ anion ($\delta_S = 1.4$ Å).
- Model B considers the NOE between a proton of maximum eccentricity ($\delta_I = 2.8$ Å) in the cation and ^{19}F ($\delta_S =$ 1.4 Å). This choice, albeit exaggerated with regard to the real IL, helps to assess the dependence of the NOE on the spin eccentricity.
- Model C refers to the limiting case of a purely translational mechanism ($\delta_I = \delta_S = 0$).

Table 1 lists the experimental data used in our calculations.[13] While the rotational dynamics of the anions and cations occurs on time scales of 100 and 500 ps, respectively,

Table 1: Dynamical properties used for modeling the spectral density function $J(\omega)$ at 25 °C.[13]

Property	Cation	Anion
D_T [m^2 s^{-1}]	1.40×10^{-11}	1.33×10^{-11}
D_R [s^{-1}]	3.19×10^8	1.41×10^9
τ_c [ps]	522	118

translational motions show a broadly distributed dynamics in the nanosecond regime. The rationale is that a distant pair of spins needs a longer time to randomize the internuclear vector **r** than a pair of neighboring spins. According to the Einstein equation the time τ_{trans} for modulation of the center-to-center vector **R** increases with the mean-square displacement $\langle \mathbf{R}^2 \rangle$ as $\tau_{trans} = \langle \mathbf{R}^2 \rangle / 6 D_T$. With $\langle \mathbf{R}^2 \rangle^{1/2} = 6$ Å, which is a typical distance for the exchange of an anion from the first to the second coordination shell of the cation in **1**, we find $\tau_{trans} = 2.3$ ns.

 © 2013 Wiley-VCH Verlag GmbH & Co. KGaA, Weinheim

In simple solvents of low viscosity like aqueous solutions the molecular motions modulating the NOE are of the order of several picoseconds. As a consequence the spectrometer frequencies are substantially below the frequencies of the molecular motions determining the spectral density $J(\omega)$. Then, one approaches the so-called "extreme-narrowing" limit, where $J(0) \cong J(\omega_I - \omega_S) \cong J(\omega_I + \omega_S)$. As a consequence σ_{IS} becomes independent of frequency, and Equation (1) simplifies to $\sigma_{IS} = 0.5\,J(0)$.[2] Much of the literature on the NOE refers to this situation. It is therefore apt to start our analysis by modeling cross-relaxation in this limiting case.

Figure 2 shows the calculated spectral density $J^*(0)$ in the extreme narrowing limit as a function of the center-to-center distance R for the models A to C, supplemented by a sketch of

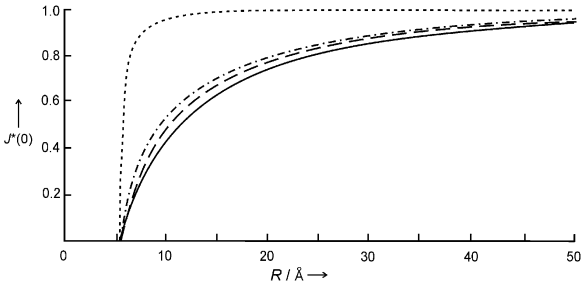

Figure 2. Spectral density function $J^*(0)$ in the extreme-narrowing limit as a function of the center-to-center distance R of the ions for model A (dashed curve), model B (dashed-dotted curve), and model C (solid curve). All curves are normalized to their asymptotic values at large R. The dotted line sketches the R^{-6} dependence as a limiting case.

the short-range R^{-6} dependence. The asterisk of $J^*(0)$ indicates that all curves are normalized by their asymptotic values, which increase with increasing off-center location of the spins. While the R^{-6}-dependent NOE immediately rises to its maximum value (dotted curve), the intermolecular NOEs are long-range. In the translational limit (solid curve) a fit to a distance dependence of the form R^{-n} yields $n = 1.1$, which practically implies a $1/R$-dependence, as is also predicted by some early theories of intermolecular spin relaxation of monoatomic liquids.[11] With increasing spin eccentricity, where rotational motions become relevant, the R dependence of the NOE changes only marginally. We find $n = 1.17$ for model A and $n = 1.27$ for model B, which represents the maximum off-center effect. Thus, in both cases the decay of the spectral density function is still governed by translational dynamics.

Furo's research group has, however, demonstrated[10] that in systems dominated by a broadly distributed translational dynamics this limit is not reached at the typical spectrometer frequencies, even for small molecules in systems of low viscosity. This is even more so, for ILs, the viscosities of which typically exceed those of fluid organic solvents by at least two orders of magnitude (at 25 °C the viscosity of **1** is $\eta =$ 104.9 mPa s[13]). In the latter case the spectral density is shifted downward and "meets" the spectrometer frequency. To elucidate the resulting interplay of the molecular frequencies and the spectrometer frequency, Figure 3 shows the

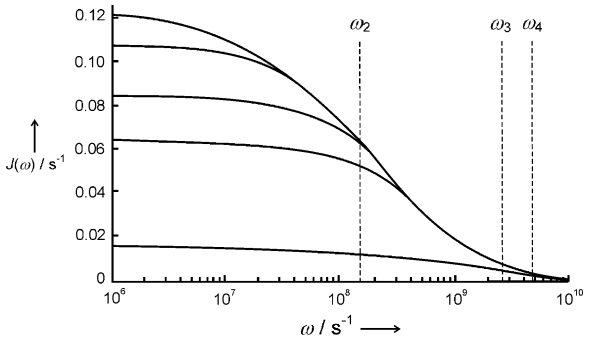

Figure 3. Spectral density function $J(\omega)$ as a function of frequency for model A for selected values of the spatial range, from top to bottom referring to $R = 100$, 30, 15, 10, and 6 Å, respectively. The three vertical bars mark the selected spectrometer frequency, $\omega_3 = 2.51$ GHz ($\nu_3 = 400$ MHz), the corresponding difference frequency $\omega_2 = (\omega_I - \omega_S) = 0.15$ GHz, and the sum frequency $\omega_4 = (\omega_I + \omega_S) = 4.85$ GHz. The ordinate is placed at $\omega_1 = 1$ MHz, where the extreme-narrowing regime is reached.

complete frequency spectrum $J(\omega)$ for model A for selected values of the spatial range R ranging from 6 to 100 Å. Although widely spread at zero-frequency, the bundle of curves in Figure 3 approaches each other with increasing frequency and the curves finally converge in the asymptotic regime.

It is instructive to consider in more detail results for the spatial dependence of the NOE at four frequencies of particular interest, numbered from low to high frequencies as ω_1 to ω_4. Our calculations are based on a spectrometer frequency of $\omega_3 = 2.51$ GHz ($\nu = 400$ MHz) used in the experiments for **1**. $\omega_1 = 1$ MHz is representative for the onset of the extreme-narrowing regime. Strikingly, ω_1 is by more than two orders of magnitude below the spectrometer frequencies used in NOE experiments. In other words, in practice the extreme-narrowing limit will never apply for ILs. $\omega_2 = (\omega_I - \omega_S) = 0.15$ GHz and $\omega_4 = (\omega_I + \omega_S) = 4.85$ GHz are the corresponding difference and sum frequencies entering into the expression for the cross-relaxation rate given by Equation (1). In Figure 3 the frequencies ω_2 to ω_4 are marked by vertical bars and the ordinate axis is placed at $\omega_1 = 1$ MHz. The resulting curves for the spatial dependence of the NOE were tentatively fitted to an R^{-n} dependence.

Figure 4 displays the exponents of the R dependence of the NOE at different frequencies. The results reveal a steady transition from long-range behavior of the NOE at low frequencies ($n = 1.17$ at $\omega_1 = 1$ MHz and $n = 2.5$ at $\omega_2 = (\omega_I - \omega_S) = 0.15$ GHz to short-range behavior at high frequencies ($n = 7.2$ at $\omega_3 = 2.5$ GHz and $n = 8.2$ at $\omega_4 = (\omega_I + \omega_S) =$ 4.85 GHz). Within the limits of the model the latter values are consistent with an R^{-6} dependence of the NOE.

The reason for this transition can be found in the rotational–translational coupling function [Eq. (5)]. For higher frequencies the ω^2 term in the denominator overpowers the contributions at low wave vectors k. Therefore, only the contributions at higher k values contribute significantly while integrating Equation (3). From the reciprocity between the wave vector and real space representations it follows that

 © 2013 Wiley-VCH Verlag GmbH & Co. KGaA, Weinheim

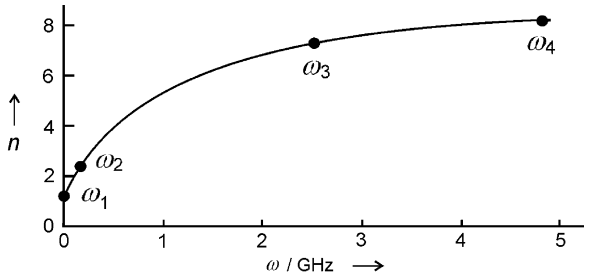

Figure 4. Exponent n characterizing the R^{-n} dependence of the spectral density function $J(\omega)$ for model A as a function of frequency.

the dominance of high k values corresponds to smaller R values, that is, to a shorter range.

However, one should recall that according to Equation (1) the experimental cross-relaxation rate σ_{IS} reflects a linear combination of $J(\omega_I-\omega_S)$ being of intrinsic long-range nature, and $J(\omega_I+\omega_S)$ having short-range character. Since the spectral density function decays monotonically, $J(\omega_I-\omega_S)$ always exceeds $J(\omega_I+\omega_S)$. The latter, however, is weighted six times as large as $J(\omega_I-\omega_S)$, resulting in a complex mixture of long-range and short-range effects. It depends on the particular conditions of the experiments, which part dominates.

In the case of **1** the term at $(\omega_I-\omega_S)$ largely overpowers that at $(\omega_I+\omega_S)$ in Equation (1), so that the measured cross-relaxation rate essentially reflects long-range behavior, if taken literally with an exponent of $n\cong2.5$. Thus, the NOE extends far beyond the first coordination sphere of the cation. Replacing the step function for the ion distribution by a more realistic pair distribution function $g(R)$, for example taken from MD simulations, may soften this long-range behavior. However, the redistribution of the ions into distinct layers essentially concerns interactions up to the second layer, whereas beyond this distance the step function is a good approximation. We therefore only expect minor changes in the R dependence of the NOE.

Taken together our analysis leads to the following conclusions:

- The spatial range captured by the NOE monotonously increases from high to low frequency, indicating a transition from R^{-6}-type short-range behavior to R^{-1}-type long-range behavior. Thus, the two contributions to the heteronuclear NOE at the frequencies $(\omega_I-\omega_S)$ and $(\omega_I+\omega_S)$ display a different R dependence.
- Under the conditions of the study of IL **1**,[7] and presumably for studies of other ILs as well, the contribution at the frequency $(\omega_I-\omega_S)$ largely overpowers that at $(\omega_I+\omega_S)$, resulting in a long-range NOE. Thus, the NOE says little about ions in direct contact, but captures spins far beyond the first coordination layer. Site-specific NOE measurements may therefore reflect the mean orientation of the ions over long distances rather than the local structure of distinct ion aggregates.
- A similar behavior is expected for the homonuclear ^{1}H-^{1}H NOE ($\omega_I=\omega_S$), for example probed in the study of cation–cation interactions in **1** by Mele et al.,[3c] where Equation (1) transcribes into the relation $\sigma_{II}=0.6J(2\omega)-0.1J(0)$. There the two frequencies are even more distant.
- The molecular-level cross-relaxation essentially reflects processes associated with translational motions of the ions. Rotational dynamics of the ions play a marginal role.

We conclude with some final remarks about the consequences of our findings for NOE studies in general:

- In the case of translational motions the broadly distributed dynamics can shift the spectral density to frequencies far below the spectrometer frequencies used in NOE experiments, so that data evaluations based on the extreme-narrowing situation are meaningless. According to the work by Furo and co-workers,[10] this result, pinpointed here for viscous ILs, applies even to systems of comparatively low viscosity.
- Accounting for differences in the model and technical methods, our conclusions are fully consistent with the results of some earlier theories of intermolecular spin relaxation,[11] and notably with theoretical work by Halle.[8] Our results go, however, beyond these studies because, as a striking feature, we observe the spatial range of the NOE to vary with frequency.
- The consistency of conclusions obtained for largely different systems such as ILs and protein solutions suggests that NOEs in many other liquids behave in an analogous fashion.

Received: April 2, 2013
Published online: June 17, 2013

Keywords: ionic liquids · molecular dynamics · NMR spectroscopy · nuclear Overhauser effect

[1] a) H. P. Mo, T. C. Pochapski, *Prog. Nucl. Magn. Reson. Spectrosc.* **1997**, *30*, 1–38; b) J. T. Gerig, *Annu. Rep. NMR Spectrosc.* **2008**, *64*, 21–76.
[2] D. Neuhaus, M. P. Williamson, *The Nuclear Overhauser Effect in Structural and Conformational Analysis*, 2nd ed., Wiley-VCH, Weinheim, **2000**.
[3] a) Y. Lingscheid, S. Arenz, R. Giernoth, *ChemPhysChem* **2012**, *13*, 261–266; b) D. Bankmann, R. Giernoth, *Prog. Nucl. Magn. Reson. Spectrosc.* **2007**, *51*, 63–90; c) A. Mele, G. Romanò, M. Giannone, E. Ragg, G. Fronza, G. Raos, V. Macon, *Angew. Chem.* **2006**, *118*, 1141–1144; *Angew. Chem. Int. Ed.* **2006**, *45*, 1123–1126; d) A. Mele, *Chim. Oggi/Chem. Today* **2010**, *28*, 48–53.
[4] a) *Ionic Liquids*, *Faraday Disc.*, *Vol. 154*, RSC Publishing, London, **2012**, pp. 454–457; b) H. Weingärtner, *Angew. Chem.* **2008**, *120*, 664–682; *Angew. Chem. Int. Ed.* **2008**, *47*, 654–670.
[5] C. Schröder, C. Wakai, H. Weingärtner, O. Steinhauser, *J. Chem. Phys.* **2007**, *126*, 084511.
[6] For experimental studies see: a) C. Daguenet, P. J. Dyson, I. Krossing, A. Oleinikova, J. Slattery, H. Weingärtner, *J. Phys. Chem. B* **2006**, *110*, 12682–12688; b) R. Buchner, G. Hefter, *Phys. Chem. Chem. Phys.* **2009**, *11*, 8984–8999. For MD simulations see: c) C. Schröder, M. Haberler, O. Steinhauser, *J. Chem. Phys.* **2008**, *128*, 134501; d) C. Schröder, O. Steinhauser, *J. Chem. Phys.* **2009**, *131*, 114504.
[7] K. Modig, E. Liepinsh, G. Otting, B. Halle, *J. Am. Chem. Soc.* **2004**, *126*, 102–114.
[8] B. Halle, *J. Chem. Phys.* **2003**, *119*, 12372–12385.

 © 2013 Wiley-VCH Verlag GmbH & Co. KGaA, Weinheim

[9] S. Gabl, H. Weingärtner, O. Steinhauser, in preparation.
[10] L. Nordstierna, P. V. Yushmanov, I. Furo, *J. Chem. Phys.* **2006**, *125*, 074704.
[11] a) A. Abragam, *The Principles of Nuclear Magnetism*, Clarendon, Oxford, **1961**, chap. VIII, pp. 300 – 305; b) Y. Ayant, E. Belorizky, P. Fries, J. Rosset, *J. Phys. (Paris)* **1977**, *38*, 325 – 337; c) L.-P. Hwang, J. H. Fried, *J. Chem. Phys.* **1975**, *63*, 4017 – 4025; d) for a review of early theoretical and experimental work see: "Nuclear spin relaxation and intermolecular interactions": H. G. Hertz, A. Kratochwill, H. Weingärtner in *Stud. Phys. Theor. Chem.*, *Vol. 37* (Eds.: W. J. Orville-Thomas, H. Ratjczak, C. N. R. Rao), Elsevier, Amsterdam, **1985**, chap. 8.
[12] C. Schröder, O. Steinhauser, unpublished results.
[13] K. Hayamizu, S. Tsuzuki, S. Seki, Y. Umebayasi, *J. Phys. Chem. B* **2012**, *116*, 11284 – 11291.

 © 2013 Wiley-VCH Verlag GmbH & Co. KGaA, Weinheim

5 Pair dynamics and the intermolecular nuclear Overhauser effect (NOE) in liquids analysed by simulation and model theories: Application to an ionic liquid

Reprinted with permission from *The Journal of Chemical Physics* **140**, 184503 (2014); DOI: 10.1063/1.4874155. Copyright 2014, AIP Publishing LLC.

Pair dynamics and the intermolecular nuclear Overhauser effect (NOE) in liquids analysed by simulation and model theories: Application to an ionic liquid

Sonja Gabl, Christian Schröder, Daniel Braun, Hermann Weingärtner, and Othmar Steinhauser

Citation: The Journal of Chemical Physics **140**, 184503 (2014); doi: 10.1063/1.4874155
View online: http://dx.doi.org/10.1063/1.4874155
View Table of Contents: http://scitation.aip.org/content/aip/journal/jcp/140/18?ver=pdfcov
Published by the AIP Publishing

Articles you may be interested in

Effect of ion structure on conductivity in lithium-doped ionic liquid electrolytes: A molecular dynamics study
J. Chem. Phys. **139**, 114508 (2013); 10.1063/1.4821155

Studies of structural, dynamical, and interfacial properties of 1-alkyl-3-methylimidazolium iodide ionic liquids by molecular dynamics simulation
J. Chem. Phys. **136**, 124706 (2012); 10.1063/1.3696004

Rotational dynamics of benzene and water in an ionic liquid explored via molecular dynamics simulations and NMR T 1 measurements
J. Chem. Phys. **136**, 074508 (2012); 10.1063/1.3685100

Heterogeneous dynamics of ionic liquids from molecular dynamics simulations
J. Chem. Phys. **129**, 194501 (2008); 10.1063/1.3005372

Ab initio molecular dynamics simulation of ionic liquids
J. Chem. Phys. **126**, 154502 (2007); 10.1063/1.2718531

This article is copyrighted as indicated in the article. Reuse of AIP content is subject to the terms at: http://scitation.aip.org/termsconditions. Downloaded to IP: 131.130.40.8 On: Mon, 12 May 2014 08:38:19

THE JOURNAL OF CHEMICAL PHYSICS **140**, 184503 (2014)

Pair dynamics and the intermolecular nuclear Overhauser effect (NOE) in liquids analysed by simulation and model theories: Application to an ionic liquid

Sonja Gabl,[1] Christian Schröder,[1] Daniel Braun,[1] Hermann Weingärtner,[2] and Othmar Steinhauser[1]
[1]*Department of Computational Biological Chemistry, University of Vienna, Waehringer Strasse 17, A-1090 Wien, Austria*
[2]*Physical Chemistry II, Ruhr-University of Bochum, D-44780 Bochum, Germany*

(Received 10 February 2014; accepted 16 April 2014; published online 9 May 2014)

Combining simulation and model theories, this paper analyses the impact of pair dynamics on the intermolecular nuclear Overhauser effect (NOE) in liquids. For the first time, we give a distance resolved NOE. When applied to the ionic liquid 1-ethyl-3-methyl-imidazolium tetrafluoroborate the NOE turns out to be of long-range nature. This behaviour translates to the experimentally measured cross- and longitudinal relaxation rates. We were able to calculate the heteronuclear NOE from simulation data, despite the high computational effort. Model theories are computationally less demanding and cover the complete frequency range of the respective spectral density function, they are usually based on a very simple pair distribution function and the solution of the diffusion equation. In order to model the simulated data sufficiently, these simplifications in structure and dynamics have to be generalised considerably. © *2014 AIP Publishing LLC*. [http://dx.doi.org/10.1063/1.4874155]

I. MOTIVATION

So far experimental, theoretical, and computational methods have provided numerous information on structural and dynamical properties of liquids and solutions. With respect to dynamical properties, the available information covers both, single-particle motions as well as the collective dynamics of many particles. What is really missing are thorough studies of the pair dynamics.

The nuclear Overhauser effect (NOE) reveals the cross-relaxation between two nuclear spins and is a classical experimental probe for pair structures and pair dynamics.[1,2] Since the advent of biomolecular structure determinations, which are now one of the most important applications of NMR spectroscopy,[3] NOE studies have almost exclusively focused on structural information provided by intramolecular relaxation processes. In studies of intermolecular NOEs, dynamics has been considered a cumbersome factor rather than a source of useful information.

The physical foundation of the NOE is the coupling of the magnetic dipole moments of two spins, I and S, by magnetic dipole-dipole interaction. The fluctuation of this interaction due to molecular motions gives rise to magnetisation transfer and cross relaxation.[1,2] This fluctuation decays with the sixth power of the distance r between the spins, so that the fluctuation of the dipole-dipole interaction within the very same molecule is driven by the reorientational dynamics of the spin-carrying molecule. In the long known Solomon theory,[1] this r^{-6} distance dependence of the fluctuation of the dipole-dipole interaction propagates into the expression for the *intramolecular* cross-relaxation rate. Thus, the NOE provides local information due to interactions between spins which are close to each other in space (as a rule of thumb <5 Å).

Over the years there have been many experimental attempts to apply the same methodology to *intermolecular* relaxation processes, where the spins are located in separate molecules.[4–6] In the spirit of the r^{-6} dependence established for the intramolecular case, it is usually conjectured that the intermolecular NOE maps local structures as well.[4] However, it has repeatedly been pointed out that intermolecular dipole-dipole relaxation is by far more complex than intramolecular relaxation. The rationale is that in addition to molecular reorientation the fluctuation of the dipole-dipole interaction is also modulated by translational displacements of the molecules.

If the locations of the spins coincide with the centres of mass of the molecules translational motion is the only relevant mechanism. Based on a random flight model for intermolecular spin relaxation, Torrey[7] has shown many years ago that in such cases the spin relaxation rate can exhibit a $1/r$ type distance dependence. Moreover, Torrey showed that this long-range distance dependence persists in the limit of small-step displacements of the particles. Torrey's conjecture of a long-range relaxation process was later confirmed in theories based on continuous small-step diffusion by Abragam,[8] Ayant *et al.*,[9] Hwang and Freed,[10] and Sholl.[11] Going beyond the purely translational case Ayant *et al.*[12] have considered a model, in which the spins are located off-centre in the molecules, so that both, translational and rotational motions are relevant. Later, Halle[13] has incorporated non-uniform diffusion into such a model. Proceeding along a very different path, Zeidler[14] has modeled the off-centre effect in terms of a distance-dependent orientational correlation function.

It is important to note that, except for Halle's work,[13] these theories do not directly model the NOE, but consider longitudinal (spin-lattice) relaxation. The classical Solomon theory of spin relaxation results in a relaxation matrix, in

 © 2014 AIP Publishing LLC

This article is copyrighted as indicated in the article. Reuse of AIP content is subject to the terms at: http://scitation.aip.org/termsconditions. Downloaded to IP: 131.130.40.8 On: Mon, 12 May 2014 08:38:19

which the diagonal elements are related to the longitudinal relaxation rates, ρ_{ii}, while the off-diagonal elements are related to the cross-relaxation rates, σ_{ik} $(i, k = I, S)$.[1] Please note, that longitudinal relaxation involves dipolar and non-dipolar contributions, while cross relaxation is purely dipolar. Because cross relaxation and the dipolar part of longitudinal relaxation reflect the same dynamical processes they have the same theoretical basis.

In the work presented here, we report on a new NOE theory, having several goals in mind: First, we aim to incorporate the NOE into a comprehensive theory of pair dynamics in liquids. With regard to dynamics existing theoretical approaches all resort to approximations and limiting cases. Except for Torrey's random flight model[7] all approaches rely on continuous small step translational and rotational diffusion, which in a more general context represent Gaussian diffusion models. Our theory enables us to derive expressions for quite a general time dependence of pair dynamics. In particular, we study nonlinear time behaviour as well as non-Gaussian processes. In the latter case, we will try translational and rotational jump diffusion models, which are often encountered in liquid state dynamics, and translational diffusion on a lattice.

Second, the different distance dependencies of intramolecular and intermolecular relaxation pose the question of how far apart spin pairs have to be to contribute to the NOE. This requires theoretical expressions, which explicitly depend on the spin-spin distance r. In a previous publication,[15] based on a model theory, we have tried to give a first answer to this question, which implies that frequency does matter for the spatial range of the NOE. Because the experiment only measures the full NOE built up by all spin pairs, and does not say anything about the distance dependence, the available relaxation theories have not attempted to explicitly resolve this distance dependence.[8–10,12] Only Halle[13] has attempted to explore in his model the spatial range by introducing a repulsive wall into his theory, which allows to cut off the contributions to the NOE beyond a given distance. To gain a more detailed physical picture we will derive explicit expressions for the distance dependence of the NOE.

Third, we intensively analyse simulation trajectories to have independent data for a critical assessment of our model theory that goes beyond a global comparison with the experimental data. Reported simulations of the NOE, e.g., Lennard-Jones systems,[16,17] liquid acetonitrile,[18] liquid methanol,[19] Xenon dissolved in benzene,[20] and peptides dissolved in water-methanol mixtures[21] do not consider the spatial dependence of the NOE. The development of a rational way to extract the cross-correlation rate from simulation trajectories is a non-trivial problem. In fact, the computation of the range of the spatial NOE is intimately connected with the size and time dependence of computer simulations, involving highly charged molecules.[22]

The model system for testing our theory is the widely used room temperature ionic liquid[23,24] (IL) 1-ethyl-3-methyl-imidazolium tetrafluoroborate [EMIM][BF_4]. Our interest in the pair dynamics and NOE of ionic liquids is founded in previous works, in which we have extensively exploited simulations[25–32] and experimental dielectric spectroscopy[33–36] in order to characterise and understand the collective reorientational and translational dynamics of the ions in ionic liquids, as revealed by their frequency-dependent dielectric permittivity. Complementary to dielectric spectroscopy is solvation spectroscopy probing the relaxation of the electric field in the solvent induced by the excitation of a chromophore solute.[37]

Since Mantz *et al.*[38] have demonstrated in case of chloroaluminate salts that NOE experiments can be employed to study ion interaction in neat ionic liquids, there have been several studies of cation-cation and cation-anion configurations in such systems.[39–43] Reviews of these cross-relaxation studies of ionic liquids[44,45] and of spin relaxation studies of such systems in more general[46] are available. To render simulations feasible at sufficiently long simulation times, we have resorted to the less viscous [EMIM][BF_4] as a simple representative, replacing the homologous 1-butyl-3-methylimidazolium $[BMIM]^+$-ions in [BMIM][BF_4] considered in our preceding paper[15] by the simpler $[EMIM]^+$-ion.

This paper is organised as follows: First, we present our model theory in two stages, starting with pure translation, followed by ro-translational coupling and off-centre effects. After a short chapter on simulation details, we enter the results and discussion section. The implications for experiment are given next, to be followed by the conclusion.

II. THEORY

A. Cross-relaxation and dipole-dipole interaction

Literature offers a variety of experimental methods for determining cross-relaxation rates.[2] Only the heteronuclear version of the classical NOESY experiment in the Zeemann (laboratory) frame is of interest here. The cross-relaxation rate collects all pair contributions of the spin species I and S, where by convention I denotes the nucleus, whose spectrum is measured, and S its interaction partner. In the NOESY experiment the cross-relaxation rate is given as

$$\sigma_{IS}^{NOE} = \frac{1}{10}[-J(\omega_I - \omega_S) + 6J(\omega_I + \omega_S)] = -\frac{1}{10}J(\omega_I - \omega_S)\left[1 - \frac{6J(\omega_I + \omega_S)}{J(\omega_I - \omega_S)}\right]. \quad (1)$$

Here, $J(\omega_I + \omega_S)$ is the spectral density function at the sum frequency and $J(\omega_I - \omega_S)$ that at the difference frequency of the interacting nuclei. The longitudinal relaxation rate in the laboratory frame is

$$\rho_{II}^{NOE} = \frac{1}{10}[J(\omega_I - \omega_S) + 3J(\omega_I) + 6J(\omega_I + \omega_S)] = \frac{1}{10}J(\omega_I - \omega_S)\left[1 + \frac{3J(\omega_I) + 6J(\omega_I + \omega_S)}{J(\omega_I - \omega_S)}\right]. \quad (2)$$

Furthermore, an interesting quantity is the NOE-enhancement $f_I\{S\}$, measuring the magnetisation transfer from spin I to spin S. It is given by the ratio of σ_{IS}^{NOE} and ρ_{II}^{NOE},

$$f_I\{S\} = \frac{\sigma_{IS}^{NOE}}{\rho_{II}^{NOE}} = (-1)\cdot\frac{1 - \frac{6J(\omega_I+\omega_S)}{J(\omega_I-\omega_S)}}{1 + \frac{3J(\omega_I)+6J(\omega_I+\omega_S)}{J(\omega_I-\omega_S)}}. \quad (3)$$

This article is copyrighted as indicated in the article. Reuse of AIP content is subject to the terms at: http://scitation.aip.org/termsconditions. Downloaded to IP: 131.130.40.8 On: Mon, 12 May 2014 08:38:19

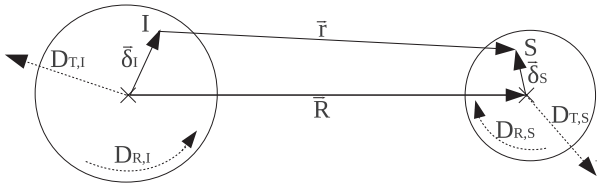

FIG. 1. Model for the dynamics governing intermolecular cross-relaxation between the spins I and S.

It is seen that the different relaxation rates pick up spectral densities at distinct frequencies and probe different linear combinations of the spectral densities. For an arbitrary frequency ω the spectral density function $J(\omega)$ is the Fourier transform,

$$J(\omega) = K_{IS}\int_0^\infty G(t)e^{i\omega t}dt = K_{IS}\cdot\mathcal{F}[G(t)], \tag{4}$$

of the time correlation function $G(t)$,

$$G(t) = \frac{1}{N_I}\sum_{i=1}^{N_I}\sum_{j=1}^{N_S} g_{ij}(t) \tag{5}$$

representing the average over all pair contributions

$$g_{ij}(t) = \langle \overleftrightarrow{T}_{ij}(0)\cdot \overleftrightarrow{T}_{ij}(t)\rangle, \tag{6}$$

from neighbouring spins coupled by the dipole-dipole tensor $\overleftrightarrow{T}_{ij}$,

$$\overleftrightarrow{T}_{ij} = \vec{\nabla}_R\vec{\nabla}_R\frac{1}{R_{ij}} = \frac{1}{R_{ij}^3}\left(\frac{3\vec{R}_{ij}:\vec{R}_{ij}}{R_{ij}^2} - \overleftrightarrow{I}\right), \tag{7}$$

involving the mutual distance vector $\vec{R}_{ij} = \vec{R}_i - \vec{R}_j$. $\overleftrightarrow{I}$ is the unit tensor. $K_{IS} = [(\mu_0/4\pi)\hbar\gamma_I\gamma_S]^2$ is the dipolar coupling constant, where γ_I and γ_S are the magnetogyric ratios of the spins, and μ_0 is the permeability of the vacuum. For ^{1}H-^{19}F spin pairs K_{IS} is 5.04×10^{11} Å^6 s^{-2}. Furthermore, N is the number of molecules and V is the volume.

Our model for the pair dynamics is shown in Fig. 1. When considering purely translational motion, the vector $\vec{R}$ entering Eq. (7) is the centre of mass distance vector, joining the molecules I and S, which in this case coincides with the spin-spin distance vector $\vec{r}$. In case of rotational motion we have to replace $\vec{R}$ by the off-centre spin-spin distance vector $\vec{r}$ as shown in Fig. 1. Noting that the vector sum $\vec{R}+\vec{\delta}_S-\vec{\delta}_I-\vec{r}$ must be zero, we obtain $\vec{r} = \vec{R}-\vec{\rho}$, where $\vec{\rho} = \vec{\delta}_I - \vec{\delta}_S$ is the difference vector of the off-centre displacements. We note that a similar model forms the basis of the theory of Ayant *et al.*[12] Moreover, in adapting relaxation theory to protein hydration, Halle[13] has accounted for an off-centre location of ^{1}H in the protein, but has neglected the off-centre displacement of ^{1}H in water.

B. Pure translation

As a first step, we replace the Cartesian expression for the dipole-dipole tensor in Eq. (7) by

$$T_m^2 = \frac{1}{R^3}Y_m^2(\Omega). \tag{8}$$

This spherical representation facilitates the following derivation as several theorems for spherical harmonics Y_m^l can be exploited. Consequently, we use the equivalent formula

$$g(t) = \left\langle \frac{1}{R_0^3}Y_m^2(\Omega_0)\cdot\frac{1}{R^3}Y_m^2(\Omega)\right\rangle \tag{9}$$

instead of Eq. (6). Thereby, $\vec{R}_0$ stands for $\vec{R}(0)$ and $\vec{R}$ abbreviates $\vec{R}(t)$. Furthermore, we omitted the pair index ij for simplification. An analogous notation is used for Ω and Ω_0, which is a comprehensive notation for the polar and azimuth angle θ and ϕ. The summation over all spin pairs according to Eq. (5) may be written as an integral over the initial distribution of distances, given by $g(R_0)$,

$$G(t) = \frac{N}{V}\int_0^{R_{up}} d\vec{R}_0\, g(R_0)\int_0^\infty d\vec{R}\,\frac{1}{R_0^3}Y_{2m}^l(\Omega_0) \times P(\vec{R},t|\vec{R}_0;t=0)\frac{1}{R^3}Y_{2m}^l(\Omega). \tag{10}$$

Here, $g(R_0)$ is the pair correlation function, which may be a simple step function or the detailed radial distribution function $g_{000}(R_0)$, where the label 000 refers to the correlation between molecular centres. The upper integration limit of the pair correlation function is considered variable as a means to constrain the contribution of pairs to a certain range of distances $[0-R_{up}]$. Thus, we are modeling the spatial range of the NOE. The time evolution of the distance vectors is described by the propagator

$$P(\vec{R},t\mid\vec{R}_0;t=0) = \langle\delta(\vec{R}-\vec{R}_{ij}(t))\delta(\vec{R}_0-\vec{R}_{ij}(0))\rangle \tag{11}$$

with the initial condition $P(t=0) = \delta(\vec{R}-\vec{R}_0)$. It represents the probability, that the pair distance vector is $\vec{R}_{ij}(t)$ at time t, provided it was $\vec{R}_{ij}(0)$ at $t=0$. If the pair displacement in this propagator is replaced by the single-particle displacement, the resulting expression corresponds to the self-contribution $G_s(\vec{R}_0,\vec{R},t)$ of the well-known van Hove correlation function.[47] Upon Fourier transformation, we get

$$P(\vec{R},t\mid\vec{R}_0;t=0) = \sum_{\vec{k}} K(\vec{k},t)e^{i\vec{k}(\vec{R}-\vec{R}_0)}, \tag{12}$$

with the exact kernel

$$K(\vec{k},t) = \langle e^{i\vec{k}(\vec{R}_{ij}(t)-\vec{R}_{ij}(0))}\rangle. \tag{13}$$

For simplification we write the exponent in a shorter notation by setting

$$d(t) = \vec{k}\cdot\left(\vec{R}_{ij}(t)-\vec{R}_{ij}(0)\right). \tag{14}$$

The kernel would correspond to the intermediate scattering function in quasi-elastic neutron scattering,[47] if the pair displacement is replaced by the single-particle displacement. The kernel will be discussed in greater detail in Sec. II B 1. The summation in Eq. (12) runs over the wave vector $\vec{k}$, being the generator of translational motion. Later on we will encounter its rotational analogue, angular momentum l. With the aid of the Rayleigh expansion for $e^{i\vec{k}\vec{R}}$ and $e^{i\vec{k}\vec{R}_0}$,

$$e^{i\vec{k}\vec{R}} = 4\pi\sum_{l,m} i^l j_l(kR)Y_m^l(\Omega_k)Y_m^l(\Omega_R) \tag{15}$$

This article is copyrighted as indicated in the article. Reuse of AIP content is subject to the terms at: http://scitation.aip.org/termsconditions. Downloaded to IP: 131.130.40.8 On: Mon, 12 May 2014 08:38:19

and exploiting the orthogonality of the spherical harmonics

$$\int d\Omega\, Y_m^l(\Omega) Y_{m'}^{l'}(\Omega) = \delta_{ll'}\delta_{mm'}. \tag{16}$$

We add that j_l are the spherical Bessel functions. Equation (10) can be further simplified to

$$J(\omega) = K_{IS} \cdot \frac{N}{V} \cdot \int_0^{R_{up}} dR_0\, g(R_0) \frac{1}{R_0} \int_0^{\infty} dR \times \frac{1}{R} \int dk\, k^2 j_2(kR) j_2(kR_0) \mathcal{F}[K(\vec{k}, t)]. \tag{17}$$

Thereby, we have replaced the summation over k by an integral. The Cartesian volume elements $d\vec{k}$ and $d\vec{R}$ were rewritten in polar coordinates, $d\vec{R} = R^2 dR d\Omega_R$ and $d\vec{k} = k^2 dk d\Omega_k$. From the last equation, it is obvious that the dependence on the time t can only be found in the kernel and therefore, will solely be altered during Fourier transformation (Eq. (4)). In other words, the time correlation function $G(t)$ and $J(\omega)$ obey the same formula if the time kernel is replaced by its Fourier transform $\mathcal{F}[K(\vec{k}, t)]$.

Although restricted to pure translation, this expression shows already the twofold strategy of our model theory: On the one hand the detailed structure is modeled via the pair correlation function $g(R_0)$, on the other hand the complexity of pair dynamics is described by the kernel.

1. Cumulant expansion of the kernel

Here, we use a cumulant expansion[48] for the exact kernel Eq. (13),

$$K(\vec{k}, t) = e^{-k^2\rho_1(t) + k^4\rho_2(t) - k^6\rho_3(t) + \cdots}. \tag{18}$$

In the Gaussian approximation we truncate this expansion after the first term and insert

$$\rho_1(t) = \frac{1}{2!}\langle d^2(t)\rangle \tag{19}$$

in conjunction with Eq. (14). In an isotropic medium all directions are equivalent and we can write

$$\langle d^2(t)\rangle = \frac{1}{3}\left\langle [\vec{R}_{ij}(t) - \vec{R}_{ij}(0)]^2 \right\rangle. \tag{20}$$

Now, the kernel is solely determined by the pair displacement

$$K(\vec{k}, t) = e^{-k^2 \frac{1}{6}\langle [\vec{R}_{ij}(t) - \vec{R}_{ij}(0)]^2\rangle}. \tag{21}$$

Approximating the pair displacement $\langle [\vec{R}_{ij}(t) - \vec{R}_{ij}(0)]^2\rangle$ by its asymptotic value $6D_T t$, we get the simple kernel

$$K(\vec{k}, t) = e^{-k^2 D_T t}. \tag{22}$$

Its temporal Fourier transform is given by

$$\mathcal{F}[K(\vec{k}, t)] = \frac{D_T k^2}{(D_T k^2)^2 + \omega^2}. \tag{23}$$

If the kernel in Eq. (22) is inserted into Eq. (12) we recover after some algebra Abragam's well-known propagator[8]

$$P(\vec{R}, t \mid \vec{R}_0; t = 0) = (4\pi D_T t)^{-3/2} e^{\frac{-(\vec{R} - \vec{R}_0)^2}{4D_T t}}, \tag{24}$$

which is also a solution of the diffusion equation

$$D_T \Delta P = \frac{\partial P}{\partial t}. \tag{25}$$

Except for Torrey's theory[7] and the use of regional D_T by Halle,[13] the propagator introduced by Abragam underlies all model theories for translational spin relaxation reported so far. Throughout this paper, we will refer to the solution of the diffusion equation with the term "simple diffusion."

It is important to recall that the diffusion coefficient D_T in the kernel, as given in Eq. (22), which transcribes into the propagator, is the pair diffusion coefficient defined with regard to the pair displacement $\langle [\vec{R}_{IS}(t) - \vec{R}_{IS}(0)]^2\rangle$ of the particles, which can be rewritten as

$$\begin{aligned}\langle [\vec{R}_{IS}(t) - \vec{R}_{IS}(0)]^2\rangle &= \langle [\vec{R}_I(t) - \vec{R}_I(0)]^2\rangle + \langle [\vec{R}_S(t) - \vec{R}_S(0)]^2\rangle \\ &\quad - 2\langle [\vec{R}_I(t) - \vec{R}_I(0)] \cdot [\vec{R}_S(t) - \vec{R}_S(0)]\rangle.\end{aligned} \tag{26}$$

In the theories of intermolecular relaxation[8–10,13] it is generally assumed that pair diffusion can be approximated by an independent translational motion of the two interacting particles. In the latter case the pair diffusion coefficient D_T can be replaced by the sum of the self-diffusion coefficients of the interacting particles, $D_T \approx D_{T,I} + D_{T,S}$, under the assumption that the cross-term $-2\langle [\vec{R}_I(t) - \vec{R}_I(0)] \cdot [\vec{R}_S(t) - \vec{R}_S(0)]\rangle$ can be neglected. The self-diffusion coefficients $D_{T,i}$ ($i = I, S$) are related to the Einstein mean-square displacement $\langle [\vec{R}_i(t) - \vec{R}_i(0)]^2\rangle$ of the single particles.

The concept of simple diffusion, provided by Eq. (22), can be extended in two directions, concerning the time axis or k-space, respectively. We will address the time axis first.

2. Beyond simple diffusion

Simple diffusion considers motion of the molecules only in the asymptotic time-region. In order to elucidate pair dynamics at shorter times, we rewrite the pair displacement in terms of the respective velocity correlation function

$$\langle [\vec{R}_{IS}(t) - \vec{R}_{IS}(0)]^2\rangle = 2t \int_0^t dt' \langle \vec{v}_{IS}(0)\vec{v}_{IS}(t')\rangle - 2\int_0^t dt' \langle \vec{v}_{IS}(0)\vec{v}_{IS}(t')\rangle \cdot t'. \tag{27}$$

For sufficiently long times, the velocity correlation function levels off to zero, resulting in a linear time dependence for the pair displacement

$$\lim \langle [\vec{R}_{IS}(t) - \vec{R}_{IS}(0)]^2\rangle = 6D_T(t - \tau_0), \tag{28}$$

with the diffusion coefficient D_T and τ_0 given by

$$D_T = \frac{1}{3}\int_0^{\infty} dt \langle \vec{v}_{IS}(0)\vec{v}_{IS}(t)\rangle, \tag{29}$$

$$\tau_0 = \frac{1}{3D_T}\int_0^{\infty} dt \langle \vec{v}_{IS}(0)\vec{v}_{IS}(t)\rangle \cdot t. \tag{30}$$

It depends on the type of velocity correlation function, whether τ_0 is positive or negative, as depicted in Fig. 2 by the two straight lines in orange and cyan. In the next two paragraphs, we will discuss the deviation from the straight lines at

This article is copyrighted as indicated in the article. Reuse of AIP content is subject to the terms at: http://scitation.aip.org/termsconditions. Downloaded to IP: 131.130.40.8 On: Mon, 12 May 2014 08:38:19

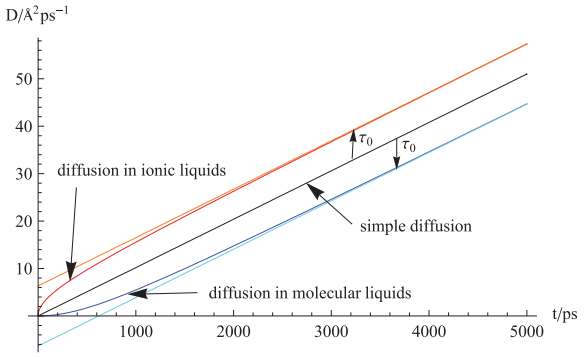

FIG. 2. Simple diffusion is given in black, whereas the characteristic shape of diffusion in molecular liquids is given in blue. The mean-squared pair displacement for our ionic liquid ([EMIM][BF_4]), gained from simulation data, is given in red. The asymptotic approximation of $6D_T(t+\tau_0)$ is shown in orange and $6D_T(t-\tau_0)$ is given in cyan.

shorter times for the two cases, diffusion in neutral molecular liquids and diffusion in ionic liquids.

a. Diffusion in molecular liquids. A typical mean-square displacement for a neutral, molecular liquid, governed by dipolar forces, is given in Fig. 2 in blue. In this case, the velocity correlation function is essentially positive and can thus be modeled mono-exponentially typical for Langevin dynamics. When inserted into Eq. (27), this leads to a pair displacement of the form

$$\langle[\vec{R}_{IS}(t)-\vec{R}_{IS}(0)]^2\rangle = 6D_T[t+\tau_0(e^{-\frac{t}{\tau_0}}-1)] \tag{31}$$

and subsequently to a kernel of the form

$$K(k,t) = e^{-k^2 D_T[t+\tau_0(e^{-\frac{t}{\tau_0}}-1)]}. \tag{32}$$

Unfortunately, the Fourier transform of the new kernel does not have an analytic expression. Egelstaff[49] found a numerical substitute

$$\langle[\vec{R}_{ij}(t)-\vec{R}_{ij}(0)]^2\rangle = 6D_T\left[\sqrt{t^2+\tau_0^2}-\tau_0\right], \tag{33}$$

with an analytic expression for the Fourier transform

$$\mathcal{F}\left[\exp\left[-D_T k^2\left(\sqrt{t^2+\tau_0^2}-\tau_0\right)\right]\right] = \frac{D_T k^2}{(D_T k^2)^2+\omega^2}\cdot x K_1(x). \tag{34}$$

Here, $x=\tau_0\sqrt{(D_T k^2)^2+\omega^2}$ and K_1 is the Bessel function of the second kind. $xK_1(x)$ is a monotonic decaying function, which starts at a value of 1. This is important, because it simultaneously dampens high values of k as well as frequencies ω.

b. Diffusion in ionic liquids. The actual mean-squared displacement for our ionic liquid is calculated from simulation data and shown in red in Fig. 2. The apparent difference to molecular liquids is the inversion of the curvature and the negative sign of τ_0. Both stem from the oscillatory behaviour of the velocity correlation function, which in its turn is caused by strong Coulomb forces of charged species. The negative regions of the oscillations, following the positive ones, are more amplified by the time t and thus resulting in a negative τ_0. In our model theory we need an analytic expression for the pair displacement.

From the visual inspection of Fig. 2, we tried the inverse function of Eq. (33) resulting in

$$\langle[\vec{R}_{ij}(t)-\vec{R}_{ij}(0)]^2\rangle = 6D_T\sqrt{(t+\tau_0)^2-\tau_0}. \tag{35}$$

To validate this model function, we fitted it to the pair displacement derived from our simulation data. The excellent fit resulted in a pair diffusion coefficient $D_T = 17\times10^8$ Å^2 s^{-1} and $\tau_0 = 0.66\times10^{-9}$ s. This clearly shows two facts: First, τ_0 stands for the time until the pair displacement gets linear, which roughly takes 1 ns. Second, the sum of the single particle diffusion coefficient of the cation $D_{T,I}$ and of the anion $D_{T,S}$ equals 17×10^8 Å^2 s^{-1}. This shows that the cross-term between cation and anion of Eq. (26) can be neglected. Consequently, the pair diffusion coefficient can be approximated by the sum of the single particle diffusion coefficients, which are experimentally accessible.

The only drop of bitterness is that we could not find an analytic expression for the Fourier-transform of the respective kernel. Hence, we used the asymptotic approximation $6D_T(t+\tau_0)$ (given as the orange line in Fig. 2) instead. This modifies the kernel of Eq. (23) to

$$\mathcal{F}\left[\exp\left[-D_T k^2\sqrt{(t+\tau_0)^2-\tau_0}\right]\right] \approx \frac{D_T k^2}{(D_T k^2)^2+\omega^2}\cdot e^{-D_T k^2\tau_0}. \tag{36}$$

3. Non-Gaussian diffusion models

Inspired by recent, experimental work of Kremer *et al.*[50] we looked for an alternative route to go beyond simple diffusion. In contrast to simple or continuous diffusion, translational pair dynamics may be modeled as a succession of jumps of duration τ_{jump}.[49,51,52] Nevertheless, between two jumps pairs still follow simple diffusion, such that the jump length λ_h is given by

$$\lambda_h^2 = 6D_T\tau_{jump}. \tag{37}$$

To incorporate this model in the framework of our theory, the kernel has to be changed appropriately. Boon and Yip[48] accomplished this by introducing a new class of kernels of the following type:

$$K(\vec{k},t) = e^{-f(k)t} \tag{38}$$

and its Fourier transform, being

$$\mathcal{F}[e^{-f(k)t}] = \frac{f(k)}{(f(k))^2+\omega^2}. \tag{39}$$

As the dependence on k^2, i.e., the Gaussian behaviour, is now replaced by a more complex function in k, one speaks of Non-Gaussian models.

For the model of jump diffusion $f(k)$ is given by

$$f(k) = \frac{D_T k^2}{1+D_T k^2\tau_{jump}}. \tag{40}$$

For $\tau_{jump}=0$ we recover simple diffusion.

This article is copyrighted as indicated in the article. Reuse of AIP content is subject to the terms at: http://scitation.aip.org/termsconditions. Downloaded to IP: 131.130.40.8 On: Mon, 12 May 2014 08:38:19

A second representative is lattice diffusion,[48] whose $f(k)$ is given by

$$f(k) = \frac{1}{\tau_{lat}}\left(1 - \frac{\sin(kL)}{kL}\right), \tag{41}$$

where L is the characteristic lattice spacing, with the following condition:

$$L^2 = 6D_T\tau_{lat}. \tag{42}$$

Both, L and λ_h, are calculated according to simple, continuous diffusion, but discretisation is accounted for by different functional forms of $f(k)$.

C. Ro-translational coupling and off-centre effect

As relaxing spins are located off-centre, we have to include their rotational motion. It is often assumed that translational and rotational effects can be decoupled and are additive (cf. Eq. (9) of Ref. 53). In the following we will show that ro-translational coupling cannot be ignored and is therefore essential. In technical terms the vector $\vec{R}$, joining molecular centres, has to be replaced by $\vec{R} - \vec{\rho}$, where $\vec{\rho} = \vec{\delta}_I - \vec{\delta}_S$ is the difference vector of the off-centre displacements, as already mentioned above. Therefore, the T-tensor has to be generalised to

$$\overleftrightarrow{T} = \vec{\nabla}_R\vec{\nabla}_R\frac{1}{|\vec{R} - \vec{\rho}|}. \tag{43}$$

For a better handling of this expression, we do a multipole expansion

$$\frac{1}{|\vec{R} - \vec{\rho}|} = \frac{1}{R}\cdot\sum_{l=0}^{\infty}\sum_{m=-l}^{+l}\frac{1}{2l+1}\left(\frac{\rho}{R}\right)^l Y_m^l(\hat{R})Y_m^{l*}(\hat{\rho}). \tag{44}$$

Although the multipole expansion is justified by the fact that $R > \rho$, i.e., $\frac{\rho}{R} < 1$, the two distances must be notably different to obtain rapid convergence. While Fig. 1 intuitively suggests that this condition is obeyed, this problem turns out to be subtle, if the interacting particles are of very different size. An illustrative example is Halle's study of protein hydration,[13] where the radii of the protein, R_P, and of water, R_W, are largely different. Assuming that the protons of the protein are located at the protein's surface, we have $\delta_I \approx R_P$ and $\delta_S \ll \delta_I$ (Halle sets $\delta_S = 0$). It is easily seen from Fig. 1, that in this case for the water molecules in the first hydration sphere ρ approaches R.

Corresponding to Eq. (43), we have to take the second derivative of the multipole expansion (Eq. (44)). In a spherical representation of the T-tensor this corresponds to an increase of the angular momentum l by 2 as, for example, visible in the following equation:

$$\frac{\partial^2}{\partial Z^2}\frac{1}{R^{l+1}}Y_m^l(\hat{R}) = C_{l,m}\frac{1}{R^{l+3}}Y_m^{l+2}(\hat{R}). \tag{45}$$

Here, Z refers to the z-component of the distance vector $\vec{R}$ and the constant $C_{l,m}$ is given by[12]

$$C_{l,m} = \left[\left(\frac{2l+1}{2l+5}\right)(l+2-m) \times (l+1-m)(l+2+m)(l+1+m)\right]^{1/2}. \tag{46}$$

Combining the last four formulae, we get the intermediate expression

$$g(t) = \sum_{l,l'=0}^{\infty}\sum_{m=-l}^{+l}\sum_{m'=-l'}^{+l'} C_{l,m}^2\frac{1}{(2l+1)(2l'+1)} \times\left\langle\frac{Y_m^{l+2}(\hat{R}_0)}{R_0^{l+3}}\cdot\frac{Y_{m'}^{l'+2}(\hat{R})}{R^{l'+3}}\right\rangle\left\langle\rho_0^l Y_m^l(\hat{\rho}_0)\cdot\rho^{l'}Y_{m'}^{l'}(\hat{\rho})\right\rangle. \tag{47}$$

Thereby, we have assumed a decoupling of translational and rotational motion at each level of l. A global coupling is still preserved by the summation over l. The intrinsic correlation function of rotation $\langle\rho_0^l Y_m^l(\hat{\rho}_0)\cdot\rho^{l'}Y_{m'}^{l'}(\hat{\rho})\rangle$ can be identified as the correlation of solid spherical harmonics $\rho^l Y_m^l$. Since $\vec{\rho} = \vec{\delta}_I - \vec{\delta}_S$ and assuming that the special case of $m = \pm l$,

$$\rho^l Y_{\pm l}^l = \text{const.}\cdot(\rho_x \pm i\rho_y)^l = \rho_\pm^l \tag{48}$$

is also representative for all other cases, we can do a binomial expansion of the correlation function of rotation:[12]

$$\begin{aligned}&\left\langle\rho_0^l Y_m^l(\hat{\rho}_0)\cdot\rho^{l'}Y_{m'}^{l'}(\hat{\rho})\right\rangle\\ &= \left\langle\left[(\delta_{I,0} - \delta_{S,0})^l Y_m^l(\hat{\delta}_{I,0} - \hat{\delta}_{S,0})\right]\cdot\left[(\delta_I - \delta_S)^{l'}Y_{m'}^{l'}(\hat{\delta}_I - \hat{\delta}_S)\right]\right\rangle\\ &= \sum_{\lambda=0}^{l}\sum_{\lambda'=0}^{l'}(-1)^{\lambda+\lambda'}\binom{l}{\lambda}\binom{l'}{\lambda'}\delta_I^\lambda\delta_I^{\lambda'}\delta_S^{l-\lambda}\delta_S^{l'-\lambda'}\\ &\quad\times\left\langle Y_\mu^\lambda(\hat{\delta}_{I,0})\cdot Y_{\mu'}^{\lambda'}(\hat{\delta}_I)\right\rangle\left\langle Y_{m-\mu}^{l-\lambda}(\hat{\delta}_{S,0})\cdot Y_{m'-\mu'}^{l'-\lambda'}(\hat{\delta}_S)\right\rangle.\end{aligned} \tag{49}$$

On the right hand side of the last equation we have performed a decoupling of the spins I and S, a mathematical simplification assuming independent rotation of the molecules carrying the spins. Now, we can compute the correlation functions for each individual spin using again the propagator formalism:

$$\left\langle Y_\mu^\lambda(\Omega_0)\cdot Y_\mu^\lambda(\Omega)\right\rangle = \int d\Omega_0\,\frac{1}{4\pi}\int d\Omega\; Y_\mu^\lambda(\Omega_0) \times P(\Omega, t|\Omega_0; t=0)Y_\mu^\lambda(\Omega), \tag{50}$$

$$P(\Omega, t\mid\Omega_0; t=0) = \sum_{\lambda,\mu} e^{-\lambda(\lambda+1)[\phi(t)-\phi(0)]^2}Y_\mu^\lambda(\Omega)Y_\mu^{\lambda*}(\Omega_0) \tag{51}$$

with the angular displacement $\langle[\phi(t) - \phi(0)]^2\rangle = \int_0^t d\tau\,(t-\tau)\langle\vec{\omega}(0)\cdot\vec{\omega}(\tau)\rangle$, derived from the angular velocity $\vec{\omega}(t)$.[54] Inserting the propagator and exploiting the orthogonality of the spherical harmonics, as already shown in Eq. (16), we get for the correlation function

$$\left\langle Y_\mu^\lambda(\delta_{I,0})\cdot Y_{\mu'}^{\lambda'}(\delta_{I,t})\right\rangle = \frac{1}{4\pi}\delta_{\lambda,\lambda'}\delta_{\mu,\mu'}e^{-\lambda(\lambda+1)[\phi(t)-\phi(0)]^2}, \tag{52}$$

which implies $\mu = \mu'$ and $\lambda = \lambda'$ further resulting in $l = l'$, reducing the double sum in Eq. (47) as well as in Eq. (49). Thus, we finally get for the correlation function of rotation:

This article is copyrighted as indicated in the article. Reuse of AIP content is subject to the terms at: http://scitation.aip.org/termsconditions. Downloaded to IP: 131.130.40.8 On: Mon, 12 May 2014 08:38:19

$$\left\langle \rho_0^l Y_m^l(\hat{\rho}_0) \cdot \rho^l Y_m^l(\hat{\rho}) \right\rangle = \sum_{\lambda} \left(\frac{l!}{\lambda!(l-\lambda)!} \right)^2 \delta_I^{2\lambda} \delta_S^{2(l-\lambda)} e^{-\lambda(\lambda+1)[\phi_I(t)-\phi_I(0)]^2} e^{-(l-\lambda)(l-\lambda+1)[\phi_S(t)-\phi_S(0)]^2}. \tag{53}$$

Combining rotational and translational motion of the spins in $G(t)$ yields for the spectral density $J(\omega)$,

$$J(\omega) = K_{IS} \cdot \frac{N}{V} \sum_l \frac{(l+1)(l+2)(2l+3)(2l+1)!}{6} \sum_{\lambda=0}^{l} \left(\frac{l!}{\lambda!(l-\lambda)!} \right)^2 \delta_I^{2\lambda} \delta_S^{2(l-\lambda)}$$
$$\times \int_0^{R_{up}} dR_0 \; g(R_0) \frac{1}{R_0^{l+1}} \int_0^{\infty} dR \; \frac{1}{R^{l+1}} \int_0^{\infty} dk \; k^2 j_{l+2}(kR) j_{l+2}(kR_0) \mathcal{F}[K(\vec{k}, l, t)] \tag{54}$$

with the kernel

$$K(\vec{k}, l, t) = e^{-\frac{k^2}{6}(\vec{R}_{ij}(t)-\vec{R}_{ij}(0))^2 \cdot t - \frac{\lambda(\lambda+1)}{4}(\phi_I(t)-\phi_I(0))^2 + \frac{(l-\lambda)(l-\lambda+1)}{4}(\phi_S(t)-\phi_S(0))^2}. \tag{55}$$

Neglecting ro-translational coupling, i.e., setting $l = \lambda = 0$, the last two expressions simplify to the case of pure translation (Eqs. (17) and (21)).

In the asymptotic case we insert

$$(\vec{R}_{ij}(t) - \vec{R}_{ij}(0))^2 \to 6 D_T t, \tag{56}$$

$$(\phi_I(t) - \phi_I(0))^2 \to 4 D_{R,I} t, \tag{57}$$

$$(\phi_S(t) - \phi_S(0))^2 \to 4 D_{R,S} t, \tag{58}$$

into Eq. (55) and we get the following Fourier transform for the kernel in case of simple diffusion:

$$\mathcal{F}[K(\vec{k}, l, t)] = \frac{D_T k^2 + \lambda(\lambda+1) D_{R,I} + (l-\lambda)(l-\lambda+1) D_{R,S}}{(D_T k^2 + \lambda(\lambda+1) D_{R,I} + (l-\lambda)(l-\lambda+1) D_{R,S})^2 + \omega^2}. \tag{59}$$

In the next case, we address diffusion in ionic liquids. Now, our kernel looks like

$$\mathcal{F}[K(\vec{k}, l, t)] = \frac{D_T k^2 + \lambda(\lambda+1) D_{R,I} + (l-\lambda)(l-\lambda+1) D_{R,S}}{(D_T k^2 + \lambda(\lambda+1) D_{R,I} + (l-\lambda)(l-\lambda+1) D_{R,S})^2 + \omega^2} \cdot e^{-D_T k^2 \tau_0}. \tag{60}$$

In the last case, we consider jump-diffusion as introduced by Ivanov and thus, emerges the following kernel with two possible τ_{jump} (τ_T and τ_R):[51,52]

$$\mathcal{F}[K(\vec{k}, l, t)] = \frac{\frac{D_T k^2}{1+D_T k^2 \tau_T} + \frac{\lambda(\lambda+1) D_{R,I}}{1+\lambda(\lambda+1) D_{R,I} \tau_R} + \frac{(l-\lambda)(l-\lambda+1) D_{R,S}}{1+(l-\lambda)(l-\lambda+1) D_{R,S} \tau_R}}{\left(\frac{D_T k^2}{1+D_T k^2 \tau_T} + \frac{\lambda(\lambda+1) D_{R,I}}{1+\lambda(\lambda+1) D_{R,I} \tau_R} + \frac{(l-\lambda)(l-\lambda+1) D_{R,S}}{1+(l-\lambda)(l-\lambda+1) D_{R,S} \tau_R} \right)^2 + \omega^2}. \tag{61}$$

The variations of all our model theories are summarised in Table I. They differ with respect to the kernel indicated by the use of the equation number. The type of pair correlation function used is described in literal terms.

D. Supermolecular aggregates

In case of strong intermolecular interactions the particles may form aggregates which survive on a time scale, which is long compared to the time scale of the dynamical processes driving intermolecular relaxation. In the latter case, the centre of mass distance of the two spin particles remains constant during the relaxation process and the vector $\vec{R}$ becomes equal to the vector $\vec{\rho} = \vec{\delta}_I - \vec{\delta}_S$, where $\vec{\delta}_I$ and $\vec{\delta}_S$ now refer to the centre of mass of the aggregate. Because ρ is constant and the dipole-dipole tensor solely results from rotational dynamics, the time correlation function in Eq. (9) simplifies to

$$G(t) = \frac{1}{\rho^6} \langle Y_{2m}^l(\Omega_0) Y_{2m}^l(\Omega_0) \rangle \tag{62}$$

in which we may introduce any model for the rotational propagator. Thus, in the strong-coupling limit Eq. (10) reduces the well-known r^{-6} dependent intramolecular spectral density, for example, exploited in biomolecular structure determinations.[3] In case of the intermolecular NOE the distance dependence is much more complex as shown later on.

III. SIMULATION

A. The model system

In order to have independent data for a critical assessment of the various versions of our model theory that goes

This article is copyrighted as indicated in the article. Reuse of AIP content is subject to the terms at: http://scitation.aip.org/termsconditions. Downloaded to IP: 131.130.40.8 On: Mon, 12 May 2014 08:38:19

TABLE I. Summary of model theories studied.

No.	Distance distribution $g(R_0)$	Pure translation	Ro-translational coupling	Input parameters	Kernel Eq.
I	Simple step function	Simple diffusion	...	$D_{T,I}, D_{T,S}, b$	(23)
II	Step function preserving ion density	Simple diffusion	...	$D_{T,I}, D_{T,S}, b, d$	(23)
III	$g^{+-}_{000}(r)$	Simple diffusion	...	$D_{T,I}, D_{T,S}$	(23)
IV	$g^{+-}_{000}(r)$	Diffusion in ILs	...	$D_{T,I}, D_{T,S}, \tau_0 = 1.58 \times 10^{-9}$s	(36)
V	$g^{+-}_{000}(r)$	Jump diffusion	...	$D_{T,I}, D_{T,S}, \tau_{jump} = 1.26 \times 10^{-8}$s	(39)+(40)
VI	$g^{+-}_{000}(r)$	Lattice diffusion	...	$D_{T,I}, D_{T,S}, \tau_{lat} = 1.58 \times 10^{-8}$s	(39)+(41)
VII	Step function preserving ion density	...	Simple diffusion	$D_{T,I}, D_{T,S}, D_{R,I}, D_{R,S}, \delta_I, \delta_S, b, d$	(59)
VIII	$g^{+-}_{000}(r)$	...	Simple diffusion	$D_{T,I}, D_{T,S}, D_{R,I}, D_{R,S}, \delta_I, \delta_S$	(59)
IX	$g^{+-}_{000}(r)$	...	Diffusion in ILs	$D_{T,I}, D_{T,S}, D_{R,I}, D_{R,S}, \delta_I, \delta_S, \tau_0 = 1 \times 10^{-9}$s	(60)
X	$g^{+-}_{000}(r)$	...	Jump diffusion	$D_{T,I}, D_{T,S}, D_{R,I}, D_{R,S}, \delta_I, \delta_S, \tau_{jump} = 3.16 \times 10^{-8}$s	(61)
A	Simulation data	T_{ij}	...		
B	Simulation data	...	T_{ij}		
Structure parameters (Å):			$b = 3.15, d = 4.7, \delta_I = 1.78, \delta_{I,max} = 2.15, \delta_S = 1.39, g^{+-}_{000}(R_0)$		
Translational single particle diffusion (Å^2 s^{-1}):			$D_{T,I} = 12.3 \times 10^8, D_{T,S} = 5.1 \times 10^8$		
Rotational single particle diffusion (s^{-1}):			$D_{R,I} = 1.35 \times 10^8, D_{R,S} = 3.4 \times 10^8$		

beyond a comparison with the global NOE data obtained by experiment, we have performed an analysis of trajectories from an extensive simulation of the ionic liquid 1-ethyl-3-methylimidazolium tetrafluoroborate [EMIM][BF_4] shown in Fig. 3. Due to their unique solvent properties, imidazolium salts belong to the most widely used ionic liquids.[23,24]

Because the most informative experimental NOE data refer to 1-butyl-3-methylimidazolium tetrafluoroborate [BMIM][BF_4], comprising cation-anion interactions with ^{19}F atoms of the tetrafluoroborate anion[39] and cation-cation interactions with hydrogens of neighbouring cations,[40] we have recently applied a simple version of our model theory to the latter salt.[15] In attempting to obtain a more general picture of dynamical processes in ionic liquids, and also including their relation to solvation dynamics of Coumarin-153 (C153),[37] we replace [BMIM]$^+$ by [EMIM]$^+$. This should shift the time scale of the relevant dynamical processes to shorter times, which better meets the time window imposed by the limited length of the simulation runs.

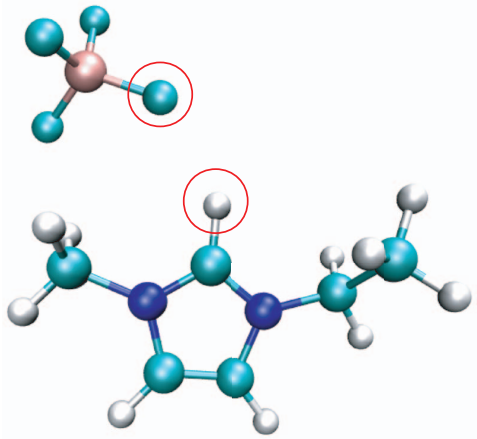

FIG. 3. An ion pair of the ionic liquid 1-ethyl-3-methylimidazolium tetrafluoroborate ([EMIM][BF_4]) with the atoms of interest (^{1}H and ^{19}F) marked by a red circle.

The simulation cell was a cubic box with a length of 64.4 Å at 300 K. The system contained 1000 [EMIM][BF_4] pairs, corresponding to an ion density of $(N^+/V) = (N^-/V) = 0.00374$ Å^{-3}, which reproduces the experimental mass density of the liquid at 300 K of 1.24 g cm^{-3}. For enabling a comparison with solvation spectroscopy for the same simulation run (not done here) the simulation box involved also one coumarin C153 molecule, whose effect is neglected here. For details please refer to our recent work.[37]

B. Evaluation of the spectral density function

The propagator used in the model theory tries to mimic the Liouville-operator in molecular dynamics simulations. The Liouville operator describes the time evolution of an element of the T-tensor during simulation

$$T^l_{2m}(\vec{R}) = e^{\mathcal{L}t} T^l_{2m}(\vec{R}_0). \tag{63}$$

Model theories replace the "exact" Liouville operator by an approximate propagator $P(\vec{R}, t|\vec{R}_0; t = 0)$.

By contrast, $J(\omega)$ can also be calculated from simulation data based on Eqs. (4)–(7), where the Liouville equation is solved directly by numerical propagation.

First, the timeseries of all unique elements of the dipole-dipole tensor were obtained for all 10^6 cation-anion-pairs.

Second, spectral density functions were calculated for each element of the dipole-dipole tensor independently, whereas the total spectral density function for one pair $J_{ij}(\omega)$ was an average over the spectral density functions of all elements of the corresponding dipole-dipole tensor.[55] The spectral density function for one pair was labeled with the initial distance of the two spins, and the average spectral density function for distance intervals of 1 Å could be calculated. Of course, this average contribution representing the interaction of one pair was multiplied by either the exact pair distribution for small distances, or the mean number density for distances larger than half of the simulation box length.

Third, for studying the spatial range of the spectral density function $J(\omega)$ a cumulative summation of all pair

This article is copyrighted as indicated in the article. Reuse of AIP content is subject to the terms at: http://scitation.aip.org/termsconditions. Downloaded to IP: 131.130.40.8 On: Mon, 12 May 2014 08:38:19

contributions $J_{ij}(\omega)$ up to an upper limit R_{up} was done. This corresponds to the integration over the pair correlation function up to R_{up} in our model theory. Of course, $J_{ij}(\omega)$ decreases with increasing distance R_0, but at the same time the number of pairs increases. This competition of decrease and increase makes the NOE long-ranged. It needs quite a long distance R_{up} to make $J_{ij}(\omega)$ so small that the summation converges.

IV. RESULTS AND DISCUSSION

A. Simulation data and implementation of model theories

A typical spectral density function $J(\omega)$ starts from its static value $J(0)$, followed by an initial segment, known as "extreme narrowing," where the frequency dependence is weak. Afterwards, $J(\omega)$ strongly, monotonically declines, until it dwindles down to zero at high frequencies. The shape of the "complete" function is displayed later in Fig. 9 in the context of results for one of our models.

In contrast, our simulation data restricts the frequency window in the computation of $J(\omega)$ to values above 2×10^8 s^{-1}, which falls into the high frequency segment of the curve. This is due to our finite simulation length. In Fig. 4, we present the total spectral density functions $J(\omega)$ for pure translation (A) in green as well as ro-translational coupling (B) in red from our simulations. Thereby, spin pairs with a distance $R_{up}^{max} = 100$ Å are contributing. The data stem from 4 independent analyses of a 30 ns time window. The averaged curve is given by the black line in either the red or green area.

It is important to note that for typical spectrometer frequencies of several hundred megahertz, in our case exemplified by data for 400 MHz, the computational results do not cover the frequency triple (i.e., $J(\omega_I - \omega_S)$, $J(\omega_I)$, $J(\omega_I + \omega_S)$) (black vertical lines in Fig. 4) picked up by the NOE. For an 800 MHz Proton spectrometer the frequency triplet (red, dashed lines in Fig. 4) is shifted to higher frequencies and thus can be used to calculate the NOE. Please note that this situation cannot be achieved in simulations of the homonuclear NOE, where $J(\omega_I - \omega_S)$ turns into $J(0)$.

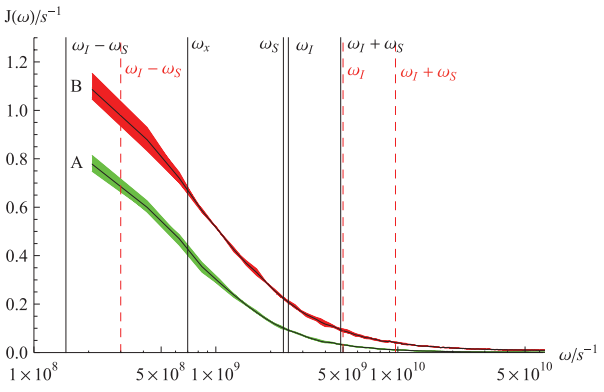

FIG. 4. The green area depicts 4 different spectral density functions $J(\omega)$ for purely translational motion of the spins I and S (a) up to $R_{up}^{max} = 100$ Å with their average in black. The red area refers to the ro-translational coupling of the spins (b). The average of the curves is given in black as well.

In Fig. 4, the frequency dependence of both spectral density functions (A) and (B) look alike but with an off-set for ro-translational coupling. This off-set can be found likewise in all variants of our model theory, appearing in the subsequent figures. An overview of the variants, labeled according to Roman numbers (I–X), and their respective parameters can be found in Table I. Fig. 5 gives an overview of pair correlation functions used in our model theories. The simulated centre-to-centre (000) cation-anion (+−) radial distribution function $g_{000}^{+-}(R_0)$ is shown in black. For a more detailed explanation of the indices used, please refer to another work.[56,57] Strong charge ordering[23,24] leads to deviations from a uniform distribution up to a distance of about 30 Å, as revealed by four detectable coordination shells,which are given in green. The onset of the pair distribution function is located at a distance b of 3.15 Å. The same onset was used for a step function given in red. In order to ensure, that the step function preserves particle density, its onset of $d = 4.7$ Å was calculated from the equality

$$\int_d^{30} dR_0\ R_0^2 = \int_0^{30} dR_0\ R_0^2\ g_{000}^{+-}(R_0). \tag{64}$$

Under the simplifying assumptions, that the pair correlation function is given by a step function and the pure translational propagator is given by simple diffusion, we even get a completely analytic expression for $J(\omega)$,

$$J(\omega) = K_{IS} \cdot \frac{N}{V} \cdot \int_0^{\infty} dk \left(\frac{j_1(kd)}{d} - \frac{j_1(kR_{up})}{R_{up}} \right) \cdot \left(\frac{j_1(kb)}{b} \right) \cdot \frac{k^2 D_T}{(k^2 D_T)^2 + \omega^2}. \tag{65}$$

Here, the second term in brackets can be identified as the propagator with its onset at a distance b, which coincides with the onset of the radial distribution function $g_{000}^{+-}(R_0)$ (Fig. 5). The first term in brackets refers to the step function, having its onset at a distance d and ending at R_{up}. Upon further simplification, $b = d$ and $R_{up} = \infty$ one gets the original formula of Abragam (Eq. (114) of Ref. 8), for which an analytical solution can be found in case of $\omega = 0$. Since for more elaborate models of $J(\omega)$ only numerical expressions can be obtained, we implemented them in the program *mathematica*. Furthermore, we found out that the integration over k – representing translation – can be limited to 20 Å^{-1} and the summation over l – representing the ro-translational coupling – can be restricted to $l = 8$.

B. From the step function to the radial pair distribution function

In our previous work,[15] we limited our results by solely using the step function as a pair correlation function. In this section, we compare the influence of the replacement of the step function by the radial distribution function $g_{000}^{+-}(R_0)$. Fries and Belorizky already used a pair correlation function $g(R_0)$ in their calculations, although it was taken from simple Lennard-Jones liquids.[58] Bagno *et al.* studied the influence of several analytical distribution functions and their influence on the spectral density function $J(\omega)$.[59] In our calculations we use

This article is copyrighted as indicated in the article. Reuse of AIP content is subject to the terms at: http://scitation.aip.org/termsconditions. Downloaded to IP: 131.130.40.8 On: Mon, 12 May 2014 08:38:19

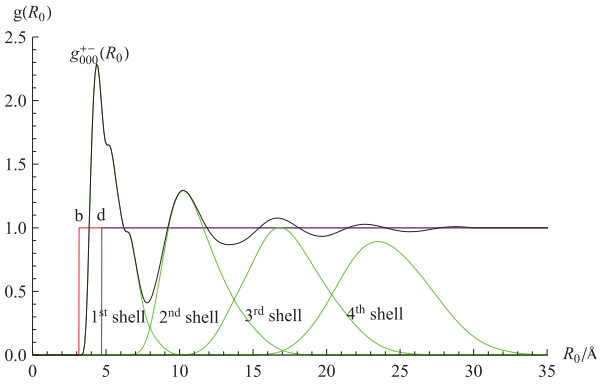

FIG. 5. Centre-of-mass radial pair distribution function $g^{+-}_{000}(R_0)$ of [EMIM][BF_4] is given in black. For distances greater than 30 Å, $g^{+-}_{000}(R_0)$ can be set equal to unity. The shells contributing to $g^{+-}_{000}(R_0)$ are displayed in green. The step function with the same onset as the pair distribution function at $b = 3.15$ Å is displayed in red, whereas the step function in blue preserves the same particle density as $g^{+-}_{000}(R_0)$ with the onset at a distance $d = 4.7$ Å.

the radial distribution function $g^{+-}_{000}(R_0)$, directly generated from the simulation data of [EMIM][BF_4], which consists of anisotropic ions. In Fig. 6, the spectral density function $J(\omega)$ from simulation data (A) for purely translational motion of the spins I and S, is given in green. Thereby, spin pairs with a distance R^{max}_{up} up to 100 Å were contributing. The curve shows a distinct decline from $2 \times 10^8 - 5 \times 10^9$ s^{-1} and only marginal values of $J(\omega)$ from $5 \times 10^9 - 5 \times 10^{10}$ s^{-1}.

The simplest model theory uses the step function for the calculation of $J(\omega)$. The red curve in Fig. 6 represents model II. There, the preservation of particle density was ensured by choosing the onset of the step function as d and b for the propagator (see Table I). One can see that the asymptotic values at high frequencies show the same behaviour as our simulation data (A) but for frequencies lower than 5×10^9 they are much too low. To improve the beginning of the

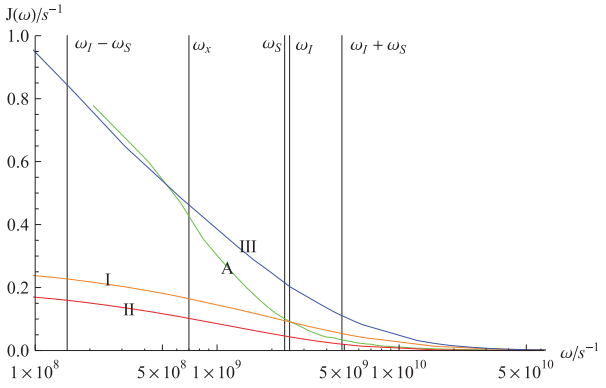

FIG. 6. Various spectral density functions $J(\omega)$ are shown for purely translational motion of the spins I and S. Simulation data (A) is given in green. Red represents the use of the step function for $J(\omega)$, while preserving the particle density (model II), whereas orange (model I) uses the step function with the same onset as given in the pair distribution function (model III), depicted in blue. All models (I, II, and III) use a kernel containing the solution of the diffusion equation.

curve, we neglected particle density and put the same value for the propagator and the onset of the step function ($b = d$), which equals the onset of $g^{+-}_{000}(R_0)$. The result is depicted in orange (model I). Although, the beginning of the curve is better than before, the simulation data (A) and the model theory (I) differ considerably with respect to curvature. Next, we inserted $g^{+-}_{000}(R_0)$ in our model theory, the outcome (model III) is given in blue. This approach provides us the correct onset and improves the curvature as well, but for frequencies higher than 5×10^8 s^{-1} the absolute values still significantly deviate from our simulation data (A). Nevertheless, we can order the models (II, I, and III) according to their improvement in comparison to simulation data. This ordering of models (II, I, and III) corresponds to the integral of the respective pair correlation functions up to 7–8 Å (see Fig. 5). In other words, a larger contribution of the pair correlation function goes along with a steady rise of the onset of the spectral density function $J(\omega)$ at low frequencies. Although, upgrading the pair correlation function improves $J(\omega)$ at low frequencies it still misses the right curvature, which is influenced by pair dynamics as reflected by the kernel. Up to now, we only use the kernel being a solution of the diffusion equation, i.e., simple diffusion (see Table I). In the following, we will study a more complex dynamics.

C. Complex translational pair dynamics

To go beyond simple diffusion with $g^{+-}_{000}(R_0)$ as a pair correlation function, we manipulate the kernel. In Fig. 7, we again present in green the simulation data for purely translational motion (A). For a better comparison of the effects of the manipulated kernel, we give the result of model III in blue as well. First, we inserted non-Gaussian diffusion models in the kernel. This can be regarded as an effective inclusion of higher terms of the cumulant expansion in k-space. Therefore, we studied Eq. (39) in combination with Eq. (40) to study jump diffusion and the resulting orange curve (model V) is shown in Fig. 7. A close fit to simulation data (A) was only possible in the high frequency regime resulting in a τ_{jump} of 1.26×10^{-8}s and extremely high values for $J(\omega)$ at lower frequencies. Furthermore, for this particular τ_{jump} we arrive at totally unreasonable jump lengths. Next, we studied lattice diffusion and combined Eqs. (39) and (41). This model (VI) is shown in grey. We found a τ_{lat} of 1.58×10^{-8} s for lattice diffusion, which is again very unrealistic.

Second, we use the result of Eq. (36) from Sec. II B 2 b as a kernel, which allows us to observe the influence of diffusion in ionic liquids on $J(\omega)$. This is shown in the magenta curve (model IV) in Fig. 7. The curve shows good agreement with simulation data for more than one decade in frequency, only the onset is a bit off the mark. Even more important is the fit result of $\tau_0 = 1.58 \times 10^{-9}$ s, which is comparable to the $\tau_0 = 0.66 \times 10^{-9}$ s gained from the fit to our simulated pair displacement. Bearing in mind that we are fitting a model theory to a simulated spectral density function and the off-centre effect has yet not been considered the consistency of the respective τ_0 values is remarkable.

This article is copyrighted as indicated in the article. Reuse of AIP content is subject to the terms at: http://scitation.aip.org/termsconditions. Downloaded to IP: 131.130.40.8 On: Mon, 12 May 2014 08:38:19

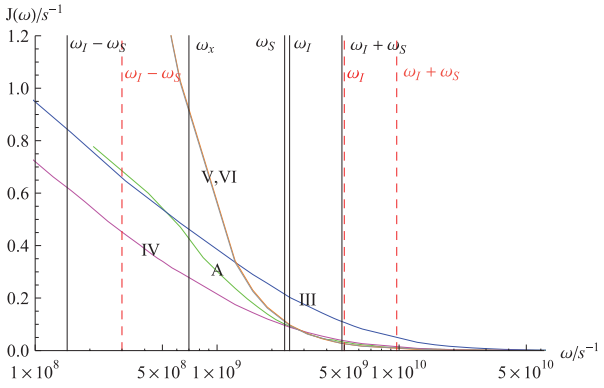

FIG. 7. The influence of an enhanced kernel on the spectral density function $J(\omega)$ is given here. Simulation data (A) is shown in green. The use of the pair distribution function for $J(\omega)$ with simple diffusion (model III) is a representative for the simple kernel and is given in blue. The utilisation of jump diffusion with $\tau_{jump} = 1.26 \times 10^{-8}$ s in combination with the pair distribution function for $J(\omega)$ (model V) is represented in orange. The grey curve for $J(\omega)$ arises from the application of lattice diffusion ($\tau_{lat} = 1.58 \times 10^{-8}$ s) and the use of the pair distribution function (model VI). Due to the resolution of the figure, the graphs of models V and VI coincide. Magenta shows the result for a kernel using diffusion in ionic liquids with $\tau_0 = 1.58 \times 10^{-9}$ s and $g_{000}^{+-}(R_0)$ (model IV).

D. Ro-translational coupling

As a next step, we calculate $J(\omega)$ with l up to 8 to include the ro-translational coupling and off-centre effect of the spins I and S. Higher l did not have a noteworthy contribution to $J(\omega)$ and were thus neglected. Simulation data (B) is given in red in Fig. 8. The result for the step function is not given here, since it is poor and not worth showing. All further results of our model theories use $g_{000}^{+-}(R_0)$ as a pair correlation function.

To investigate the influence of the displacement of ^{1}H from the centre of mass, the displacement of ^{19}F was kept fixed at a distance of 1.39 Å. The average displacement of ^{1}H, deduced from simulation data, of 1.78 Å for $[EMIM]^+$ (model VIII) is shown in purple in Fig. 8. The data for maximum displacement of ^{1}H of 2.15 Å is not given here, since its curve is just shifted to higher values. It is obvious, that the displacement of the spins I and S from their centre of mass shifts $J(\omega)$, but it still provides an insufficient curvature as dynamics is still restricted to simple diffusion. Therefore, we need a more elaborate kernel, as already mentioned above.

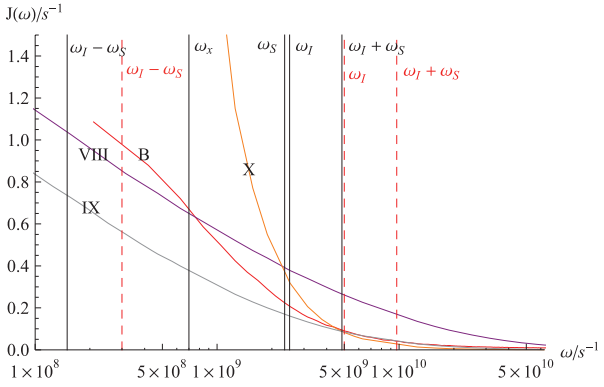

FIG. 8. Various spectral density functions $J(\omega)$ are shown for the ro-translational coupling of the spins I and S. Simulation data (B) is given in red. The use of the pair correlation function $g_{000}^{+-}(R_0)$ with an average displacement of 1.78 Å for $[EMIM]^+$ as well as simple diffusion (model VIII) is given in purple. The grey curve (model IX) includes diffusion in ionic liquids in the kernel (Eq. (60)) with $\tau_0 = 1 \times 10^{-9}$ s as well as $g_{000}^{+-}(R_0)$. The utilisation of jump diffusion with $\tau_{jump} = 3.16 \times 10^{-8}$ s (kernel of Eq. (61)) in combination with $g_{000}^{+-}(R_0)$ on $J(\omega)$ (model X) is represented in orange.

First, we use the kernel of Eq. (61) for the evaluation of Eq. (54). In principle, we are enabled to use two different τ_{jump} (τ_T and τ_R), nevertheless, the best result was achieved by the use of a $\tau_T = \tau_R = \tau_{jump} = 3.16 \times 10^{-8}$ s as visible by the orange curve (model X) in Fig. 8, which is in agreement with simulation data (B) for high frequencies but sucks at low frequencies. Furthermore, in analogy to purely translational motion, we are facing the same problem of a totally unrealistic jump length λ_h.

Inserting the kernel of Eq. (60) in Eq. (54), we investigate the influence of diffusion in ionic liquids as developed in Sec. II B 2 b. The result (model IX) is shown in grey. For a τ_0 of 1×10^{-9} s we observe a good agreement with simulation data (B) for one decade in frequency. This τ_0 is in excellent agreement with the value ($\tau_0 = 0.66 \times 10^{-9}$ s) derived from the direct fit of the pair displacement gained from simulation data (see Sec. II B 2 b). This demonstrates that among all model theories developed here, models (IV and IX) are the ones with the highest consistency with simulation data (A and B).

In general, the inclusion of the off-centre effect shifts all model curves (VII, VIII, IX, and X) to higher values as compared to the purely translational models (II, III, IV, and V), but it does not change its shape. This principal behaviour is in accordance to our simulation data as already shown in Fig. 4.

E. Distance dependence at 5 selected frequencies

To study the distance dependence of the NOE, we restricted the upper limit R_{up} of Eq. (54). Now, we can calculate the contribution to the spectral density function $J(w)$ of all spin pairs with an initial pair distance up to R_{up}. We selected five frequencies of the total spectrum to investigate the distance dependence. For a 400 MHz Proton NMR spectrometer, these are ω_I (2.5×10^9 s^{-1}) and ω_S (2.35×10^9 s^{-1}), the frequencies of the spins I and S, $\omega_I - \omega_S$ (1.5×10^8 s^{-1}) and $\omega_I + \omega_S$ (4.85×10^9 s^{-1}), the difference and sum frequency needed for the calculation of the cross relaxation rate σ_{IS} (Eq. (1)) as well as longitudinal relaxation rate ρ_{II} (Eq. (2)) of the NOESY experiment. Furthermore, an additional frequency ω_x at 7×10^8 s^{-1} was chosen, being placed, where the curves of $J(\omega)$ shift from the steep onset to the flat ending. These frequencies can be identified as the black lines in Figs. 4 and 6–8. For the model theories the zero frequency was calculated as well. In Table II, we give the distance resolved values of the normalised spectral density function

$$J^N(\omega = \omega_i, R_{up}) = J(\omega = \omega_i, R_{up}) / J\left(\omega = \omega_i, R_{up}^{max}\right), \tag{66}$$

where $\omega_i = 0$, $\omega_I - \omega_S$, ω_x, ω_I, ω_S, $\omega_I + \omega_S$. Unfortunately, we could not give results for our simulation data for the difference frequency (400 MHz Proton spectrometer), since limited

This article is copyrighted as indicated in the article. Reuse of AIP content is subject to the terms at: http://scitation.aip.org/termsconditions. Downloaded to IP: 131.130.40.8 On: Mon, 12 May 2014 08:38:19

TABLE II. Distance resolved values of the normalised spectral density function $J^N(\omega = \omega_i, R_{up})$ with $\omega_i = 0, \omega_I - \omega_S, \omega_x, \omega_I, \omega_S, \omega_I + \omega_S$, for various models and simulation data. The rows labeled $R_{up} = 100$ Å give the absolute values in s^{-1} at this distance. The upper half of the table addresses purely translational motion of the spins I and S, whereas the lower half gives the results for the ro-translational coupling of the spins.

Pure translation

Model	II						III						IV						A				V					
R_{up}(Å)	0	$\omega_I - \omega_S$	ω_x	ω_S	ω_I	$\omega_I + \omega_S$	0	$\omega_I - \omega_S$	ω_x	ω_S	ω_I	$\omega_I + \omega_S$	0	$\omega_I - \omega_S$	ω_x	ω_S	ω_I	$\omega_I + \omega_S$	ω_x	ω_S	ω_I	$\omega_I + \omega_S$	0	$\omega_I - \omega_S$	ω_x	ω_S	ω_I	$\omega_I + \omega_S$
5	0.05	0.07	0.09	0.15	0.15	0.21	0.12	0.23	0.37	0.52	0.53	0.61	0.07	0.16	0.26	0.38	0.39	0.45	0.09	0.10	0.11	0.10	0.39	0.50	0.59	0.62	0.62	0.63
6	0.20	0.25	0.35	0.51	0.52	0.66	0.19	0.36	0.54	0.75	0.76	0.83	0.12	0.25	0.41	0.59	0.61	0.69	0.20	0.18	0.20	0.21	0.53	0.68	0.78	0.81	0.81	0.82
7	0.31	0.39	0.53	0.73	0.74	0.88	0.23	0.43	0.64	0.85	0.87	0.92	0.15	0.31	0.51	0.71	0.72	0.81	0.29	0.26	0.28	0.31	0.59	0.76	0.85	0.88	0.88	0.88
8	0.40	0.50	0.66	0.85	0.87	0.97	0.25	0.47	0.69	0.89	0.90	0.95	0.17	0.35	0.55	0.76	0.77	0.86	0.31	0.28	0.29	0.33	0.62	0.80	0.88	0.90	0.90	0.91
9	0.52	0.59	0.75	0.93	0.94	1.0	0.27	0.50	0.73	0.93	0.94	0.97	0.19	0.39	0.61	0.81	0.82	0.89	0.36	0.33	0.34	0.37	0.64	0.81	0.90	0.92	0.92	0.93
10	0.57	0.65	0.82	0.97	0.97	1.0	0.31	0.56	0.79	0.95	0.96	0.99	0.22	0.45	0.69	0.87	0.88	0.93	0.44	0.41	0.41	0.45	0.67	0.85	0.92	0.94	0.94	0.95
15	0.70	0.85	0.97	1.0	1.0	1.0	0.43	0.75	0.95	0.99	0.99	1.0	0.35	0.67	0.90	0.99	0.99	0.99	0.74	0.71	0.71	0.75	0.76	0.93	0.98	0.99	0.99	0.99
20	0.79	0.93	1.0	1.0	1.0	1.0	0.52	0.86	0.99	1.0	1.0	1.0	0.45	0.81	0.98	1.0	1.0	1.0	0.87	0.84	0.84	0.87	0.81	0.97	0.99	1.0	1.0	1.0
25	0.84	0.97	1.0	1.0	1.0	1.0	0.59	0.91	1.0	1.0	1.0	1.0	0.52	0.89	0.98	1.0	1.0	1.0	0.97	0.95	0.94	0.98	0.84	0.98	1.0	1.0	1.0	1.0
30	0.88	0.99	1.0	1.0	1.0	1.0	0.64	0.95	1.0	1.0	1.0	1.0	0.59	0.93	1.0	1.0	1.0	1.0	1.0	1.0	0.99	1.0	0.86	0.99	1.0	1.0	1.0	1.0
R_{up}=100	0.21	0.16	0.10	0.05	0.04	0.02	1.71	0.84	0.46	0.21	0.20	0.11	1.48	0.62	0.28	0.10	0.09	0.04	0.41	0.10	0.09	0.03	4.61	3.15	0.90	0.11	0.10	0.03

Ro-translational coupling

Model	VII						VIII						IX						B				X					
R_{up}(Å)	0	$\omega_I - \omega_S$	ω_x	ω_S	ω_I	$\omega_I + \omega_S$	0	$\omega_I - \omega_S$	ω_x	ω_S	ω_I	$\omega_I + \omega_S$	0	$\omega_I - \omega_S$	ω_x	ω_S	ω_I	$\omega_I + \omega_S$	ω_x	ω_S	ω_I	$\omega_I + \omega_S$	0	$\omega_I - \omega_S$	ω_x	ω_S	ω_I	$\omega_I + \omega_S$
5	0.08	0.10	0.13	0.19	0.19	0.24	0.18	0.33	0.47	0.61	0.62	0.69	0.10	0.20	0.31	0.43	0.44	0.51	0.08	0.10	0.10	0.09	0.64	0.73	0.82	0.84	0.84	0.84
6	0.27	0.33	0.43	0.58	0.59	0.69	0.26	0.47	0.64	0.81	0.82	0.88	0.16	0.31	0.48	0.65	0.66	0.74	0.18	0.16	0.17	0.20	0.78	0.87	0.93	0.94	0.94	0.95
7	0.39	0.47	0.61	0.78	0.79	0.88	0.30	0.54	0.73	0.89	0.90	0.94	0.19	0.38	0.58	0.76	0.77	0.85	0.28	0.25	0.27	0.29	0.83	0.91	0.96	0.97	0.97	0.97
8	0.47	0.58	0.72	0.88	0.89	0.95	0.32	0.57	0.76	0.92	0.93	0.96	0.21	0.41	0.63	0.81	0.82	0.89	0.32	0.28	0.29	0.32	0.84	0.93	0.97	0.98	0.98	0.98
9	0.54	0.66	0.80	0.94	0.95	0.98	0.34	0.60	0.80	0.95	0.95	0.97	0.23	0.45	0.67	0.85	0.86	0.92	0.37	0.33	0.35	0.37	0.86	0.94	0.98	0.98	0.98	0.98
10	0.59	0.71	0.86	0.97	0.97	0.99	0.37	0.65	0.85	0.96	0.97	0.98	0.27	0.52	0.74	0.90	0.91	0.96	0.42	0.39	0.41	0.43	0.88	0.95	0.98	0.99	0.99	0.99
15	0.74	0.88	0.98	1.0	1.0	1.0	0.49	0.81	0.96	0.99	0.99	1.0	0.39	0.72	0.92	0.98	0.98	0.99	0.70	0.71	0.74	0.75	0.92	0.98	1.0	1.0	1.0	1.0
20	0.82	0.94	1.0	1.0	1.0	1.0	0.57	0.90	1.0	1.0	1.0	1.0	0.49	0.84	0.98	0.99	0.99	1.0	0.84	0.85	0.87	0.88	0.94	0.99	1.0	1.0	1.0	1.0
25	0.87	0.98	1.0	1.0	1.0	1.0	0.63	0.94	1.0	1.0	1.0	1.0	0.56	0.90	0.98	1.0	1.0	1.0	0.93	0.94	0.97	0.99	0.95	1.00	1.0	1.0	1.0	1.0
30	0.90	0.99	1.0	1.0	1.0	1.0	0.68	0.97	1.0	1.0	1.0	1.0	0.62	0.94	1.0	1.0	1.0	1.0	0.97	0.99	1.0	1.0	0.96	1.0	1.0	1.0	1.0	1.0
R_{up}=100	0.25	0.20	0.14	0.08	0.08	0.05	1.91	1.01	0.65	0.39	0.38	0.27	1.60	0.74	0.38	0.17	0.16	0.10	0.65	0.23	0.21	0.09	16.81	11.68	2.98	0.37	0.32	0.09

This article is copyrighted as indicated in the article. Reuse of AIP content is subject to the terms at: http://scitation.aip.org/termsconditions. Downloaded to IP: 131.

simulation length excludes the calculation of this frequency as well as the zero frequency.

First, we address the results of pure translational motion of the spins in the upper half of Table II. To give a better insight in the relative values of Table II, we added the absolute values of $J(\omega)$ at $R_{up}^{max} = 100$ Å. Models II (step function and kernel of Eq. (23)), III ($g_{000}^{+-}(R_0)$ and kernel of Eq. (23)) and IV (diffusion in ionic liquids (Eq. (36))) show a distinct long-range behaviour for low frequencies changing to a short-range NOE at high frequencies. This can readily be seen in the pattern of "1.0," in Table II. This pattern also shows that the difference in range between low and high frequencies decreases with increasing complexity in our model theory. At the frequency $(\omega_I + \omega_S)$ the range enhances from approximately 9 Å (model II) via 15 Å (model III) to 20 Å in model IV. For the simulation data (A) the difference in range disappears altogether. It does not reveal any frequency dependence and reaches the full NOE at a distance of approximately 30 Å, which corresponds to the end of the fourth shell of anions around a cation as visible in Fig. 5.

Our model theory for jump diffusion (model V) shows the same pattern of "1.0," as model IV, but the relative values of model V at short distances drastically exceed those of model IV. We can pinpoint the reason for the results of jump diffusion in its kernel (Eq. (40)). Normally, one needs high values of ω to prevail over the term in the denominator concerning the diffusion coefficients (Eq. (23)). For the kernel of jump diffusion (Eq. (40)) smaller values of ω suffice to bring out the behaviour for higher frequencies, since the term concerning the diffusion coefficients is reduced by τ_{jump}. In other words, τ_{jump} can be regarded as a weighting factor, which reduces the influence of the diffusion coefficients and ω gains in importance at lower frequencies. Simultaneously, we loose the spread in distance (R_{up}), because the integrand in k gets shorter in range (Figure not given).

Next, we have a closer look at the lower half of Table II concerning the results of ro-translational coupling of the spins I and S. For a better comparison with purely translational motion we listed the respective model theories one below the other. For each model we observe the same pattern as for purely translational motion. Even more, the respective relative values of the model theories (II and VII, III and VIII, IV and IX) are very close, where the values for ro-translational coupling are slightly higher. For the simulation data (A and B) respective normalised values are almost identical. Only, for the model of jump diffusion (X) the full NOE is shifted to a shorter range of ≈15 Å, which corresponds to the third shell according to Fig. 5. Apart from this exception, the only difference between purely translational motion and ro-translational coupling of the molecules can be found in their absolute values.

F. NOESY relaxation rates and NOE-enhancement

In low viscous solvents, we have fast dynamics and the spectral density function resides in the high frequency domain. Therefore, the triple of frequencies lies in the extreme narrowing limit, i.e., in the initial part of $J(\omega)$ as shown by the purple curve in Fig. 9. The marginal curvature in this region justifies the assumption that the three values of $J(\omega_I - \omega_S)$, $J(\omega_I)$, and $J(\omega_I + \omega_S)$ are approximately equal. In this limiting case Eq. (3) yields an enhancement of 0.5.

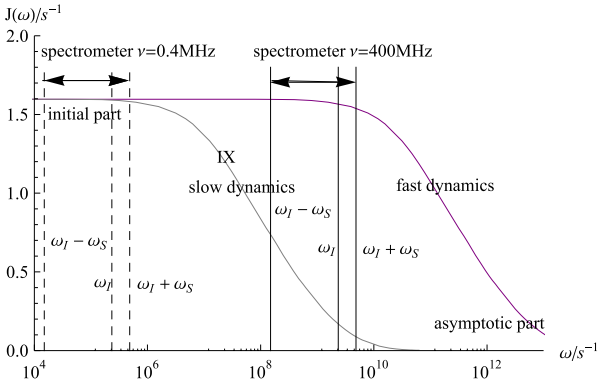

FIG. 9. The frequency dependence of the spectral density functions $J(\omega)$ are shown for model IX, which represent a system of slow dynamics in grey, as well as a model system with fast dynamics in purple.

In high viscous solvents, however, the curvature of $J(\omega)$ comes into action and results in three rather different values for $J(\omega_I - \omega_S)$, $J(\omega_I)$, and $J(\omega_I + \omega_S)$ of descending magnitude. When $J(\omega_I - \omega_S)$ dominates, the denominator of Eq. (3) being of type $\frac{1}{1+x}$ can be approximated by $1 - x$. Consequently, this limiting case leads to an enhancement of

$$f_I\{S\} = \frac{\sigma_{IS}^{NOE}}{\rho_{II}^{NOE}} = -1\left[1 - \frac{3J(\omega_I) + 12J(\omega_I + \omega_S)}{J(\omega_I - \omega_S)}\right] + \mathcal{O}(J^2), \quad (67)$$

lying slightly above −1. Of course, a negative enhancement is only obtainable when having negative cross-relaxation rates σ_{IS}^{NOE} as the longitudinal relaxation rate ρ_{II}^{NOE} is always positive.

However, the fluidity of the sample is only one aspect. Moreover, the choice of the spectrometer determines the position of the triple of frequencies ($J(\omega_I - \omega_S)$, $J(\omega_I)$, and $J(\omega_I + \omega_S)$). Therefore, the actual value of the NOE-enhancement depends on the combination of the solvent viscosity and the spectrometer frequency. Since the enhancement can either be positive or negative, it is even possible to find a combination, where the enhancement is zero. This offers the possibility to get NOE-enhancements of opposite signs from the very same spectral density function by varying the spectrometer frequency. Therefore, we give results for $\nu = 400$ MHz and $\nu = 800$ MHz, respectively. In Figs. 4, 7, and 8, we can identify the triple of frequencies for the 400 MHz spectrometer by the black lines and for the 800 MHz spectrometer by the red, dashed lines.

In Table III, we present the absolute values for the longitudinal, ρ_{II}^{NOE}, and cross-relaxation rates, σ_{IS}^{NOE}, of the NOESY experiment for a 400 MHz Proton spectrometer. We calculated the absolute values according to Eqs. (1) and (2) for the same model theories as already used in Table II and again a variation of R_{up} was used to study the distance dependence. We have also included the NOE-enhancement,

This article is copyrighted as indicated in the article. Reuse of AIP content is subject to the terms at: http://scitation.aip.org/termsconditions. Downloaded to IP: 131.130.40.8 On: Mon, 12 May 2014 08:38:19

TABLE III. The absolute values for the longitudinal and cross-relaxation rates of the NOESY experiment as well as the NOE-enhancement are given distance resolved for various model theories for a 400 MHz Proton spectrometer.

Pure translation												
Model	II			III			IV			V		
R_{up}(Å)	σ_{IS}^{NOE}	ρ_{II}^{NOE}	$f_I\{S\}$	σ_{IS}^{NOE}	ρ_{II}^{NOE}	$f_I\{S\}$	σ_{IS}^{NOE}	ρ_{II}^{NOE}	$f_I\{S\}$	σ_{IS}^{NOE}	ρ_{II}^{NOE}	$f_I\{S\}$
5	0.0014	0.0055	0.248	0.0195	0.0905	0.215	0.0008	0.0307	0.027	−0.1485	0.1876	−0.7918
6	0.0039	0.0187	0.209	0.0236	0.1290	0.183	0.0003	0.0479	0.005	−0.2014	0.2524	−0.7981
7	0.0042	0.0263	0.161	0.0232	0.1475	0.157	−0.0006	0.0577	−0.010	−0.2251	0.2803	−0.8029
8	0.0036	0.0308	0.117	0.0221	0.1542	0.143	−0.0015	0.0621	−0.024	−0.2373	0.2941	−0.8069
9	0.0026	0.0334	0.079	0.0201	0.1602	0.125	−0.0033	0.0668	−0.050	−0.2409	0.2990	−0.8059
10	0.0017	0.0351	0.047	0.0155	0.1674	0.093	−0.0064	0.0736	−0.087	−0.2514	0.3107	−0.8092
15	−0.0015	0.0385	−0.040	0.0007	0.1867	0.004	−0.0187	0.0911	−0.205	−0.2777	0.3399	−0.8172
20	−0.0028	0.0398	−0.071	−0.0070	0.1978	−0.035	−0.0269	0.1003	−0.268	−0.2877	0.3501	−0.8217
25	−0.0034	0.0404	−0.085	−0.0130	0.2020	−0.064	−0.0316	0.1052	−0.300	−0.2929	0.3557	−0.8234
30	−0.0037	0.0407	−0.096	−0.0162	0.2043	−0.079	−0.0345	0.1083	−0.319	−0.2953	0.3580	−0.8248
Ro-translational coupling												
Model	VII			VIII			IX			X		
R_{up}(Å)	σ_{IS}^{NOE}	ρ_{II}^{NOE}	$f_I\{S\}$	σ_{IS}^{NOE}	ρ_{II}^{NOE}	$f_I\{S\}$	σ_{IS}^{NOE}	ρ_{II}^{NOE}	$f_I\{S\}$	σ_{IS}^{NOE}	ρ_{II}^{NOE}	$f_I\{S\}$
5	0.0051	0.0134	0.379	0.0777	0.2144	0.362	0.0123	0.0628	0.1962	−0.8072	0.9760	−0.8271
6	0.0137	0.0403	0.339	0.0945	0.2810	0.336	0.0164	0.0941	0.1739	−0.9635	1.1536	−0.8353
7	0.0161	0.0532	0.303	0.0966	0.3074	0.314	0.0169	0.1101	0.1534	−1.0139	1.2089	−0.8387
8	0.0163	0.0599	0.272	0.0969	0.3169	0.306	0.0164	0.1168	0.1405	−1.0306	1.2269	−0.8399
9	0.0156	0.0635	0.246	0.0950	0.3240	0.293	0.0153	0.1235	0.1239	−1.0453	1.2432	−0.8408
10	0.0148	0.0657	0.225	0.0913	0.3325	0.275	0.0126	0.1322	0.0955	−1.0612	1.2603	−0.8420
15	0.0117	0.0696	0.167	0.0777	0.3537	0.220	−0.0004	0.1521	−0.0028	−1.0979	1.2990	−0.8451
20	0.0103	0.0710	0.146	0.0704	0.3649	0.193	−0.0086	0.1622	−0.0533	−1.1042	1.3049	−0.8462
25	0.0098	0.0716	0.136	0.0648	0.3687	0.176	−0.0133	0.1678	−0.0791	−1.1108	1.3116	−0.8469
30	0.0095	0.0718	0.132	0.0620	0.3705	0.167	−0.0168	0.1706	−0.0982	−1.1146	1.3156	−0.8472

already defined in Eq. (3). The combination of the specific parameters, applied in our model theories to describe [EMIM][BF_4] (see Table I), with a 400 MHz Proton spectrometer fortuitously results in values of around zero for the NOE-enhancement. Of course the longitudinal relaxation rate ρ_{II}^{NOE} is always positive. Therefore, the fluctuations around zero are caused by the sensitivity of the cross-relaxation rate σ_{IS}^{NOE}. As σ_{IS}^{NOE} represents the balance between $6J(\omega_I + \omega_S)$ and $-J(\omega_I - \omega_S)$ it is much more sensitive than the spectral density function $J(\omega)$ itself. In fact it is a measure of the curvature of $J(\omega)$. For small curvature (models II and VII) $6J(\omega_I + \omega_S)$ overrides $-J(\omega_I - \omega_S)$ resulting in a positive enhancement. For large curvature (jump diffusion – models V and X) $-J(\omega_I - \omega_S)$ is the dominating term in σ_{IS}^{NOE} and ρ_{II}^{NOE} and therefore, the enhancement is strongly negative. Due to the outmost dominion of $-J(\omega_I - \omega_S)$ the consistency in the enhancement for models V and X in Table III is an artefact. For a medium curvature (models III and IV, VIII, and IX), we observe a change in sign within the distance dependence. Although models III and IV as well as models VIII and IX are depicted nearly parallel for low frequencies in Figs. 7 and 8, the change in sign occurs at different distances. This can be ascribed to the term $e^{-D_T k^2 \tau_0}$, the solely difference in the respective kernels, which dampens the spectral density functions of models IV and IX, resulting in an earlier dominion of $-J(\omega_I - \omega_S)$.

Due to the results of Table III, we restrict our further discussion of the results for an 800 MHz spectrometer in Table IV to the comparison of model IV to simulation data A and model IX to simulation data B. Here, the frequency triple is shifted to the right to higher frequencies, resulting in smaller values for the spectral density function as well as more negative cross-relaxation rate σ_{IS}^{NOE}. The NOE-enhancement gets more negative too. Even more impressive is that the enhancement gets nearly independent of the distance, which is based on the ratio of σ_{IS}^{NOE} and ρ_{II}^{NOE}, as both terms show the same distance dependence. Although we observed a frequency dependence throughout all our model theories, models IV and IX show this behaviour least of all and are therefore the models of choice to best reproduce the results of simulation data.

V. RELATION TO EXPERIMENT

We complete this discussion by comments on the consequences of our results for the interpretation of experimental NOE data. Although intermolecular cross relaxation prospects unique information on both, the pair dynamics and pair structure, in simple liquids and solutions the NOE has almost exclusively been used as a structural tool. With one notable exception,[60] these studies have relied on measurements at a single spectrometer frequency, which renders data interpretation highly model-dependent.

This article is copyrighted as indicated in the article. Reuse of AIP content is subject to the terms at: http://scitation.aip.org/termsconditions. Downloaded to IP: 131.130.40.8 On: Mon, 12 May 2014 08:38:19

TABLE IV. For an 800 MHz Proton spectrometer we give the values for the distance resolved normalised spectral density function $J^N(\omega = \omega_i, R_{up})$ with $\omega_i = \omega_I - \omega_S, \omega_I, \omega_I + \omega_S$ as well as the absolute values for the longitudinal and cross-relaxation rates of the NOESY experiment and the NOE-enhancement for two model theories and our simulation data.

Pure translation												
Model	IV						A					
R_{up}(Å)	$\omega_I - \omega_S$	ω_I	$\omega_I + \omega_S$	σ_{IS}^{NOE}	ρ_{II}^{NOE}	$f_I\{S\}$	$\omega_I - \omega_S$	ω_I	$\omega_I + \omega_S$	σ_{IS}^{NOE}	ρ_{II}^{NOE}	$f_I\{S\}$
5	0.20	0.45	0.50	−0.0047	0.0181	−0.261	0.09	0.11	0.13	−0.0056	0.0084	−0.668
6	0.32	0.69	0.74	−0.0082	0.0282	−0.292	0.19	0.23	0.25	−0.0111	0.0167	−0.666
7	0.39	0.81	0.85	−0.0107	0.0338	−0.316	0.27	0.30	0.32	−0.0163	0.0235	−0.693
8	0.43	0.86	0.89	−0.0121	0.0364	−0.332	0.29	0.32	0.34	−0.0175	0.0251	−0.697
9	0.48	0.90	0.92	−0.0139	0.0391	−0.355	0.33	0.37	0.39	−0.0199	0.0286	−0.693
10	0.55	0.93	0.97	−0.0168	0.0432	−0.390	0.39	0.46	0.46	−0.0240	0.0346	−0.694
15	0.79	0.98	0.99	−0.0274	0.0547	−0.501	0.72	0.76	0.77	−0.0444	0.0620	−0.716
20	0.91	1.0	1.0	−0.0326	0.0602	−0.541	0.85	0.88	0.91	−0.0525	0.0731	−0.718
25	0.96	1.0	1.0	−0.0347	0.0629	−0.552	0.95	0.98	1.0	−0.0583	0.0811	−0.719
30	0.99	1.0	1.0	−0.0362	0.0638	−0.567	1.0	1.0	1.0	−0.0613	0.0857	−0.715
R_{up}=100	0.45	0.04	0.01	x	x	x	0.69	0.03	0.01	x	x	x
Ro-translational coupling												
Model	IX						B					
R_{up}(Å)	$\omega_I - \omega_S$	ω_I	$\omega_I + \omega_S$	σ_{IS}^{NOE}	ρ_{II}^{NOE}	$f_I\{S\}$	$\omega_I - \omega_S$	ω_I	$\omega_I + \omega_S$	σ_{IS}^{NOE}	ρ_{II}^{NOE}	$f_I\{S\}$
5	0.24	0.51	0.56	0.0004	0.0406	0.009	0.08	0.10	0.15	−0.0041	0.0143	−0.289
6	0.38	0.75	0.80	−0.0015	0.0603	−0.025	0.17	0.20	0.24	−0.0108	0.0278	−0.389
7	0.46	0.85	0.90	−0.0037	0.0700	−0.053	0.24	0.29	0.34	−0.0156	0.0401	−0.389
8	0.50	0.89	0.93	−0.0052	0.0739	−0.071	0.28	0.32	0.38	−0.0181	0.0452	−0.400
9	0.55	0.92	0.94	−0.0073	0.0777	−0.094	0.33	0.37	0.44	−0.0219	0.0531	−0.413
10	0.61	0.96	0.97	−0.0105	0.0828	−0.126	0.38	0.44	0.50	−0.0255	0.0619	−0.412
15	0.82	0.99	0.99	−0.0216	0.0960	−0.225	0.68	0.77	0.79	−0.0478	0.1069	−0.448
20	0.92	1.0	1.0	−0.0265	0.1020	−0.260	0.83	0.92	0.93	−0.0591	0.1289	−0.458
25	0.97	1.0	1.0	−0.0293	0.1046	−0.280	0.91	1.0	1.0	−0.0650	0.1419	−0.458
30	0.99	1.0	1.0	−0.0306	0.1055	−0.290	0.95	1.0	1.0	−0.0672	0.1485	−0.453
R_{up}=100	0.56	0.08	0.04	x	x	x	0.98	0.09	0.04	x	x	x

What is needed for an unambiguous analysis of experimental data is information on the frequency dependence of the intermolecular spectral density function $J(\omega)$. Experimental results for frequency-dependent longitudinal relaxation, which is complementary to cross relaxation, indeed provides such information.[14,53,61,62] With a few notable exceptions,[5,19–21,60] the consequences of these results for the interpretation of the NOE have, however, been ignored. Instead, most interpretations have explicitly or implicitly resorted to the Lorentzian ansatz

$$J(\omega) = K_{IS}\frac{1}{r^6}\frac{\tau_c}{1+\omega^2\tau_c^2} \tag{68}$$

or its extreme narrowing version

$$J(\omega) \approx J(\omega = 0) = \frac{K_{IS}\tau_c}{r^6}, \tag{69}$$

which form the standard expressions for interpreting intramolecular relaxation data.[2,8] Their adaption to intermolecular cross relaxation is more-or-less empirical, as is the assignment of the correlation time τ_c to the dynamical processes. In evaluating NOE data, τ_c is usually eliminated from the working equations by rescaling the measured cross relaxation rates with regard to a reference spin pair of known distance r_{ref}, so that $\sigma_{ij}/\sigma_{ij,ref} = r_{ref}^6/r^6$.[4–6]

It is obvious that the use of Eq. (68) as a means for describing the intermolecular spectral density function does not withstand the test of our theories and simulations. The rationale is that the Lorentzian ansatz, which implies a simple exponential relaxation process, ignores that the ro-translational pair dynamics is by far more complex than the purely rotational dynamics controlling intramolecular relaxation. Our simulations and model theories, as well as preceding theories at various levels of sophistication,[10,12,13] suggest that the decay of $J(\omega)$ is largely stretched compared to the Lorentzian shape. Taking the result in Fig. 9 as a prototypical example, the predicted decay of $J(\omega)$ for [EMIM][BF_4] extends over almost six decades in frequency, while a Lorentzian shape (not shown) can only cover two decades.

The stretched decay of $J(\omega)$ is confirmed by experimental studies of frequency dependent longitudinal relaxation.[53,61–63] Such experiments were employed a long time before sophisticated NOE techniques have become available,[63] and are still used in cases in which the NOE is difficult to measure.[53,62] Perhaps the most illustrative example is reported in a paper by Sacher *et al.*,[61] who observed a very broad dispersion regime for the intermolecular relaxation of methyl protons in aqueous solutions of tetramethylammonium chloride at spectrometer frequencies ν between 2 and 400 MHz. By contrast, intramolecular relaxation of the

This article is copyrighted as indicated in the article. Reuse of AIP content is subject to the terms at: http://scitation.aip.org/termsconditions. Downloaded to IP: 131.130.40.8 On: Mon, 12 May 2014 08:38:19

methyl protons proved to be independent of frequency. Essentially the same observation has been made by Furo and co-workers[60] in a study of the hydration of perfluorated anions by ^{19}F-^{1}H NOE, in very contrast to a frequency-independent intramolecular ^{19}F-^{19}F NOE.

It is worthwhile to note that these typical features of the intermolecular spectral density function persist in highly viscous systems, where the dynamical processes are affected by the approach to the glass transition.[53,62] This is important because the viscosities of ionic liquids are substantially higher than those of common molecular solvents.[23] Although our model compound [EMIM][BF_4] is a low-viscous ionic liquid, it possess an experimental viscosity of 34 mPa · s at 300 K,[64] which is about 40 times that of water.

The largely stretched shape of $J(\omega)$ has substantial consequences for the existence and accessibility of an extreme narrowing regime. The above-quoted observations in Refs. 60 and 61 imply that the frequency dependence of $J(\omega)$ extends far into the range, where standard arguments based on the viscosity and size of the particles suggest intermolecular relaxation to be independent of frequency, as actually observed for intramolecular relaxation in the same systems. In view of these observations, Furo and co-workers[60] have therefore argued that many, if not most intermolecular cross relaxation data have been interpreted under the erroneous assumption of extreme narrowing.

Similar conclusions can be drawn from NOE data for ionic liquids recorded by NOESY spectroscopy. In his review of NOE studies of ionic liquids,[45] Mele has pointed out that at the typical spectrometer frequencies of several hundred megahertz NOESY experiments for ionic liquids yield negative intermolecular NOEs, which is confirmed by our theoretical results for [EMIM][BF_4]. By contrast, data by Hayamizu *et al.*[64] show that at the same conditions intramolecular longitudinal ^{1}H-^{1}H and ^{19}F-^{19}F relaxation shows only a weak frequency dependence and is close to the extreme narrowing regime.

Finally, in most cases the use of the intermolecular NOE as a tool for determining intermolecular structures has been based on the presumption of a r^{-6} dependence of the spectral density function, which implies that local structures are probed. Our results prove such an assumption to be untenable. While this conjecture has already emerged at various levels of sophistication from a series of preceding theoretical studies,[7–13] our approach now enables a detailed spatial resolution of the distance dependence of $J(\omega)$. Depending on the model, we find for [EMIM][BF_4] notable contributions to the NOE up to internuclear distances of 15–30 Å, which corresponds to 3–5 coordination shells. Site-specific NOE measurements therefore reflect the mean orientation of ions over comparatively long distances rather than the local structure, even though in some cases the average ion configurations as typical outcomes are remarkably consistent with expectations for local structures, e.g., from quantum-mechanical calculations for ion pairs.[39]

VI. CONCLUSION

By a combination of simulation and model theories this paper analyses the impact of pair dynamics on the intermolecular NOE in liquids. To our best knowledge this is the first study of the NOE at full distance resolution. Furthermore, it is the first application to an ionic liquid. Our findings are:

- One can cope with the computational efforts to simulate the heteronuclear NOE at least for high spectrometer frequencies. Since the computation of the homonuclear NOE requires the spectral density at zero frequency, this is still a barrier.
- Although, the whole frequency range can be covered by model theories, the usual procedure to describe the structure of the interacting nuclei by a step function and the pair dynamics by a solution of the diffusion equation is not sufficient. In order to get reasonable agreement with simulation data we had to use the detailed radial distribution function $g^{+-}_{000}(R_0)$.
- In addition, the implementation of a more complex pair dynamics beyond simple diffusion is necessary. Therefore, we have tested existing non-Gaussion diffusion models such as jump and lattice diffusion. But we had to develop a further model based on the fit of the simulated pair displacement of the ionic liquid [EMIM][BF_4], which showed best consistency with our simulated data.
- At the quantitative level, ro-translational coupling is important, but the qualitative feature of the spectral density function $J(\omega)$ is essentially determined by purely translational pair dynamics.
- A detailed analysis of the distance dependence of the spectral density function revealed that the frequency dependence of the range of the NOE decreases with increasing complexity of the model theories and disappears altogether for simulation. Thus, in a realistic description $J(\omega)$ becomes long-ranged extending up to 30 Å or equivalently to the fourth shell of $g^{+-}_{000}(R_0)$.
- Even more sensitive is the cross-relaxation rate σ^{NOE}_{IS}, which balances contributions from high and low frequencies. Therefore, the curvature of the spectral density function plays an important role for the actual value of σ^{NOE}_{IS}. Depending on the combination of the fluidity of the sample and the spectrometer frequency the sign of σ^{NOE}_{IS} can be changed. When normalising the cross-relaxation rate σ^{NOE}_{IS} by the longitudinal relaxation rate ρ^{NOE}_{II} the resulting NOE-enhancement may become short-ranged.

ACKNOWLEDGMENTS

This work was supported by Project No. P23494 of the FWF Austrian Science Fund as well as the Cluster of Excellence RESOLV (EXC 1069) funded by the Deutsche Forschungsgemeinschaft.

[1] I. Solomon, Phys. Rev. **99**, 559 (1955).
[2] D. Neuhaus and M. P. Williamson, *The Nuclear Overhauser Effect in Structural and Conformational Analysis* (Wiley-VCH, Weinheim, 2000).
[3] J. Cavanagh, W. J. Fairbrother, A. G. Palmer III, and N. J. Skelton, *Protein NMR Spectroscopy: Principles and Practice* (Academic Press, San Diego, 1996).
[4] H. Mo and T. C. Pochapsky, Prog. Nucl. Magn. Reson. Spectrosc. **30**, 1 (1997).

This article is copyrighted as indicated in the article. Reuse of AIP content is subject to the terms at: http://scitation.aip.org/termsconditions. Downloaded to IP: 131.130.40.8 On: Mon, 12 May 2014 08:38:19

[5]J. T. Gerig, Annu. Rep. NMR Spectrosc. **64**, 21 (2008).
[6]T. Brand, E. Cabrita, and S. Berger, Progr. Nucl. Magn. Reson. Spectrosc. **46**, 159 (2005).
[7]H. C. Torrey, Phys. Rev. **92**, 962 (1953).
[8]A. Abragam, *The Principles of Nuclear Magnetism* (Clarendon, Oxford, 1961), p. 300.
[9]Y. Ayant, E. Belorizky, J. Aluzon, and J. Gallice, J. Phys. **36**, 991 (1975).
[10]L. Hwang and J. H. Freed, J. Chem. Phys. **63**, 4017 (1975).
[11]C. A. Sholl, J. Phys. C: Solid State Phys. **14**, 447 (1981).
[12]Y. Ayant, E. Belorizky, P. Fries, and J. Rosset, J. Phys. **38**, 325 (1977).
[13]B. Halle, J. Chem. Phys. **119**, 12372 (2003).
[14]M. D. Zeidler, Mol. Phys. **30**, 1441 (1975).
[15]S. Gabl, O. Steinhauser, and H. Weingärtner, Angew. Chem. Int. Ed. **52**, 9242 (2013).
[16]M. Odelius, A. Laaksonen, M. H. Levitt, and J. Kowalewski, J. Magn. Reson. A **105**, 289 (1993).
[17]J.-P. Grivet, J. Chem. Phys. **123**, 034503 (2005).
[18]P.-O. Westlund and R. M. Lynden-Bell, J. Magn. Reson. **72**, 522 (1987).
[19]J. T. Gerig, J. Magn. Reson. **210**, 171 (2011).
[20]M. Luhmer, A. Moschos, and J. Reisse, J. Magn. Reson. Ser. A **113**, 164 (1995).
[21]J. T. Gerig, J. Phys. Chem. B **116**, 1965 (2012).
[22]S. Gabl, C. Schröder, and O. Steinhauser, J. Chem. Phys. **137**, 094501 (2012).
[23]H. Weingärtner, Angew. Chem. Int. Ed. **47**, 654 (2008).
[24]N. V. Plechkova and K. R. Seddon, Chem. Soc. Rev. **37**, 123 (2008).
[25]C. Schröder, T. Sonnleitner, R. Buchner, and O. Steinhauser, Phys. Chem. Chem. Phys. **13**, 12240 (2011).
[26]C. Schröder and O. Steinhauser, J. Chem. Phys. **133**, 154511 (2010).
[27]C. Schröder and O. Steinhauser, J. Chem. Phys. **132**, 244109 (2010).
[28]C. Schröder and O. Steinhauser, J. Chem. Phys. **131**, 114504 (2009).
[29]C. Schröder, J. Hunger, A. Stoppa, R. Buchner, and O. Steinhauser, J. Chem. Phys. **129**, 184501 (2008).
[30]C. Schröder and O. Steinhauser, J. Chem. Phys. **128**, 224503 (2008).
[31]C. Schröder, M. Haberler, and O. Steinhauser, J. Chem. Phys. **128**, 134501 (2008).
[32]C. Schröder, C. Wakai, H. Weingärtner, and O. Steinhauser, J. Chem. Phys. **126**, 084511 (2007).
[33]C. Daguenet, P. J. Dyson, I. Krossing, A. Oleinikova, J. Slattery, C. Wakai, and H. Weingärtner, J. Phys. Chem. B **110**, 12682 (2006).
[34]H. Weingärtner, P. Sasisanker, C. Daguenet, P. J. Dyson, I. Krossing, J. M. Slattery, and T. Schubert, J. Phys. Chem. B **111**, 4775 (2007).
[35]M.-M. Huang and H. Weingärtner, Chem. Phys. Chem. **9**, 2172 (2008).
[36]M.-M. Huang, Y. Jiang, P. Sasisanker, G. D. Driver, and H. Weingärtner, J. Chem. Eng. Data **56**, 1494 (2011).
[37]M. Schmollngruber, C. Schröder, and O. Steinhauser, J. Chem. Phys. **138**, 204504 (2013).
[38]R. A. Mantz, P. C. Trulove, R. T. Carlin, and R. A. Osteryoung, Inorg. Chem. **34**, 3846 (1995).
[39]Y. Lingscheid, S. Arenz, and R. Giernoth, Chem. Phys. Chem. **13**, 261 (2012).
[40]A. Mele, G. Romano, M. Giannone, E. Ragg, G. Fronza, G. Raos, and V. Marcon, Angew. Chem. **118**, 1141 (2006).
[41]C. Chiappe, A. Sanzone, D. Mendola, F. Castiglione, A. Famulari, G. Raos, and A. Mele, J. Phys. Chem. B **117**, 668 (2013).
[42]P. Judeinstein, C. Iojoiu, J.-Y. Sanchez, and B. Ancian, J. Phys. Chem. B **112**, 3680 (2008).
[43]D. Nama, P. G. Anil Kumar, P. S. Pregosin, T. J. Geldbach, and P. J. Dyson, Inorg. Chim. Acta **359**, 1907 (2006).
[44]D. Bankmann and R. Giernoth, Prog. Nucl. Magn. Reson. Spectrosc. **51**, 63 (2007).
[45]A. Mele, Chim. Oggi/Chem. Today **28**, 48 (2010).
[46]H. Weingärtner, Curr. Opin. Colloid Interface Sci. **18**, 183 (2013).
[47]J. P. Hansen and I. R. McDonald, *Theory of Simple Liquids*, 3rd ed. (Elsevier, 2006).
[48]J. P. Boon and S. Yip, *Molecular Hydrodynamics* (Dover Publications, Inc., New York, 1980).
[49]P. A. Egelstaff, J. Chem. Phys. **53**, 2590 (1970).
[50]J. R. Sangoro, C. Iacob, S. Naumov, R. Valiullin, H. Rexhausen, J. Hunger, R. Buchner, V. Strehmel, J. Kärger, and F. Kremer, Soft Matter **7**, 1678 (2011).
[51]E. N. Ivanov, Zh. Eksp. Teor. Fiz. **45**, 1509 (1963).
[52]E. N. Ivanov, Sov. Phys. JETP **18**, 1041 (1964).
[53]R. Meier, D. Kruk, and E. A. Rössler, Chem. Phys. Chem. **14**, 3071 (2013).
[54]M. Haberler, C. Schröder, and O. Steinhauser, J. Comput. Theory Chem. **8**, 3911 (2012).
[55]N. Michaud-Agrawal, E. J. Denning, T. B. Woolf, and O. Beckstein, J. Comput. Chem. **32**, 2319 (2011).
[56]C. Schröder, T. Rudas, G. Neumayr, W. Gansterer, and O. Steinhauser, J. Chem. Phys. **127**, 044505 (2007).
[57]C. Schröder, T. Rudas, and O. Steinhauser, J. Chem. Phys. **125**, 244506 (2006).
[58]P. Fries and E. Belorizky, J. Phys. **39**, 1263 (1978).
[59]D. Frezzato, F. Rastrelli, and A. Bagno, J. Phys. Chem. B **110**, 5676 (2006).
[60]L. Nordstierna, P. V. Yushmanov, and I. Furó, J. Chem. Phys. **125**, 074704 (2006).
[61]F. Sacher, M. Holz, and H. Hertz, J. Magn. Reson. A **103**, 61 (1993).
[62]D. Kruk, R. Meier, and E. A. Rössler, J. Phys. Chem. B **115**, 951 (2011).
[63]J. P. Kintzinger and M. D. Zeidler, Ber. Bunsenges. Phys. Chem. **77**, 98 (1973).
[64]K. Hayamizu, S. Tsuzuki, S. Seki, and Y. Umebayashi, J. Phys. Chem. B **116**, 11284 (2012).

This article is copyrighted as indicated in the article. Reuse of AIP content is subject to the terms at: http://scitation.aip.org/termsconditions. Downloaded to IP: 131.130.40.8 On: Mon, 12 May 2014 08:38:19

6 On the solvation dynamics of coumarin C153 in ionic liquids: Comparison of non-equilibrium simulation to equilibrium simulation and experiment

On the solvation dynamics of coumarin C153 in ionic liquids: Comparison of non-equilibrium simulation to equilibrium simulation and experiment

Sonja Gabl, Christian Schröder and Othmar Steinhauser[1]

University of Vienna, Department of Computational Biological Chemistry, Austria

The solvation dynamics of coumarin C153 dissolved in two ionic liquids, $C_2mim^+OTf^-$ and $C_4mim^+BF_4^-$, was investigated by means of non-equilibrium and equilibrium molecular dynamics simulation as well as experiment. A new approach of generating start configurations for non-equilibrium simulations has been tested and to assess the quality of this new method, the resulting solvation response functions were compared to equilibrium simulation and experiment. All methods were in good agreement to each other. Furthermore, component analysis of the solvation response function was carried out for non-equilibrium simulation data in terms of cations and anions as well as permanent and induced charges.

I. INTRODUCTION

The understanding of solvation dynamics has been of great interest to experimenters as well as theorists. The time-dependent Stokes shift of the fluorescence emission of a probe molecule dissolved in a solvent can be used to study local solvation effects.

The central quantity provided by experiment is the normalised solvation response function

$$S_{exp}(t) = \frac{\nu(t) - \nu(\infty)}{\nu(0) - \nu(\infty)}, \tag{1}$$

where $\nu(t)$ is actually defined as the peak maximum of a distribution and describes the time evolution of the emission frequency, with its limits being $\nu(0)$ and $\nu(\infty)$. The distribution occurs because there is more than one solute molecule present in the probe and each coumarin C153 is giving its own response. The group of Maroncelli reports that the distribution is of log-normal shape.[1,2]

Over the years molecular dynamics simulation proved itself to be of great assistance in the interpretation of experimental data. In early theoretical works[3–8] simple or model solutes were used to simplify the demands on computational resources and to gain a general understanding of solvation dynamics. Later on, more elaborate solute molecules, such as coumarin C153 or other polyatomic solutes, were dissolved in various solvents and their respective Stokes shifts were investigated.[9–12]

The appearance of room temperature ionic liquids, a new class of solvents, posed a new challenge with respect to solvation dynamics to experiment,[1,13–24] theory[1,25–28] and molecular dynamics simulation[29–38]. In the last decade, the number of molecular dynamics studies on solvation dynamics of ionic liquids is steadily increasing. Thereby, a lot of different solute molecules were investigated such as rigid, diatomic ones[13,31] or benzenelike molecules[31] or betaine-30[34,39] as well as coumarin C153[15,40].

Regardless of the solute molecule used, the authors had to use either molecular dynamics simulation in equilibrium or non-equilibrium to study solvation dynamics. In case of simulation in non-equilibrium, all groups pursued the same approach of generating new start configurations. Different non-equilibrium trajectories are provided by simulating in equilibrium and changing from ground ($S0$) to excited state ($S1$) in intervals separated by only a few time steps. In this work, we follow a different course of action. We prepare individual start configurations by use of PACKMOL[41], which should ensure a better phase space sam-

pling. To assess the quality of the provided start configurations and their trajectories, we will compare them to results of equilibrium simulations as well as experiment.

In simulations the root of the solvation response function is the difference in the electrostatic solvation energy between $S0$ and $S1$

$$\Delta U(t) = \sum_{\gamma}^{solute} \Delta q_\gamma V_\gamma(t), \tag{2}$$

where Δq_γ is the difference in solute charge and the electrostatic potential $V_\gamma(t)$, acting on the solute atoms, is defined as

$$V_\gamma(t) = \sum_{i\beta} \frac{q_{i\beta}}{4\pi\epsilon_0 r_{\gamma i\beta}}, \tag{3}$$

where i refers to molecules and β to atoms respectively. The electrostatic potential $V_\gamma(t)$ can be separated into different components

$$V_\gamma(t) = V_\gamma^1(t) + V_\gamma^2(t), \tag{4}$$

where the indices 1 and 2 refer to either cations and anions or permanent and induced charges. For a detailed description of permanent and induced charges, i.e. the Drude formalism, please refer to another work.[42] Please note, that in case of Drude oscillator functions the induced dipole is represented by a pair of particles tethered by a spring. One particle is fixed at the position of the polarizable atom, the other one is mobile and responds to the local electric field. However, since these particles can be more or less treated like normal atoms with a partial charge, the Coulomb energy can be easily split up into permanent contributions (interaction between the atoms and the solute charge Δq_γ) and induced contributions (interaction of a Drude particle with the solute charge Δq_γ).

In case of non-equilibrium simulation the normalised solvation response function is now defined as follows

$$S(t) = \frac{\overline{\Delta U(t)} - \overline{\Delta U(\infty)}}{\overline{\Delta U(0)} - \overline{\Delta U(\infty)}}, \tag{5}$$

where $\Delta U(t)$ is the difference in solvation energy between the ground state ($S0$) and the excited state ($S1$). The overbar indicates averaging over non-equilibrium trajectories. The averaging is necessary, because in contrast to experiment, there is only one solute molecule dissolved in its solvent in a box during simulation.

In contrast to experiment, the computational analysis has the advantage to decompose the resulting Stokes shift function $S(t)$ into its important components thus facilitating the

interpretation. Therefore, we split $S(t)$ into $S_+(t)$ and $S_-(t)$ or $S_{perm}(t)$ and $S_{ind}(t)$. This decomposition refers to the numerator of Eq.5 only and thus uses an uniform denominator $\Delta\Delta U = \overline{\Delta U(0)} - \overline{\Delta U(\infty)}$ and we can write

$$\Delta\Delta U \cdot S(t) = \overline{\Delta U(t)} - \overline{\Delta U(\infty)} \tag{6}$$

$$= \Delta\Delta U \cdot (S_+(t) + S_-(t)) = \big(\overline{\Delta U_+(t)} - \overline{\Delta U_+(\infty)}\big) + \big(\overline{\Delta U_-(t)} - \overline{\Delta U_-(\infty)}\big) \tag{7}$$

$$= \Delta\Delta U \cdot (S_{perm}(t) + S_{ind}(t)) = \big(\overline{\Delta U_{perm}(t)} - \overline{\Delta U_{perm}(\infty)}\big) + \big(\overline{\Delta U_{ind}(t)} - \overline{\Delta U_{ind}(\infty)}\big). \tag{8}$$

In case of equilibrium simulations two trajectories are generated, one for the ground state ($S0$) and one for the excited state ($S1$). The solvation response function can be expressed in the terms of a time correlation function (TCF),

$$C(t) = \frac{\langle \delta\Delta U(0) \cdot \delta\Delta U(t) \rangle}{\langle \delta\Delta U^2 \rangle}, \tag{9}$$

where $\delta\Delta U(t)$ represents the fluctuations $\delta\Delta U(t) = \Delta U(t) - \langle \Delta U \rangle$. Here, $\langle \Delta U \rangle$ corresponds to averaging over time instead of different configurations, as it is the case in non-equilibrium. It is also possible to do a component analysis for equilibrium simulations, but the description demands that cross-terms are included

$$C(t) = \frac{C_1(t) + C_2(t) + 2\chi_{12}(t)}{C_1(0) + C_2(0) + 2\chi_{12}(0)}, \tag{10}$$

where the indices 1 and 2 refer again to either cations and anions or permanent and induced charges. The cross-terms are necessary, because the TCF is made up by a product instead of a sum, as is the case for non-equilibrium. For a more detailed description of the theory on component analysis in equilibrium simulation please refer to our previous work.[43]

By comparing Eq.10 to Eq.7-8 it can readily be seen that the formalism for equilibrium simulation is a lot more complex than that for non-equilibrium simulation due to the cross-terms.[40]

In this work, we will use the above developed equations to compare results of non-equilibrium as well as equilibrium simulation to experiment. That way we can assess if both methods are equal or if one method should be favoured over the other. Furthermore, we will have a closer look on component analysis by means of non-equilibrium data, which is easier to interpret, since we do not have to deal with cross-terms.

II. METHODS

In this work we carried out non-equilibrium molecular dynamics simulations of coumarin C153 dissolved in two different ionic liquids, $C_2mim^+OTf^-$ and $C_4mim^+BF_4^-$. Each system contained one coumarin C153 in the electronic ground state ($S0$) and 1000 ion pairs. For each system 150 'independent' start configurations were obtained by using different seeds in PACKMOL.[41] Every configuration was minimized for 140 steps by the steepest descent method using an unpolarized force field. Afterwards, we switched to a polarized force field and minimised for an additional 50 steps with the steepest descent method to obtain reasonable energies. For more details concerning the force field parameters please refer to our previous work.[43] To equilibrate all configurations they were simulated for 1ns in the ground state. For the actual non-equilibrium simulation an instantaneous change of the charge distribution from the electronic ground state ($S0$) to the excited state ($S1$) came to pass. Then, we simulated each configuration in the excited state ($S1$) for 1ns.

All simulations were performed with the program package CHARMM[44,45] at 300K in cubic boxes with a box length of 64.4Å for $C_2mim^+BF_4^-$ and 68.65Å for $C_4mim^+BF_4^-$ under periodic boundary conditions. A time step of 0.5fs was applied. The SHAKE algorithm[46] kept all bonds involving a hydrogen atom at a constant length. Non-bonded and image lists used a 14Å cut-off distance and were heuristically updated. Lennard-Jones interactions were smoothly switched off between 9 and 10Å, while electrostatic interactions were calculated using the PME method.[47,48] Real space interactions were cut off at 10Å and the damping constant for interactions in reciprocal space was $0.41Å^{-1}$. We used 54 grid points and the charges in the grid were interpolated by sixth-order spline functions. To include polarizability of the solvent molecules, Drude oscillators were attached to all non-hydrogen molecules. All Drude particles have the same uniform charge of $q^\delta = -2.0e$ and a mass of $m^\delta = 0.2$amu, which were both subtracted from the respective atomic parameters. Please refer to our previous work for a more detailed description of the computational setup concerning Drude oscillators.[42,49,50]

All equilibrium trajectories used in this work stem from our previous publication.[43]

	$C_2mim^+OTf^-$	$C_4mim^+BF_4^-$
$\langle \Delta U(t) \rangle_{eq}$	-40.2	-39.6
$\overline{\Delta U(\infty)}$	-40.1	-39.6
$\overline{\Delta U(0)}$	-18.9	-16.8
$\overline{\Delta U_+(\infty)}$	-31.6	-26.9
$\overline{\Delta U_-(\infty)}$	-8.5	-12.6

TABLE I. Various solvation energies for equilibrium and non-equilibrium simulations are given in kcal mol^{-1}. The value of $\langle \Delta U(t) \rangle_{eq}$ was calculated by averaging the time series of $\Delta U(t)$ of the whole equilibrium trajectory. $\overline{\Delta U(\infty)}$ and $\overline{\Delta U(0)}$ are the limits of $\overline{\Delta U(t)}$, where the overbar indicates averaging over 150 non-equilibrium trajectories. The indices + and − refer to cations and anions respectively.

III. RESULTS AND DISCUSSION

A. Assessment of the quality of non-equilibrium simulations

To calculate the solvation response function $S_{neq}(t)$ of non-equilibrium simulations, we averaged over 150 'independent' simulations. So far, start configurations for non-equilibrium simulations were generated by simulating in equilibrium and changing from ground ($S0$) to excited state ($S1$) in intervals separated by a few time steps.[3,4,10,51,52] This approach may have its merits, since one can take out start configurations, ready to use, by simulating one trajectory in equilibrium, but the resulting non-equilibrium trajectories are very similar to each other and sample the same region in phase space. In our case we generate different start configurations, where we have to equilibrate each on its own, but we cover a greater region in phase space. As an indicator for sufficient averaging over non-equilibrium trajectories, we have a closer look on $\langle \Delta U(t) \rangle_{eq}$, gained from equilibrium simulation in the excited state $S1$, and $\overline{\Delta U(\infty)}$, calculated from non-equilibrium simulations. For the evaluation of $\langle \Delta U(t) \rangle_{eq}$ the time series of $\Delta U(t)$ was averaged over the entire trajectory length of at least 50ns for the excited state $S1$. For $\overline{\Delta U(\infty)}$ on the other hand the last value of all 150 non-equilibrium trajectories were averaged. Consulting Table I the consistency of $\langle \Delta U(t) \rangle_{eq}$ and $\overline{\Delta U(\infty)}$ for both ILs is satisfying.

Another approach to validate the quality of our non-equilibrium simulations is to transfer

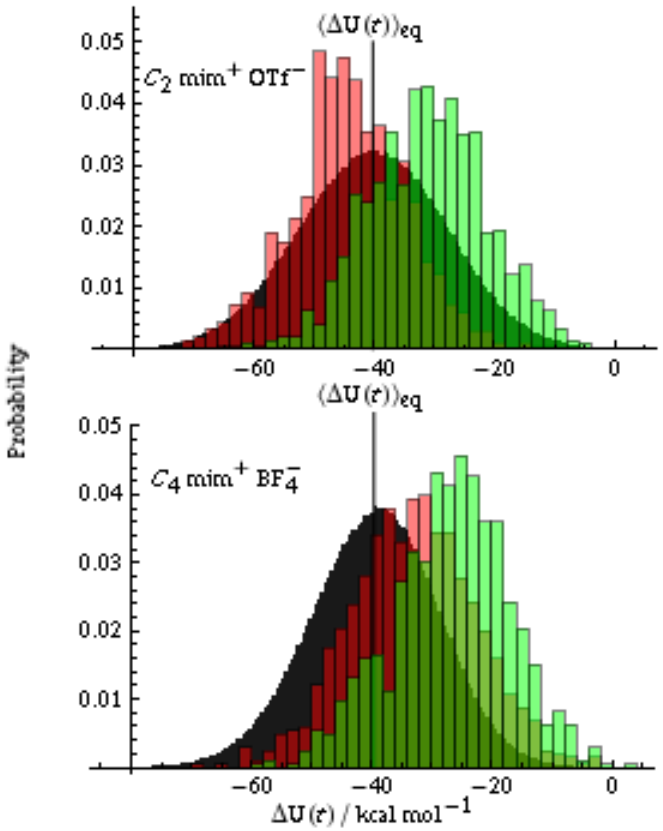

FIG. 1. Here, we give normalised histograms of equilibrium and non-equilibrium data. The black histogram is made up by values of $\Delta U(t)_{eq}$ of equilibrium trajectories simulated for $S1$. The black line represents the average of $\Delta U(t)_{eq}$, i.e. $\langle \Delta U(t) \rangle_{eq}$. The red histogram shows the distribution of $\Delta U(\infty)$ of non-equilibrium trajectories, whereas the blue one stands for $\Delta U(0)$. The graph at the top refers to $C_2mim^+OTf^-$ and $C_4mim^+BF_4^-$ can be found at the bottom.

all 150 values of $\Delta U(\infty)$ to a normalised histogram (red) and compare it to a normalised histogram (black) composed by the values of $\Delta U(t)$ from equilibrium as depicted in Fig.1. For both ILs the histograms, which belong to equilibrium simulation are of the shape of a Gauss function. In contrast, the histograms, which belong to non-equilibrium simulation, are of inherent log-normal shape. This is actually in accordance with experiment, where the time evolution of the solvation response is given by an emission band, which can be fitted by log-normal line shape functions.[2] Although, the shape of the non-equilibrium histogram is in good agreement with experiment, on a logarithmic scale the histogram is still asymmetric,

so experimental data cannot be exactly reproduced.

For $C_2mim^+OTf^-$ the black and red histograms lie on top of each other, whereas for $C_4mim^+BF_4^-$ the histogram, which belongs to non-equilibrium, is slightly shifted to the right. A possible explanation for the shift is that due to the high viscosity of $C_4mim^+BF_4^-$, simulation in equilibrium got stuck in phase space and would have required more time for its investigation. Although there is this discrepancy, it should be of no importance according to the values of $\langle \Delta U(t) \rangle_{eq}$ and $\overline{\Delta U(\infty)}$ in Table I. As a next step, we have a closer look at the values of $\overline{\Delta U(0)}$ and the according distribution of values, represented by the green histograms. We observe that the green histogram, which corresponds to excitation to $S1$ at $t = 0$ is shifted to the left over time until it reaches $t = \infty$ after 1ns, given by the red histogram. The difference of the peak maxima of $\overline{\Delta U(0)}$ and $\overline{\Delta U(\infty)}$ is again confirmed by Table I.

Taking into account the values in Table I and the results of the histograms, we take this as a validation that the number of simulations is sufficient and the results from non-equilibrium simulation are consistent with equilibrium simulation.

B. Solvation response function

In Fig. 2 we present the solvation response functions computed from non-equilibrium simulations and compare it to the results of our equilibrium simulations[43] as well as experimental data by Maroncelli *et al.*[1] For $C_2mim^+OTf^-$ (at the top of the first column of Fig. 2) we observe the best accordance of non-equilibrium results (shown in black) to experimental data (given in red), whereas data from equilibrium simulation (displayed in green) lies slightly above the other graphs. At the bottom of the first column of Fig. 2 the results for $C_4mim^+BF_4^-$ are shown. We observe the same shape for the non-equilibrium simulation result (black) in comparison to experimental data (red), but the graph is shifted downwards. In contrast, we can see that the solvation response function of equilibrium simulation (green) follows the curvature of the experimental graph, but only for a few picoseconds. The asymptotic regime deviates due to the high viscosity of $C_4mim^+BF_4^-$, where we have to face insufficient sampling of slow processes. Due to the low viscosity of $C_2mim^+OTf^-$ we observe less discrepancies in the various graphs than for those of $C_4mim^+BF_4^-$. This viscosity dependence, especially in the long-time regime of the solvation response function

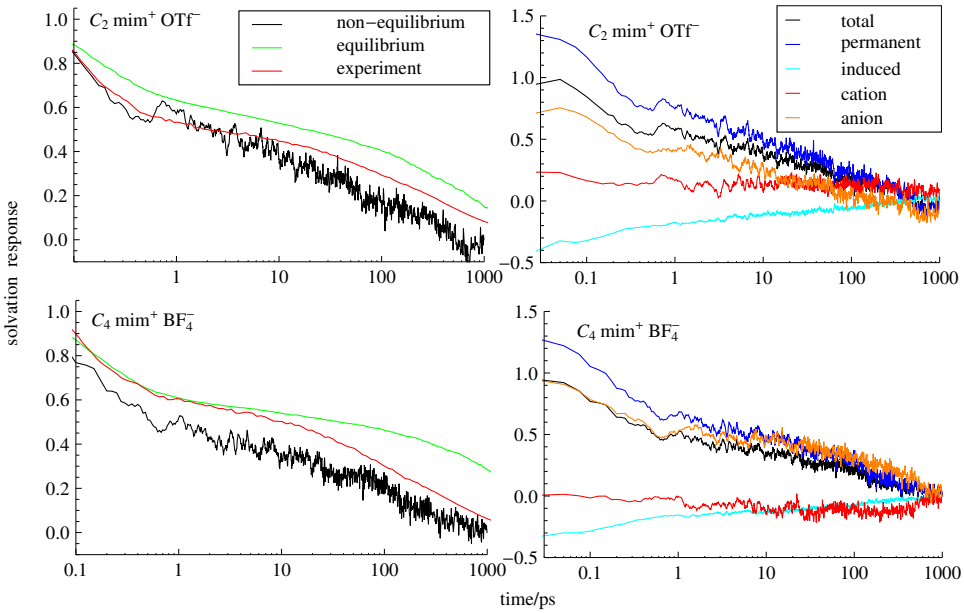

FIG. 2. Various solvation response functions of $C_2mim^+OTf^-$ can be found in the first row, whereas $C_4mim^+BF_4^-$ is represented in the second row. In the first column the total solvation response functions of the experiment are given in red, results for non-equilibrium are given in black and equilibrium is shown in green. The second column deals with various contributions to the total solvation response function (black). Contributions of permanent and induced charges are given in blue and cyan and the parts made up by cations and anions are represented in red and orange respectively.

of ionic liquids, has already been pointed out.[19,21,53]

C. Component analysis of solvation response function

In equilibrium simulation it is possible to investigate the contribution of components to the total solvation response function as shown in Eq.10. Unfortunately, one has to

deal with cross-terms χ_{12}, which do not facilitate interpretation.[32,34,40,43] The advantage of working with non-equilibrium simulations is that one can avoid cross-terms in analysis, due to the additivity of all components contributing to the total energy (cf. Eq.6 and below). In the second column of Fig. 2 we present for $C_2mim^+OTf^-$ and $C_4mim^+BF_4^-$ the total solvation response function in black as well as separate contributions in colour. Permanent charges are coloured in blue and the part from induced charges, i.e. Drude charges, is given in cyan. For both ionic liquids studied here, we find the same pattern. The total solvation response function is made up for the most part by permanent charges. At the beginning, where we instantaneously change the charge of C153 from $S0$ to $S1$, induced charges, representing polarizability, have a strong negative contribution of about one third of the total solvation response function, which steadily increases in a linear way on a logarithmic scale to values of about zero around 1ns. In other words, the contribution from the electrostatic potential of the induced charges counteracts the contribution from the electrostatic potential of permanent charges. The capability of the electrostatic potential of induced charges to act as an inner solvent is extremely important for a correct description of the total solvation response function, because it can react adequately to the sudden change in the charge distribution of the solute molecule C153.

We can also split up the total solvent response function into contributions of cations and anions, given in Fig. 2 in red and orange respectively. It can easily be seen that the total solvation response function has its shape from the electrostatic potential of the anions, whereas the contribution of $V_\gamma^+(t)$ of the cations is almost constant over time. Nevertheless, by consulting the values for $\overline{\Delta U_+(\infty)}$ and $\overline{\Delta U_-(\infty)}$ in Table I, it is obvious that the cations play an important role in total value, but not for transient behaviour. In case of $C_2mim^+OTf^-$ 79% of $\overline{\Delta U(\infty)}$ is made up by cations, for $C_4mim^+BF_4^-$ the cations account for 68%. In other words, cations are responsible for a constant, high background due to its electrostatic potential and they screen the charges of the solute. Because the contribution of cations does not change over time, this information gets lost by normalising the solvation response function.

IV. SUMMARY AND CONCLUSION

In this work we pursued a different approach to generate start configurations for non-equilibrium simulation runs. By use of the program PACKMOL,[41] 150 'independent' start configurations were constructed and non-equilibrium simulations were conducted. This has the advantage of a better phase space sampling. To assess the quality and number of simulations, $\langle \Delta U(t) \rangle_{eq}$, gained from equilibrium simulation, and $\overline{\Delta U(\infty)}$, calculated from non-equilibrium simulation, were compared to each other. Furthermore, normalised histograms of the distribution of values, which lead to $\langle \Delta U(t) \rangle_{eq}$ and $\overline{\Delta U(\infty)}$, were created. The averaged values as well as the histograms lead to the conclusion that equilibrium and non-equilibrium simulations are consistent. In addition, the histogram made up from the sampling over non-equilibrium values is closer in shape to the experimentally measured emission band than that of equilibrium simulation. Moreover, the difference of $\overline{\Delta U(0)}$ and $\overline{\Delta U(\infty)}$ can also be found in the position of the maxima of the corresponding histograms (red and green in Fig.1).

The comparison of the total solvation response functions, gained from non-equilibrium simulations, equilibrium simulation and experiment, showed a good agreement for both ionic liquids, $C_2mim^+OTf^-$ and $C_4mim^+BF_4^-$. For $C_4mim^+BF_4^-$ the result for non-equilibrium simulations is even better than that of equilibrium simulation, because the asymptotic time region does not suffer from insufficient sampling of phase space.

A real advantage of dealing with non-equilibrium simulations lies in the calculation of various contributions to the total solvation response function. The segmentation into contributions of permanent and induced charges or into contributions of cations and anions does not include cross-terms, which complicate interpretation. With regard to permanent and induced charges, our findings are that induced charges counteract permanent charges in a steadily increasing linear function on a logarithmic scale until its contribution to the total solvation response reaches zero. Thereby, induced charges fulfil the important role of an inner solvent for the correct description of the total solvation response function.

Looking at the graphs for the contributions of cations and anions, it is obvious that the anions are responsible for the shape of the total solvation response function, whereas the contribution of cations does not change over time. Nevertheless, the cations reveal their importance while considering the unnormalised value of $\overline{\Delta U_+(\infty)}$, where they account for

70-80% of the total energy $\overline{\Delta U(\infty)}$, i.e. cations give a high but constant background.

We would like to finish this summary with some concluding remarks. In comparison to experiment, simulation in equilibrium as well as non-equilibrium are equivalent methods. However, simulation in non-equilibrium appears to have some advantages. First, the interpretation of analysis data is facilitated, because of missing cross-terms. Second, with suitable computer architecture one can easily run non-equilibrium simulations parallel.

V. ACKNOWLEDGEMENTS

We would like to thank the Vienna Scientific Cluster (http://www.zid.tuwien.ac.at/vsc) of the University of Vienna, the Vienna University of Technology and the University of Natural Resources and Applied Life Science Vienna for the generous allocation of computer time. This work was supported by Project No. P23494 of the Austrian Science Fund FWF.

REFERENCES

[1]M. Maroncelli, X.-X. Zhang, M. Liang, D. Roy, and N. P. Ernsting, Faraday Discuss. **154**, 409 (2012).

[2]X.-X. Zhang, M. Liang, N. P. Ernsting, and M. Maroncelli, J. Phys. Chem. B **117**, 4291 (2013).

[3]T. Fonseca and B. M. Ladanyi, J. Phys. Chem. **95**, 2116 (1991).

[4]O. A. Karim, A. D. J. Haymet, M. J. Banet, and J. D. Simon, J. Phys. Chem. **92**, 3391 (1988).

[5]M. Maroncelli and G. R. Fleming, J. Chem. Phys. **86**, 6221 (1987).

[6]E. Bernardi, M. M. Martins, and H. Stassen, Chem. Phys. Lett. **407**, 171 (2005).

[7]B. D. Bursulaya, D. A. Zichi, and H. J. Kim, J. Phys. Chem. **99**, 10069 (1995).

[8]E. A. Carter and J. T. Hynes, J. Chem. Phys. **94**, 5961 (1991).

[9]F. Cichos, R. Brown, and P. A. Bopp, J. Chem. Phys. **114**, 6834 (2001).

[10]L. R. Martins, A. Tamashiro, D. Laria, and M. S. Skaf, J. Chem. Phys. **118**, 5955 (2003).

[11]B. M. Ladanyi and M. Maroncelli, J. Chem. Phys. **109**, 3204 (1998).

[12]B. M. Ladanyi and B.-C. Perng, J. Phys. Chem. A **106**, 6922 (2002).

[13]P. K. Mandal, S. Saha, R. Karmakar, and A. Samanta, Curr. Science **90**, 301 (2006).

[14]N. Ito, S. Arzhantsev, and M. Maroncelli, Chem. Phys. Lett. **396**, 83 (2004).

[15]N. Ito, S. Arzhantsev, M. Heitz, and M. Maroncelli, J. Phys. Chem. B **108**, 5771 (2004).

[16]B. Lang, G. Angulo, and E. Vauthey, J. Phys. Chem. A **110**, 7547 (2006).

[17]J. Wishart, J. Phys. Chem. Lett. **1**, 1692 (2010).

[18]A. Samanta, J. Phys. Chem. B **110**, 13704 (2006).

[19]A. Samanta, J. Phys. Chem. Lett. **1**, 1557 (2010).

[20]N. Ito and R. Richert, J. Phys. Chem. B **111**, 5016 (2007).

[21]H. Jin, G. A. Baker, S. Arzhantsev, J. Dong, and M. Maroncelli, J. Phys. Chem. B **111**, 7291 (2007).

[22]A. M. Funston, T. A. Fadeeva, J. F. Wishart, and E. W. Castner Jr., J. Phys. Chem. B **111**, 4963 (2007).

[23]P. J. Carlson, S. Bose, D. W. Armstrong, T. H. ans M. S. Gordon, and J. W. Petrich, J. Phys. Chem. B **116**, 503 (2012).

[24]S. K. Das and M. Sarkar, J. Lumin. **132**, 368 (2012).

[25]H. K. Kashyap and R. Biswas, J. Phys. Chem. B **112**, 12431 (2008).

[26]H. K. Kashyap and R. Biswas, J. Phys. Chem. B **114**, 254 (2010).

[27]S. Daschakraborty and R. Biswas, J. Chem. Phys. **137**, 114501 (2012).

[28]X. Song, J. Chem. Phys. **131**, 044503 (2009).

[29]B. L. Bhargava and S. Balasubramanian, J. Chem. Phys. **123**, 144505 (2005).

[30]M. N. Kobrak, J. Chem. Phys. **125**, 064502 (2006).

[31]Y. Shim, M. Y. Choi, and H. J. Kim, J. Chem. Phys. **122**, 044510 (2005).

[32]Y. Shim, J. Duan, M. Y. Choi, and H. J. Kim, J. Chem. Phys. **119**, 6411 (2003).

[33]D. Jeong, Y. Shim, M. Y. Choi, and H. J. Kim, J. Phys. Chem. B **111**, 4920 (2007).

[34]M. N. Kobrak and V. Znamenskiy, Chem. Phys. Lett. **395**, 127 (2004).

[35]Y. Shim and H. J. Kim, J. Phys. Chem. B **112**, 11028 (2008).

[36]M. N. Kobrak, J. Chem. Phys. **127**, 184507 (2007).

[37]Z. Hu and C. J. Margulis, J. Phys. Chem. B **110**, 11025 (2006).

[38]D. Roy and M. J. Maroncelli, J. Phys. Chem. B **116**, 5951 (2012).

[39]V. Znamenskiy and M. N. Kobrak, J. Phys. Chem. B **108**, 1072 (2004).

[40]Z. L. Terranova and S. A. Corcelli, J. Phys. Chem. B **117**, 15659 (2013).

[41]L. Martínez, R. Andrade, G. Birgin, and J. M. Martínez, J. Comput. Chem. **30**, 2157 (2009).

[42]C. Schröder and O. Steinhauser, J. Chem. Phys. **133**, 154511 (2010).

[43]M. Schmollngruber, C. Schröder, and O. Steinhauser, J. Chem. Phys. **138**, 204504 (2013).

[44]A. D. MacKerell Jr., B. Brooks, C. L. Brooks, L. Nilson, B. Roux, Y. Won, and M. Karplus, *The Encyclopedia of Computational Chemistry*, edited by P. V. R. Schleyer, Vol. 1 (Wiley, New York, 1998) p. 271.

[45]B. R. Brooks, R. E. Bruccoleri, B. D. Olafson, D. J. States, and S. Swaminathan, J. Comput. Chem. **4**, 187 (1983).

[46]J.-P. Ryckaert, G. Ciccotti, and H. J. C. Berendsen, J. Comput. Phys. **23**, 327 (1977).

[47]T. Darden, D. York, and L. Pedersen, J. Chem. Phys. **98**, 10089 (1993).

[48]U. Essmann, L. Perera, M. L. Berkowitz, T. Darden, H. Lee, and L. G. Pedersen, J. Chem. Phys. **102**, 8577 (1995).

[49]C. Schröder, T. Sonnleitner, R. Buchner, and O. Steinhauser, Phys. Chem. Chem. Phys. **13**, 12240 (2011).

[50]C. Schröder, Phys. Chem. Chem. Phys. **14**, 3089 (2012).

[51]Y. Shim, M. Y. Choi, and H. J. Kim, J. Chem. Phys. **122**, 044511 (2005).

[52]S. A. Egorov, J. Chem. Phys. **121**, 6948 (2004).

[53]S. Arzhantsev, N. Ito, M. Heitz, and M. Maroncelli, Chem. Phys. Lett. **381**, 278 (2003).

7 Final discussion

In principle there are two different ways to conduct molecular dynamics simulation, on the one hand simulation in equilibrium and on the other hand simulation in non-equilibrium. Depending on the problem one or the other simulation method may be more suitable.

Nevertheless, molecular dynamics simulation of ionic liquids (IL) requires particular attention on the correct handling of the used methods. The Lennard- Jones potential is responsible for the modeling of shape forces, which in their turn are needed to describe the anisotropy of the ions, especially the bulky cations. To be able to switch from local shape anisotropy to bulk isotropy, sufficiently large samples are needed. In addition, Coulomb forces are needed to deal with interacting intermolecular charge distributions. Because the infinite range of the Coulomb potential by r^{-1} is not compatible with finite computer simulation, another method to describe electrostatic forces has to be used, in our case the Ewald method. Nevertheless, the Ewald method also requires a certain system size to work properly. Furthermore, we should not forget to address viscosity. Due to the fact that ILs can be fluid as oil or sticky as lubricants, the dynamics is slowed down in comparison to simulations of water and we have to extend the simulation length for proper sampling.

Since we still have to face the finiteness of computational resources, we have to think about correct and therefore large enough system sizes, i.e. the number of molecules within a simulation box, to avoid artefacts in analysis. Furthermore, adequate simulation length has to be performed to gain consistent values from data analysis, such as structure, collective and single particle properties as well as dielectric spectra.

In my **first publication** [11] I address the effects of finiteness in system size and simulation length of the ionic liquid $C_2mim^+TfO^-$ in a systematic

way. Therefore, based on an all atom force field, extensive simulations of 70ns length were carried out for system sizes containing 8-2000 ion pairs. The examination of different properties such as energy, structure, collective and single particle properties as well as dielectric spectra, revealed that they differ in their dependence on system size and time.

While energies - Lennard-Jones, Coulomb and potential energy - are rather insensitive, 50 ion pairs are sufficient for the description of structure in short range order, but oscillations are going further on. For the correct handling of dynamics, however, at least 500 ion pairs are needed. While plotting values of various dynamical properties versus the inverse box length, a linear regime for larger systems arises. There are indications that the onset of this region is influenced by viscosity. An explanation for this regime can be found in hydrodynamics, at least for the translational diffusion coefficient. Thereby, we express the diffusion coefficient by using hydrodynamic terms and the Ewald potential instead of the bare Coulomb potential. The outcome of this is an expression for the self-diffusion coefficient, which includes the inverse box length as well as viscosity. Since the calculation of viscosity in IL still poses problems, we have now discovered a new possibility to determine the viscosity, provided the calculated translational diffusion coefficients of two different system sizes, which are part of the linear regime, are accurate. To conclude the discussion of finiteness in size and time, there is a clear order. It is important to simulate a system, which is part of the linear regime, because size dependence of a too small system cannot be compensated by a longer simulation. To calculate consistent dynamical properties, 20-30ns of trajectory data are needed.

The results on the effects of finiteness from this methodic work were used in all subsequent publications, which use molecular dynamics simulation. From that point on, another methodic step forward was made by introducing polarizability. In this manner the solvent can adjust the molecular charge distribution to changes in the local environment. One could say that polarization forces act as an inner solvent, which accelerate dynamics.

In the **second publication** [12] the finiteness in range of the heteronuclear *intermolecular* nuclear Overhauser effect (NOE) of $C_4mim^+BF_4^-$ is studied by means of a simple model theory. The given insights are signif-

icant for experimenters, because the NOE is normally used to study local structures in liquids and solutions. The NOE reveals cross-relaxation of two interacting nuclear spins, I and S, due to magnetization transfer of their coupled magnetic dipole moments. In case of the *intramolecular* NOE, where the spins reside on the very same molecule, the fluctuations of the dipole-dipole interaction decay with the sixth power of distance r between spins and result in an r^{-6} expression for the cross-relaxation rate σ_{IS}. Thus, only spin pairs with a distance of less than 4-5Å contribute to the NOE.

For the *intermolecular* NOE, however, the dipole-dipole relaxation is a lot more complex, because one has to include translational diffusion of the particles. Combined with molecular reorientation these motions modulate the fluctuations of the dipole-dipole interaction, which in turn are picked up by σ_{IS}. This cross-relaxation rate is a linear combination of two different frequencies of the spectral density function $J(\omega)$, namely the sum frequency $(\omega_I + \omega_S)$ and the difference frequency $(\omega_I - \omega_S)$. Since only σ_{IS} is experimentally accessible, the information on intermolecular structure and dynamics is given by $J(\omega)$, whose description is model dependent.

To account for translational motion in the spectral density function $J(\omega)$ in case of the *intermolecular* NOE, the vector $\vec{R}$ is needed, connecting the centres of mass of the ions. This vector is determined by the cation-anion distribution, described by the radial pair distribution function $g(R)$. To include rotational motions of the spins, which are located away from the centres of mass, the vectors $\vec{\delta}_I$ and $\vec{\delta}_S$ are required. Furthermore, the translational diffusion coefficient D_T, which is a sum of the self-diffusion coefficients, and the rotational diffusion coefficients $D_{R,I}$ and $D_{R,S}$ are necessary as parameters for our model.

To obtain an analytic expression for $J(\omega)$ in reciprocal space, $g(R)$ is approximated by a step function and the time evolution of the magnetic dipole-dipole interaction is given by solving the differential equations for both types of diffusion, translational and rotational. The resulting spectral density function $J(\omega)$ consists of three main terms: A term including spherical Bessel functions of rank l to capture the range in space, the rotranslational coupling function to describe pair dynamics and last a term, which involves a combination of the measureable rotational and transla-

tional diffusion coefficients, where solely translational diffusion is dependent on the wave vector k. All three terms are connected by summing up over l. In case of purely translational motion the off-centre vectors $\vec{\delta}_I$ and $\vec{\delta}_I$ reside in the centres of mass of the ions and only $l = 0$ contributes to the NOE, otherwise terms were added up to $l = 6$ to 10 to achieve convergence for our model.

Based on the formula for $J(\omega)$ the heteronuclear ^{1}H-^{19}F NOE of the ionic liquid $C_4mim^+BF_4^-$ was investigated by means of three models. Model A refers to the case, where $\vec{\delta}_I$ of the cation and $\vec{\delta}_S$ of the anion accord to the averaged distance of the off-centre located spins from their respective centre of mass. To assess the dependence of the NOE on spin eccentricity model B sets $\vec{\delta}_I$ to the value of maximum eccentricity. Model C considers the limiting case of purely translational motion, where $\vec{\delta}_I = \vec{\delta}_S = 0$.

Due to the fact, that there is a lot of literature on the NOE in the 'extreme-narrowing' limit, where $J(0) \approx J(\omega_I - \omega_S) \approx J(\omega_I + \omega_S)$, analysis is started there. The plot of $J(0)$, normalised by the respective asymptotic value, versus the distance R reveals an intermolecular NOE of long-range nature for all three models. A fit of the form R^{-n} results in slightly increasing values for n from 1.1 to 1.27, which goes along with increasing spin eccentricity. Thus, $J(\omega)$ is mainly dominated by translational dynamics.

As a next step, the complete frequency spectrum of $J(\omega)$ for various distances R is discussed. A main feature of the different graphs is that they coincide at high frequencies, but notably split up at low frequencies. We observe, that for a 400MHz spectrometer the sum and difference frequency are not located in the 'extreme-narrowing' limit. This is due to the fact that in high viscous solvents, as it is the case in ionic liquids, translational motion is greatly retarded and $J(\omega)$ is shifted to lower frequencies.

The values of $J(\omega)$ at selected values of the spatial range were extracted for a set of frequencies. For each frequency these values were fitted to R^{-n} and a plot of the exponents n versus the set of frequencies showed that low frequencies are of long-range nature, whereas high frequencies are of short-range nature. A reason for this behaviour can be pinpointed in the ro-translational coupling function, where ω and k, representatives for the frequency and reciprocal space respectively, counteract with each other.

This has further implications on the cross relaxation rate σ_{IS}. It is a linear combination of the long-range difference frequency $(\omega_I - \omega_S)$ and the short-range sum frequency $(\omega_I + \omega_S)$, resulting in a complex mixture of long-range and short-range effects.

So far, the investigation of the heteronuclear *intermolecular* NOE by means of a simple model theory revealed that the NOE is of long-range nature. Furthermore, a frequency dependence in the finiteness of range could be detected. In addition, it has been shown that the 'extreme-narrowing' limit can not be applied for ionic liquids or liquids of higher viscosity in general. To gain a better insight it this matter, a more thorough investigation is needed.

In the **third publication** [13] the heteronuclear *intermolecular* NOE in $C_2mim^+BF_4^-$ is analysed by molecular dynamics simulation and model theories. All model theories are compared to simulation results to assess their quality. In contrast to the previous publication [12] the cation C_4mim^+ was exchanged by its homologue C_2mim^+ to obtain the less viscous ionic liquid $C_2mim^+BF_4^-$. This has the advantage that phase space sampling during simulation is less time demanding.

For the evaluation of the spectral density function $J(\omega)$ of purely translational motion as well as ro-translational coupling of the spins, 30ns of trajectory data of 1000 ion pairs were used. For each of the 10^6 cation-anion pairs $J(\omega)$ was calculated via the dipole-dipole tensor. The spectral density function of each pair was labeled with the initial distance of the spins so that the distance resolved NOE could be deduced from it. Due to finite simulation time the spectral density function could only be calculated for a frequency window, which includes the frequency triple $((\omega_I - \omega_S)$, (ω_I) and $(\omega_I + \omega_S))$ of an 800MHz Proton spectrometer. Unfortunately it does not cover the difference frequency $(\omega_I - \omega_S)$ of a 400MHz Proton spectrometer. Finite simulation length is still the barrier for the calculation of the homonuclear NOE, since it requires extremely long simulation lengths for the spectral density function at zero frequency. Simulations of that duration are only feasible with a coarse-grained force field instead of an all-atom force field.

For model theories, the whole frequency range can be covered. Thereby, two entities need to be described, the structure of the interacting nuclei as well as pair dynamics. In the previous publication [12] structure was modeled by the step function whereas pair dynamics was described by a solution of the diffusion equation. For this work, the existing model theory was extended and new ones were developed. For a detailed description of the various theories please consult the publication itself. All model theories can be evaluated for purely translational motion as well as ro-translational coupling of the spins. Although ro-translational coupling is important in a quantitative sense, the qualitative features are essentially picked up by translational motion.

Comparison of the spectral density function $J(\omega)$ calculated from simulation data over two decades in frequency to the simple model theory clearly revealed deficiencies for the model theory. The sigmoidal shape of simulation data could not be reproduced by this theory, but the most striking feature of simulation data was the missing frequency dependence in spatial range.

In order to gain a better understanding of the frequency dependence in the existing model theory, some improvement had to be made. First, the step function was replaced by the radial pair distribution function, gained from simulation data, for a better description of the structure of the interacting spins. Comparison of the new model theory to simulation results showed that there are still shortcomings. Although, there is an improvement in shape in contrast to the step function, frequency dependence is still an issue.

In addition to the improved description of structure, a more complex pair dynamics is needed. Up to this point, dynamics was represented by a solution of the diffusion equation. Therefore, non-Gaussian diffusion models, such as jump and lattice diffusion, were investigated. The models were fitted to the spectral density function $J(\omega)$ of simulation data, which was only possible for high frequencies. Unfortunately, we arrived at totally unreasonable jump length and lattice points respectively.

Another possibility to improve pair dynamics is based on the fit of the simulated pair displacement of $C_2mim^+BF_4^-$. For this model theory, an

asymptotic approximation of the fit function was used and it showed the best consistency with the spectral density function of simulation data. Even more encouraging was the fact, that this model showed the least frequency dependence in spatial range of all model theories studied.

Even more sensitive than the spectral density function $J(\omega)$ itself is the cross relaxation rate σ_{IS}, which represents the curvature of $J(\omega)$ by balancing $6J(\omega_I + \omega_S)$ and $-J(\omega_I - \omega_S)$. The cross relaxation rate σ_{IS} itself depends on the combination of solvent viscosity and spectrometer frequency and can either be positive or negative. Dividing σ_{IS} by ρ_{II}, the longitudinal relaxation rate, we define the NOE-enhancement $f_I\{S\}$. The most striking feature of the NOE-enhancement is that it can get independent of the spatial range, as σ_{IS} and ρ_{II} have the same distance dependence.

After a thorough investigation of the *intermolecular* NOE in ionic liquids, some important findings have been discovered. The *intermolecular* NOE is of long-range nature, extending up to 30Å, and for this reason cannot be used to study local structures in liquids and solvents. Furthermore, the analysis of the distance dependence of $J(\omega)$ for all model theories revealed a frequency dependence, which is missing in simulation data. The frequency dependence gets less pronounced with increasing complexity of the model theory. Even more sensitive than the spectral density function is the cross-relaxation rate σ_{IS}, which balances contributions from high and low frequencies, and is actually measured by experiment.

In NMR the interaction of two nuclear spins, I and S, in a magnetic field is observed. An analogue can be found in dielectric spectroscopy, which analyses the response of a sample to an applied electronic field. Time dependent fluorescence spectroscopy can be used to study local solvation effects. Thereby, the solute changes its charge distribution upon electronic excitation and the subsequent relaxation of the solvent goes along with a time-dependent fluorescence shift of the emission frequency, which is used to quantify solvent dynamics.

On the one hand, molecular dynamics simulation can be used to interpret experimental Stokes shift data, since one can split the total solvation response function into contributions. On the other hand, the actual exper-

iment is very important to validate simulation results and potential model theories.

In the **fourth publication** [14] molecular dynamics simulation in non-equilibrium is used to evaluate the total solvation response function as well as various contributions of coumarin C153 dissolved in two different ionic liquids, $C_2mim^+TfO^-$ and $C_4mim^+BF_4^-$. Comparison to equilibrium simulation results and experiment is used to assess the quality of phase space sampling of non-equilibrium simulations.

In experiment several coumarin C153 molecules are dissolved in an ionic liquid and the solvation response function is made up by all of them. In contrast, only one coumarin C153 is placed inside the simulation box. To achieve proper phase space sampling, so that analysis will yield correct results, two methodic approaches can be pursued. In case of equilibrium simulation, proper sampling is achieved by generating a trajectory of appropriate length. Simulation in non-equilibrium does not require such long trajectory data, but adequate phase space sampling needs averaging over a great number of simulations, started from different configurations.

In this work, a new approach to configure start configurations for non-equilibrium simulations has been tested. Normally, start configurations are generated from an equilibrium trajectory only separated by a few time steps, where the configurations do not significantly differ from each other. In contrast, 150 'independent' start configurations were created by the program PACKMOL [15] and simulated for 1ns. This has the advantage of a better phase space sampling.

To rate the quality and number of non-equilibrium simulations, two entities are investigated. On the one hand, the values of the time series of the solvation energy $\Delta U(t)$, gained from an equilibrium trajectory simulated in the excited state $S1$, were transfered to a normalised histogram, which was compared to another normalised histogram made up by all 150 values of $\Delta U(\infty)$, the asymptotic limit of the calculated time series $\Delta U(t)$ of a non-equilibrium trajectory. The histograms were in good agreement and in addition, the histogram, belonging to non-equilibrium, had a similar shape to the emission frequency band of the experiment. On the other hand, the averaged solvation energies $\langle \Delta U(t) \rangle_{eq}$ of equilibrium simulation were com-

pared to $\overline{\Delta U(\infty)}$, were the overbar indicates averaging over non-equilibrium simulations. The values were in good agreement to each other. This leads to the conclusion that equilibrium and non-equilibrium simulations are consistent.

Comparison of the solvation response function of non-equilibrium to equilibrium simulation and experiment showed again good agreement for both ionic liquids. For the more viscous IL $C_4mim^+BF_4^-$ the non-equilibrium result is actually better than the equilibrium one, since we do not have to deal with insufficient sampling of phase space due to too short simulation length, where we are confined to a limited region in phase space.

The greatest advantage of non-equilibrium simulation lies in its analysis. The total solvation response function can be partitioned into various contributions without having to deal with cross-terms as it is the case for equilibrium simulation. This facilitates the interpretation of the contributions a lot.

While taking a closer look on the contributions of cations and anions, it is obvious the total solvation response function has its shape from the anions. Nevertheless, the cations are responsible for a high but constant background.

By splitting the total solvation response function into contributions of permanent and induced charges, the importance of polarizability is emphasised. The induced charges, i.e. Drude particles, counteract the permanent charges, thus acting as an inner solvent, which is needed to react appropriately on the sudden change of the charge distribution in the solute molecule C153.

Another advantage of conducting non-equilibrium simulations lies in its potential of being run parallel on a suitable computer architecture.

I would like to conclude this thesis with some final remarks. Based on different methodic approaches, equilibrium and non-equilibrium simulation, questions on the effects of finiteness and sampling in simulation of ionic liquids are (hopefully) sufficiently answered. Furthermore, interesting aspects of the spatial range in the *intermolecular* NOE have been elucidated by use of model theories as well as analysed molecular dynamics simulation.

Bibliography

[1] J. P. Hallett and T. Welton, *Chem. Rev.* **111**, 3508 (2011).

[2] M. Armand, F. Endres, D. R. MacFarlane, H. Ohno, and B. Scrosati, *Nature Materials* **8**, 621 (2009).

[3] Y. Shim, Y. Jung, and H. J. Kim, *J. Phys. Chem. C* **115**, 23574 (2011).

[4] N. V. Plechkova and K. R. Seddon, *Chem. Soc. Rev.* **37**, 123 (2008).

[5] H. Zhao, S. Xia, and P. Ma, **80**, 1089 (2005).

[6] M. J. Earle, J. M. S. S. Esperanca, M. A. Gilea, J. N. Canongia Lopes, L. P. N. Rebelo, J. W. Magee, K. R. Seddon, and J. A. Widegren, *Nature* **439**, 831 (2006).

[7] B. Jastorff, R. Störmann, J. Ranke, K. Mölter, F. Stock, B. Oberheitmann, W. Hoffmann, J. Hoffmann, M. Nüchter, B. Ondruschka, and J. Filser, *Green Chem.* **5**, 136 (2003).

[8] A. R. Leach, *Molecular Modelling: Principles and Applications*, Pearson Education, 2001.

[9] M. P. Allen and D. J. Tildesley, *Computer simulations of liquids*, Oxford Press, New York, 1989.

[10] G. Lamoureux and B. Roux, *J. Chem. Phys.* **119**, 3025 (2003).

[11] S. Gabl, C. Schröder, and O. Steinhauser, *J. Chem. Phys.* **137**, 094501 (2012).

[12] S. Gabl, O. Steinhauser, and H. Weingärtner, *Angew. Chem. Int. Ed.* **52**, 9242 (2013).

[13] S. Gabl, C. Schröder, H. Weingärtner, and O. Steinhauser, *J. Chem. Phys.* **140**, 184503 (2014).

[14] S. Gabl, C. Schröder, and O. Steinhauser, *intended for submission to J. Chem. Phys.* (2014).

[15] L. Martínez, R. Andrade, G. Birgin, and J. M. Martínez, *J. Comput. Chem.* **30**, 2157 (2009).

Curriculum Vitae

Sonja Gabl

Email: sonja@mdy.univie.ac.at

Education

since 04/2010	**Dr. rer. nat., Chemistry**, University of Vienna
03/2004 - 04/2010	**Mag. rer. nat., Chemistry**, University of Vienna

Research Experience

since 04/2010	**Department of Computational Biological Chemistry, University of Vienna** Thesis: *On the effects of finiteness and sampling in simulation of ionic liquids: Implications for molecular dynamics simulations and NMR theory* Advisor: Prof. O. Steinhauser
03/2004 - 04/2010	**Department of Computational Biological Chemistry, University of Vienna** Diploma Thesis: *Start Configurations for Simulation of Ionic Liquids: Generation and Assessment* Advisor: Prof. O. Steinhauser
10/2007 - 12/2007	**Department of Theoretical Chemistry, University of Warwick, GB** Erasmus semester with focus on research in theoretical chemistry Advisor: Prof. R. Deeth

Teaching Experience

10/2010 - 05/2014	Teaching Assistant 'Mathematics for Molecular Biologists'
03/2013 - 05/2014	Teaching Assistant 'Mathematics for Biological Chemists'
10/2010 - 06/2012	Teaching Assistant 'Theoretical Chemical Exercises'